Spectroscopic Studies of Optical Second-Harmonic Generation

from Si(001) Surfaces

by

YONG QIANG AN

A thesis submitted to the

Faculty of the Graduate School of the

University of Colorado in partial fulfillment

of the requirements for the degree of

Doctor of Philosophy

Department of Physics

2003

This thesis entitled:
Spectroscopic Studies of Optical Second-Harmonic Generation from Si(001) Surfaces
written by Yong Qiang An
has been approved for the Department of Physics

____

Dr. Steven T. Cundiff

____

Dr. Charles T. Rogers

Date ________________________

The final copy of this thesis has been examined by the signatories, and we find that both the content and the form meet acceptable presentation standards of scholarly work in the above mentioned discipline.

An, Yong Qiang (Ph. D., Physics)

Spectroscopic Studies of Optical Second-Harmonic Generation from Si(001) Surfaces

Thesis directed by Professor Steven T. Cundiff

I present a spectroscopic study of optical second-harmonic generation (SHG) from Si(001) surfaces and interfaces in the vicinity of the direct two-photon E_1 transition using tunable femtosecond lasers. The samples investigated are oxidized Si, hydrogen terminated Si, and Cr-SiO_2-Si structures. I first use a phenomenological theory and susceptibility tensors to predict the symmetry properties of several different SHG contributions and present methods for separating bulk and surface SHG contributions and uniquely determining susceptibility tensor elements. By measuring polarization selected rotational-anisotropy SHG (RA-SHG), I show that both bulk and surface SHG contributions display resonances and that interference between these contributions can shift the apparent resonance energy. The strength of bulk and surface SHG contributions varies with photon energy. Linear optics also plays a role in SHG spectroscopy. For certain photon energies, the peak locations of the RA-SHG signals from oxidized and hydrogen terminated Si(001) surfaces differ. This indicates phase shift between surface SHG fields. For appropriate polarizations, peaks of the RA-SHG signals from oxidized Si surfaces can be turned into valleys by varying the photon energy, and eightfold symmetric RA-SHG signals can be observed at certain photon energies. Comparison of RA-SHG signals from Cr-SiO_2-Si

structures and oxidized Si samples also shows a difference in the peak location at certain photon energies. Further experimental results show that an ultrathin Cr coating film on oxidized Si introduces additional sources of SHG, which modify the spectra and time-dependence of SHG. I also study the effect of thermal oxidation of Si(001) samples on SHG and show that SHG is sensitive to interface width. RA-SHG signals with eightfold symmetry are found for several different polarizations and the corresponding photon energies are sensitive to interface conditions. Thermal oxidation affects the time-dependence and spectroscopy of SHG. These results indicate that SHG spectroscopy is a powerful tool for characterizing Si surfaces or interfaces.

Dedication

To the memory of my grandfather.

Acknowledgments

There are many people who have made this thesis and this work possible.

I wish first to thank my advisor, Steven Cundiff, for his support and guidance during my graduate studies. His ability to instruct clear physics and to explain it concisely has set a standard to which I will always aspire. His willingness to promote me professionally through teaching me English and sending me to conferences has been most generous. He has always been available to talk to me. Through his interest and enthusiasm for my work, he has driven me to do my personal best in the lab. An advisor can do little more for a student.

I would like to thank my committee members: Charles Rogers, Daniel Dessau, Henry Kapteyn, and Kelvin Wagner, for many helpful comments and questions on my thesis.

I am grateful for the help of many incredibly talented scientists, postdocs, and students at JILA during my graduate studies. I thank Prof. Stephen Leone for help in my Comps III exam. I thank Prof. David Nesbitt for critical reading of my manuscripts. JILA is a wonderful place to do research because of the wide array of talented, knowledgeable, and helpful support staff. I am thankful for the electronics shop, the computing, the instrument shop, and the administration staff for their help. I thank David Alchenberger for help in preparing experiment samples, and Barbara Tennis and Marilee DeGeode for helpful English classes.

I would like to thank the whole Cundiff group for making the lab an enjoyable place to work and to live. These members are Justin Shacklette, Amy Spivey, Tara Fortier, Kelda Furbush, Virginia Lorenz, Zhigang Chen, Qudsia Quraishi, Tianhao

Zhang, David Jones, Camelia Borca, Rudolf Bratschitsch, Pete Roos, Martin Griebel, Soobong Choi, and Jessi Ames. I enjoyed and would remember our group skiing trips to Eldora and Keystone.

Finally, I would like to thank all my family members for their constant love and support. Especially, I thank my wife, Chuanxia, for all of her kind support, encouragement, and unconditional love, and my son, Rocky, for the love and joy he brings.

CONTENTS

Abstract, Acknowledgments, Contents, List of Tables, and List of Figures i-xv

Chapter

1 Introduction 1

1.1 Historical Overview of Second-Harmonic Generation (SHG) 1

1.2 This Work 4

1.3 Experimental Setup 8

2 Phenomenological Theory of SHG from Si Surfaces 14

2.1 Introduction 14

2.2 The Model 14

2.3 Rotational-Anisotropy SHG (RA-SHG) 18

2.3.1 Bulk and Surface Second-Harmonic (SH) Contributions 18

2.3.2 RA-SHG from Vicinal Si Faces 21

2.3.3 RA-SHG from the Si(001) Face 32

2.4 Separation of Bulk and Surface SH Contributions 35

2.5 Summary 38

3 Bulk and Surface Contributions to Resonant SHG 40

3.1 Introduction 40

3.2 Bulk and Surface SHG Contributions 42

3.3 Sample Preparation and Experimental Methods 43

3.4 Experimental Results 44

3.4.1 Spectroscopy of the Bulk Anisotropic Contribution 44

3.4.2 Spectroscopy of the Isotropic Contribution 47

3.5 Discussion 51

3.6 Summary 52

4 Phase Inversion in RA-SHG 54

4.1 Introduction 54

4.2 Experimental Conditions and Sample Preparation 55

4.3 Observed Phase Inversions 55

4.3.1 Phase Inversion due to Photon Energy Variation 55

4.3.2 Phase Inversion due to Surface Modification 57

4.4 Phase and Amplitude of Susceptibility Tensors 59

4.5 Discussion 63

4.6 Summary 66

5 SHG from Cr-SiO_2-Si(001) Structures 68

5.1 Introduction 68

5.2 Theoretical Background 71

5.3 Experimental Conditions and Sample Preparation 73

5.4 Experimental Results 73

5.4.1 Comparison of RA-SHG from Cr-SiO_2-Si and SiO_2-Si Surfaces 73

5.4.2 Spectroscopic Study of RA-SHG from Cr-SiO_2-Si 79

5.4.3 Comparison of TD-SHG from Cr-SiO_2-Si and SiO_2-Si Surfaces 81

5.5 Discussion and Further Experiments 83

5.5.1 Phase Inversion due to Additional SHG Sources 83

5.5.2 Further Experiments to Detect for SHG Sources 84

5.5.3 Insight into the Charge Trapping Process 88

5.6 Summary 91

6 SHG from Thermally Oxidized Si(001) Surfaces 93

6.1 Introduction 93

6.2 Experimental Conditions and Sample Preparation 96

6.3 Variation of SHG with Oxide Thickness 97

6.3.1 Isotropic and Anisotropic SHG Contributions 97

6.3.2 Phase Inversion Photon Energy 101

6.3.3 Time-dependent SHG 104

6.3.4 Effect of Thermal Oxidation on SHG Spectroscopy 105

6.4 Discussion 108

6.5 Summary 109

7 Conclusions 111

Bibliography 113

Appendix: SHG from Vicinal Si(001) Surfaces 121

LIST OF TABLES

Table

2.1 Angular functions $\Phi_m(\alpha)$ 25

2.2 $b^{BQ}_{00,(g,h)}$ and $b^{BQ}_{m,(g,h)}$ as functions of Fresnel factors 26

2.3 $b^{d}_{00,(g,h)}$ and $b^{d}_{m,(g,h)}$ as functions of Fresnel factors 28

2.4 $s^{SD}_{m,(g,h)}$ as combinations of Fresnel factors and tensor elements 30

LIST OF FIGURES

Figure

1.1 Experimental setup for surface SHG 9

2.1 Geometry and unit vectors for the propagating fundamental and SH fields 15

2.2 Diagram of the beam frame and the vicinal surface with respect to the cubic crystal axes 22

2.3 Definition of the linear polarization configuration with the incident fundamental beam (a) and the reflected SH beam (b) 33

3.1 Spectra of the anisotropic SHG contribution $a_{4,(p,s)}$, the linear optics coefficient $L_{(p,s)}$, and the magnitude ($|\zeta|$) of the anisotropic element ζ 46

3.2 RA-SHG intensities from modified Si(001) surfaces (NO-Si, TO-Si and H-Si) at a two-photon energy of 3.26 eV for different polarization configurations: (*p, p*), top panel and (*p, s*), bottom panel 48

3.3 Spectra of the isotropic amplitudes $a_{0,r}$ for NO-Si and TO-Si (top panel) and the interfering and non-interfering isotropic amplitudes $a_{0,r}$ and $a_{0,i}$ for H-Si (bottom panel) 50

4.1 RA-SHG signals from both TO-Si and NO-Si samples for the polarization (*s, p*) at several two-photon energies 56

4.2 RA-SHG intensities from modified Si(001) surfaces (NO-Si, TO-Si, and H-Si) at a two-photon energy of 3.26 eV for different polarizations: (*s, p*), top panel, and (*q, s*), bottom panel 58

4.3 Spectra of the amplitudes and relative phases of the tensor elements ∂_{31} (upper panel) and ∂_{15} (lower panel) for all three samples: TO-Si, NO-Si and H-Si 62

5.1 RA-SHG signals from Cr-NO-Si and Cr-TO-Si samples for the (*p, p*), (*s, p*), and (*q, s*) polarizations at a two-photon energy of 3.40 eV 75

5.2 RA-SHG signals from both NO-Si and TO-Si samples for the (*p, p*), (*s, p*), and (*q, s*) polarizations at a two-photon energy of 3.40 eV 76

5.3 Comparison of the (*p, s*) polarized RA-SHG signals from TO-Si and Cr-TO-Si samples at a two-photon energy of 3.40 eV 78

5.4 (*p, p*) polarized RA-SHG intensities from the Cr-TO-Si sample at two-photon energies. Note that the RA-SHG with eightfold symmetry appears at the two-photon energy of 3.35 eV 80

5.5 Comparison of the TD-SHG signals for the (*p, p*) polarization at a two-photon energy of 3.40 eV for different samples: NO-Si and TO-Si (upper panel); Cr-NO-Si and Cr-TO-Si (lower panel) 82

5.6 Isotropic SHG signals variation with two-photon energy from the surfaces of bulk Cr, thin Cr coated silica, and silica covered Cr 86

6.1 Ratio of the isotropic to anisotropic SHG components for the (*p, p*) polarization (upper panel) and anisotropic SHG components for the (*p, s*)

polarization (lower panel) as a function of oxide thickness at several two-photon energies: 3.44 eV, 3.40 eV, and 3.26 eV 100

6.2 Upper panel: oxide thickness dependence of the two-photon energy at which the RA-SHG signal shows eightfold symmetry for (*p, p*), (*q, s*), and (*s, p*) polarizations. Lower panel: RA-SHG signals from a thermally oxidized Si(001) sample with 57.9 nm thick oxide for the (*s, p*) polarization, showing either eightfold or fourfold symmetry 102

6.3 Time-dependent SHG signal for the (*p, p*) polarization at a two-photon energy of 3.26 eV for several thermally oxidized Si(001) surfaces with different thicknesses of the oxide layer 104

6.4 SH spectra from a thermally oxidized Si(001) sample with 57.9 nm thick oxide at a fixed azimuthal angle of 22.5^o for different polarization configurations: (*p, p*), (*s, p*), and (*q, s*) 107

A.1 (*p, p*) polarized RA-SHG signals at a two-photon energy of 3.22 eV from natively oxidized vicinal Si(001) surfaces (NO-Si V) (upper panel) and thermally oxidized vicinal Si(001) surfaces (TO-Si V) (lower panel) with different vicinal angles of 0°, 1°, 2°, 3°, 4°, and 5° 123

A.2 (*p, p*) polarized RA-SHG signals from a natively oxidized Si sample with vicinal angle of 5° (NO-Si V5) (upper panel) and a thermally oxidized Si sample with vicinal angle of 5° (TO-Si V5) (lower panel) at two-photon energies 4.34 eV, 4.41 eV, and 4.48 eV 124

A.3 RA-SHG signals from a natively oxidized Si sample with vicinal angle of 5° (NO-Si V5) at several two-photon energies of 3.10 eV 3.26 eV, 3.40 eV,

and 3. 49 eV for different polarizations: (*p, p*), (*s, p*), (*p, s*), and (*s, s*) 125

A.4 RA-SHG signal from a thermally oxidized Si sample with vicinal angle of 5° (TO-Si V5) at several two-photon energies of 3.10 eV 3.26 eV, 3.40 eV, and 3. 49 eV for different polarizations: (*p, p*), (*s, p*), (*p, s*), and (*s, s*) 126

A.5 RA-SHG signal from a hydrogen terminated Si sample with vicinal angle of 5° (H-Si V5) at several two-photon energies of 3.10 eV 3.26 eV, 3.40 eV, and 3. 49 eV for different polarizations: (*p, p*), (*s, p*), (*p, s*), and (*s, s*) 127

Chapter 1

Introduction

1.1 Historical overview

A new branch of physics, nonlinear optics, was born in 1961 when Franken *et al*. [1] first demonstrated second-harmonic generation in a quartz crystal. Numerous nonlinear optical phenomena have been discovered since then. As laser technology progressed, nonlinear optics has become increasingly more mature and several comprehensive text books have been written on this subject [2-5]. Within the vast area of nonlinear optics, second-harmonic generation (SHG), or the frequency doubling of light, plays an essential role.

In 1962, theoretical investigations dealing with the behavior of light waves by solving the Maxwell's equations in a nonlinear dielectric and at the boundary of nonlinear media were perform by Armstrong *et al.* [6] and Bloembergen *et al*. [7], respectively. The classical laws of optical reflection and refraction were generalized to treat the nonlinear optical response. The predicted laws of nonlinear reflection were verified by Ducuing *et al*. [8] and both the real and imaginary parts of the complex nonlinear susceptibility were measured by Chang *et al*. [9].

SHG in a medium with a center of inversion symmetry was first observed by Terhune *et al*. in calcite [10]. They introduced a nonlinear term of quadrupolar origin in the form of a second-harmonic (SH) polarization proportional to the product of the fundamental field and its gradient. The most careful observation of the quadrupole effect in a phase matched propagation geometry in calcite was carried out by

Bjorkholm and Siegman [11]. In cubic and isotropic media with inversion symmetry, the quadrupole term does not give rise to transmitted harmonic radiation as the polarization source of the quadrupolar origin has only a longitudinal component.

Initial experiments on cubic centrosymmetric materials, particularly Si and Ge, were carried out by Bloembergen *et al.* [12]. The resulting SH signal was believed to originate solely from the nonlinear quadrupolar source term and independent of surface conditions. Moreover, the SH signal was found to be independent of the orientation of the surface cut with respect to the crystallographic axes. Wang first proposed that SHG from isotropic media originated from a surface dipole layer by inferring from studies on liquid-air interfaces [13]. The exist of a dipole layer at the interface responsible for the observed signal implies the surface sensitivity of this technique. The surface sensitivity of SHG was demonstrated by Brown and Matsuoka in 1969 [14] and by Chen *et al.* in 1973 [15] through observation of dramatic change in SHG upon surface modification.

The development of nonlinear optics during the decade of the sixties was followed by a decade with relatively little activity. Since 1980, the subject has experienced a period of continuous growth. As described by Bloembergen in a historical overview paper [16], for this topic one may designate the decade of the sixties as the period of "classical antiquity", the seventies as the Middle Ages, with the renaissance starting in 1980. Downer described that today's nonlinear optics is probably in "a new low" and a new era is about to begin [17].

The potential of SHG as a surface-specific tool was not fully exploited until the decade of the eighties. Shen [18, 19] and Richmond *et al.* [20] have reviewed the

progress on SHG at interfaces of media with inversion symmetry made during the eighties. SHG as a surface probe has received much attention because of it simplicity, surface specificity, and versatility. In 1983, the potential of SHG was demonstrated for its surface-specific spectroscopy [21], and the ability to measure molecular adsorbate orientation [22]. The discovery of the dependence of SHG on crystal orientation by Guidotti *et al.* [23], however, showed that SHG has a bulk contribution. The anisotropic SH signal from both Si and Ge was observed by measuring the SH signal reflected from these surfaces while azimuthally rotating the substrates. The SH anisotropy was attributed to the bulk electric-dipole mechanism being permitted through inversion-symmetry breaking by high-density photo-induced carriers. The rotational-anisotropy SHG (RA-SHG) from Si surfaces was also demonstrated by Tom *et al.* [24], but the anisotropy of SHG was claimed to originate from the bulk quadrupole effect. The explanation of Litwin *et al*. [25] agreed with the bulk quadrupole model and it was generally accepted later.

If one intends to use the SHG technique as a probe for surface-specific properties, one must be able to distinguish surface and bulk contributions. Guyot-Sionnest *et al*. [26] discussed various conditions under which the surface contribution is expected to be large relative to the bulk contribution. Sipe *et al.* [27] developed a phenomenological theory of SHG for cubic centrosymmetric crystals and discussed the possibility of bulk and surface discrimination. It has been shown that separation of bulk and surface SH contributions is a problem of fundamental difficulty in the use of SHG as a strictly surface probe [28]. However, in most cases strict separation is not needed because the surface SHG usually dominates over the bulk SHG.

In recent years, SHG has matured into a versatile and powerful technique for probing the electronic and structural properties of surface or interfaces, as described in several excellent review papers [29-31]. With the advent of the mode-locked Ti:sapphire laser [32] and the tunable short pulse optical parametric amplifier/oscillator systems, spectroscopic SHG studies could be carried out over a wide wavelength range on important semiconductor interfaces. The demonstration of resonant enhancement of SHG at the Si-SiO_2 interface provided insight into electronic structures at the interface [33]. Microscopic theories have been developed to predict and explain the SH spectra [34, 35]. Among the later significant developments in Si surfaces, the studies demonstrating the dc field enhancement of SHG [36, 37] and the time-dependence of SHG [38] are related to this work.

1.2 This work

SHG has been recognized and used for more than two decades in basic research on the physical and chemical properties of surfaces or interfaces. Using the SHG technique as a surface-specific probe is based on the principle that SHG is electric-dipole forbidden in the bulk of media with inversion symmetry, such as Si and Ge, but allowed at the surface where the inversion symmetry is broken. Existence of the bulk SHG in the total SH signal is against the basic principle of surface selectivity of SHG, and it is generally believed to be a fundamental problem for using the surface SHG technique. Most previous surface SHG studies neglected or inadequately addressed the bulk SH contribution. However, we take advantage of the natural co-existence of bulk and surface SH contributions and use the interference

between them to monitor the phase of the surface SH field. We also investigate the relative size of bulk and surface SH contributions by varying with photon energy.

We use the SHG technique to study the buried SiO_2-Si interface. Since the SHG technique is an optical probe, it can access buried interfaces if the top medium is transparent. The significant advantages of the SHG probe include capabilities of non-contact, non-invasive, and in situ sampling. Spatial and/or temporal resolution of the laser beam is also potentially attractive. The SiO_2-Si interface is of enormous technological importance to integrated circuit manufacturers. It occurs in the channel region of metal-oxide-semiconductor field-effect-transistors, which are the basic building blocks of modern integrated circuits.

Crystalline Si is one of the most intensively studied media, thus the medium properties can be easily related to the measured SH signal. Physical properties (density: 2.33 g/cm^3, melting point: 1415 ^{o}C, band gap: 1.12 eV, electron mobility: 1350 cm /Vs, hole mobility: 480 cm /Vs, resistivity: 2.5 x 10^5 Ω-cm, etc.) [39] and lattice structures and symmetry (structure: diamond structure with a=5.42 Å, space group: $Fd\overline{3}m$, crystal class: $\overline{m}3m$ (international notation) or O_h^7 (Schonfliess notation), symmetry formula: $3L_4 4L_3 6L_2 9PC$) [40] are well known for single crystal Si. Our Si samples were provided by Virginia Semiconductor, Inc.

We study the SHG mainly from Si surfaces with (001) orientation. The SHG response from this surface can be characterized by a relatively small number of susceptibility tensor elements, which is an advantage in separating the bulk and surface SH contributions. Practically speaking, microelectronic circuits are built exclusively on wafers with the (001) orientation. The structural quality of SiO_2-

Si(001) interfaces is superior over SiO_2-Si(111) interfaces. The SH response of the Si(001) interface is usually much weaker than that from the more intensity studied Si(111) surface. SHG studies of the Si(001) surface have been comparatively few in number, incomplete, or controversial in significant ways. It is timely and important to perform a comprehensive spectroscopic SHG study on the technologically important Si(001) surface.

A good SiO_2-Si interface should be nearly atomically smooth, have as few electrically active defects as possible, and have a minimal concentration of carrier traps that can be charged, either permanently or temporarily. Charge trapping can modify the electronic state at the interface, which can be monitored by time-dependent SHG (TD-SHG). For oxidized Si surfaces, especially those with thin oxide layers, phenomenological susceptibility tensors are not constant values, because laser interaction with the interfacial medium may cause quasi-static time-dependent effects. For example, charge transfer by photo-injection across the SiO_2-Si interface may build up an effective dc electric field, which causes time-dependence of SHG.

This thesis is mainly a spectroscopic study of SHG from principal (flatcut) Si(001) surfaces. Some results of SHG on vicinal (miscut by a small angle from principal face) Si(001) surfaces are presented in an appendix. In addition to the SH intensity, we observe the variation of the phase of SH field with photon energy. By comparing SH signals from different surfaces, we investigate the relationship between the observed SH signal and the interfacial properties. Some of these results are also presented elsewhere in publications [41, 42].

We first discuss, in the next section, the general experimental setup used during the SHG experiments. In Chapter 2, we use a phenomenological theory of SHG to predict the symmetry property of SHG and extend to calculation of bulk and surface electric-field-induced SHG (EFISH) effects from either principal or vicinal Si(001) surfaces. In addition, we discuss the possibility of separating bulk and surface SH contributions and present methods for uniquely determining susceptibility tensor elements. In Chapter 3, we study bulk and surface contributions to resonant SHG from Si(001) surfaces and show that interference between bulk and surface contributions can modify the apparent spectrum obtained for a fixed azimuthal angle. In Chapter 4, we present the observation of the phase inversion in rotational-anisotropy SHG at Si(001) interfaces, which can be induced by either varying the photon energy or by surface modification. In Chapter 5, we compare RA-SHG spectroscopy and time-dependent SHG results from Cr-SiO_2-Si(001) structures with an ultrathin Cr coating film and SiO_2-Si(001) surfaces with coating. The difference in the SHG signal between Cr coated and uncoated samples was attributed to additional SH sources caused by the ultrathin Cr film. In Chapter 6, we study the effect of thermal oxidation of Si(001) samples on SHG. We show that RA-SHG, TD-SHG, and SHG spectroscopy depend strongly on the interface width caused by thermal oxidation. For the same sample, the resonant behaviors of SHG are polarization dependent. In Chapter 7, we summarize the results of SHG on Si(001) surfaces and their implications, and present our view of the weakness and strongpoint of the surface SHG technique. In the appendix, we present the results of SHG on vicinal Si(001) surfaces.

1.3 Experimental setup

SHG from Si surfaces is a very weak effect because the main SHG contribution comes from only a few monolayers of atoms with broken inversion symmetry. This requires the use of short pulsed lasers to generate high peak powers and photon-counting to detect the weak signals. SHG signals are collected as a function of the azimuthal angle of the sample and as a function of time with the same basic apparatus.

The apparatus for measuring SHG is shown in Fig. 1.1. This apparatus can measure both rotational-anisotropy SHG (RA-SHG) and time-dependent SHG (TD-SHG). Both of these are discussed in more detail in the following chapters. RA-SHG provides information about the symmetry of the interface and the interference of different SHG contributions. TD-SHG is sensitive to the carrier dynamics at the interface, which affects the SHG signal.

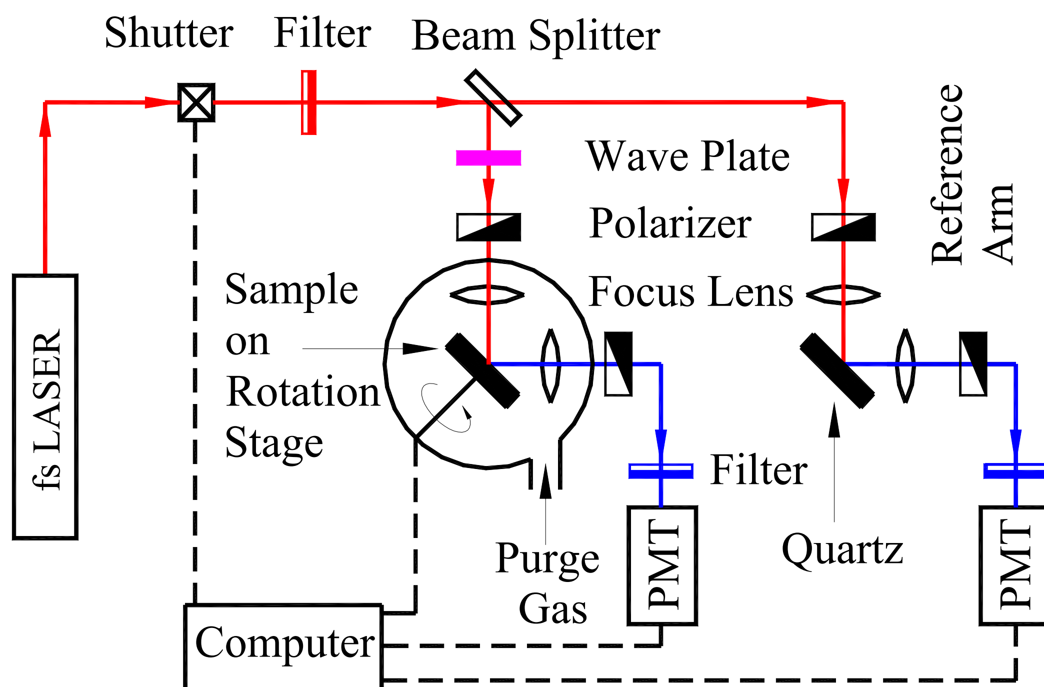

Fig. 1.1. Experimental setup for surface SHG. Components are described in text.

The laser pulses are generated by a Kerr-lens-modelocked Ti:sapphire laser (Coherent Mira 900). The Ti:sapphire laser is pumped by either an argon-ion laser (Coherent Innova 300) or a diode-pumped solid-state laser (Coherent Verdi V10). The pulse width is typically about 150 fs, but increases at edges of the spectral range to about 200 fs (more strongly at the blue edge). The pulse repetition rate is about 76 MHz. Output of the Ti:sapphire laser can be tuned from 700 to 900 nm (photon energies of 1.38-1.77 eV). An optical parametric oscillator (OPO) (Coherent APE OPO Basic) synchronously pumped by the Ti:sapphire laser is used to realize additional spectroscopic tuning. It is based on a collinear, noncritical phasematched process in KTP crystals and made for a frequency transformation from the Ti:sapphire range to 1050~1600 nm. To further extend the spectroscopic tuning range, a BBO crystal is used to double the frequency of the output pulses from the OPO to obtain pulses around 550 nm. A prism pair is used to compensate for the group-velocity-dispersion and simultaneously to eliminate unwanted spectral bands. If such a prism pair is not used, an important consideration in experimental design is to minimize the amount of material that the pulses traverse. Material group-velocity-dispersion stretches the pulses, thereby reducing the peak intensity and hence the nonlinear signal.

The laser pulses pass through a filter to remove any residual scattered background pump light. They are then split between signal and reference arms by a dielectric beam splitter that is designed to be 50% reflective at 750 nm. The beam in the signal arm passes through a half-wave plate and a polarizer before being focused on the sample. The focusing lens is a gradient index lens with a 10 mm focal length.

This lens is chosen to give the tightest possible focus while passing through the smallest possible amount of glass. It can produce close to a diffraction-limited spot of 4 μm. The beam is incident on the sample at an angle of 45° from the surface normal. The reflected beam, which now includes SH light, is collimated by a UV-fused-silica lens. The reflected beam passes through a polarizer and then a filter that transmits the SH light while absorbing the fundamental light. The SH signal is detected using a photomultiplier tube (PMT) that has a photocathode with a large work function so that it is insensitive to the fundamental light (nevertheless multi-photon processes at the photocathode can result in a signal from the fundamental if it is too strong). The optical path of the reference arm, which is used for normalization, is essentially the same as the signal arm, with the exception that the half-wave plate is omitted. Neutral density filters are included in the signal arm before the sample to control the incident power onto the silicon samples. A neutral density filter is included in the reference arm after the sample to avoid overloading the detection electronics; there is no risk of damaging the quartz sample in the reference arm with the available power levels. SHG from the optical elements is unmeasurable, even if they had an SHG efficiency as high as silicon, the fact that they are only exposed to an unfocused beam means that their response would be several orders of magnitude less than that from the sample.

The average power on the sample is between 40 and 80 mW (varies with wavelength). At this power level, heating of the Si samples is negligible. Because of the tight focus and short pulses, these modest average power levels correspond to a peak intensity of 3 GW/cm^2.

The signals from both PMTs are recorded by a computer interfaced with photon-counting electronics. The computer controls a rotation stage on which the sample in the signal arm is mounted. The rotation axis is in the surface normal direction. This allows data to be collected as a function of the sample azimuthal angle for the RA-SHG measurements. The computer also controls a shutter in the incident laser beam. This is used for the TD-SHG measurements. It is also used to allow the sample to discharge in the dark before and between RA-SHG scans.

The polarization optical elements are used to select orientation of the excitation beams and to analyze the SHG beams. The polarizers in the incident beams are either borosilicate glass with aligned silver particles or Glan Thompson prisms. The half-wave plate is zero order to obtain the greatest possible bandwidth and is made from a birefringent polymer stack on BK7 glass to obtain as thin an element as possible. The polarizers in the reflected beams are Glan Taylor prisms.

The test sample is enclosed in a chamber that can be purged. This is required because different gases in the ambient may have different influences on the oxide charging phenomena and on the properties at the medium-ambient interface, which in turn affect the SHG signal. The laser beams enter and exit the purge chamber via 1.5 mm thick UV-fused silica windows. The stream of the purging gas is directed towards the sample in order to improve the purity.

A reference arm is introduced for spectroscopic calibration, as shown in Fig. 1.1. Variation of the pulse width and intensity with tuning of wavelength is normalized out by measuring the ratio of the SHG from the sample and the SHG from a z-cut quartz plate in the reference arm. Quartz is chosen here to generate the SHG

for calibration because it is a wide bandgap (8.9 eV) medium [43, 44], thus dispersion of the linear and SHG susceptibility is small in the tuning range. In the reference arm, the polarization configuration is fixed to be p-in/p-out and the orientation of the quartz crystal is fixed at where the SHG signal is maximized as the crystal is rotated about its surface normal. The quartz plate is 1.5 mm thick. For one incident beam, there are two spatially separated linear or SH beams reflected from the plate: one from the front surface and the other from the back surface. The SHG signal reflected from the back surface is used for the spectroscopic calibration, because our measured SHG signal from the back surface is about 500 times stronger than that from the front surface. However, SHG spectroscopic behaviors are about the same for both beams.

Chapter 2

Phenomenological theory of SHG from Si surfaces

2.1 Introduction

The incident beam at frequency ω creates a polarization at the harmonic frequency 2ω, which radiates second-harmonic (SH) light. Nonlinear susceptibility tensors connect the fundamental field and the generated SH field. The tensor elements that are allowed by both symmetry of the medium and geometry of the beams are treated as sources of SH polarization. Using a phenomenological theory, we predict the symmetry properties of rotational-anisotropy SHG (RA-SHG) in reflection from either principal or vicinal Si(001) surfaces. We consider bulk and surface SH contributions and SHG from the electric-field-induced SHG (EFISH) contribution if present. We show that under certain circumstances bulk and surface SH contributions can be separated; moreover, individual tensor elements can be uniquely determined by combining polarization selection and RA-SHG.

2.2 The Model

Consider a laser beam, idealized as single incident plane wave at frequency ω and wave vector $\vec{v}_i$, incident from the ambient with dielectric constant $\varepsilon = 1$ on the medium with $\varepsilon(\omega) \neq 1$ of interest at an angle θ_0, as shown in Fig. 2.1.

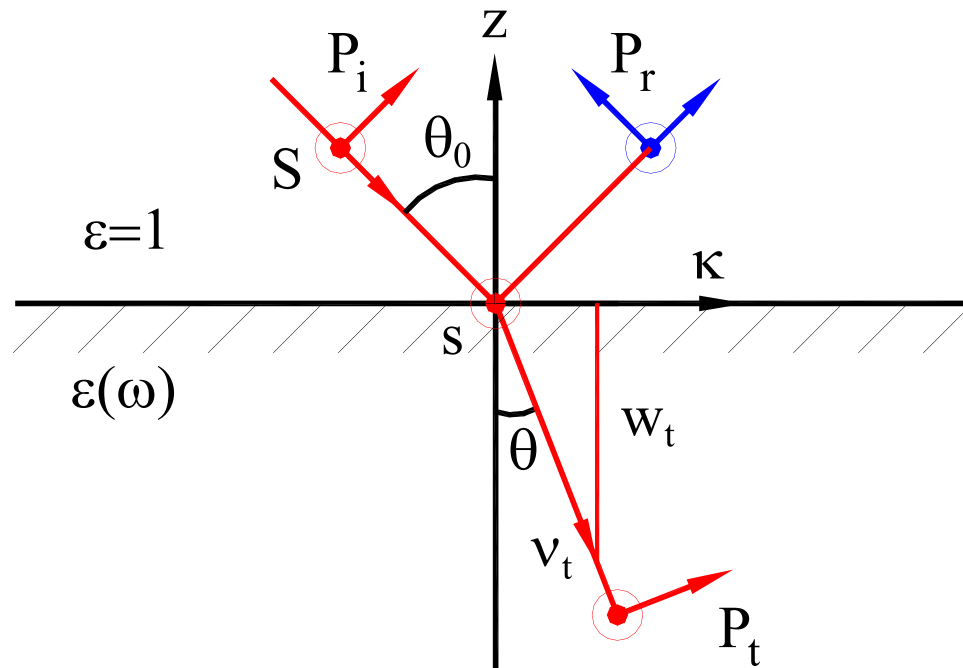

Fig. 2.1. Geometry and unit vectors for the propagating fundamental and SH fields. Note that the diagram assumes that the refractive index of the medium is real.

We study the SH field $\vec{E}^{(2\omega)}$ in reflection geometry. The incident field $\vec{E}_i(\vec{r},t)$, the reflected field $\vec{E}_r(r,t)$, and the transmitted field $\vec{E}_t(\vec{r},t)$ are written in the general form

$$\vec{E}_n(r,t) = \vec{E}_n e^{i\vec{v}_n \cdot \vec{r} - i\omega t} + c.c., \quad (2.1)$$

where the subscript n can be replaced by i, r, or t to represent the incident, the reflected, or the transmitted field, respectively. Each of the amplitudes of the electric fields can be expressed as a superposition of its p- and s-polarized components as

$$\vec{E}_n = E_{np}\hat{p}_n + E_{ns}\hat{s}. \quad (2.2)$$

We take the normal to the surface to be the $\hat{z}$ direction and the wave-vector component perpendicular to $\hat{z}$ as $\vec{\kappa} = \hat{\kappa}|v_i|\sin\theta_0$. In terms of these, the wave vectors for these three fields are

$$\vec{v}_n = \vec{\kappa} - w_n\hat{z}. \quad (2.3)$$

For all three fields, the components of the wave vector normal (w_n) and parallel (κ) to the medium surface are related by

$$w_i = (\tilde{\omega}^2 - \kappa^2)^{1/2} = -w_r, \quad (2.4a)$$

$$w_t = (\tilde{\omega}^2\varepsilon(\omega) - \kappa^2)^{1/2}, \quad (2.4b)$$

where $\tilde{\omega} = \omega / c$ and $\varepsilon(\omega)$ is the dielectric constant of the medium. In Eq. (2.4), we choose the root with $\mathrm{Im}(\omega) \geq 0$, and if $\mathrm{Im}(\omega) = 0$, we take $\mathrm{Re}(\omega) \geq 0$.

The reflected and transmitted fields are obtained from the incident field as

$$\vec{E}_r = (\hat{s}r_s\hat{s} + \hat{p}_r r_p \hat{p}_i)\cdot\vec{E}_i, \quad (2.5a)$$

$$\vec{E}_t = (\hat{s}t_s\hat{s} + \hat{p}_t t_p \hat{p}_i)\cdot\vec{E}_i, \quad (2.5b)$$

where r_s and r_p (t_s and t_p) are the usual Fresnel coefficients of reflection (transmission) from the ambient into the medium for *s*- and *p*-polarized light, respectively,

$$r_s = \frac{w_i - w_t}{w_i + w_t}, \qquad r_p = \frac{w_i\varepsilon(\omega) - w_t}{w_i\varepsilon(\omega) + w_t};$$
$$t_s = \frac{2w_i}{w_i + w_t}, \qquad t_p = \frac{2nw_i}{w_i\varepsilon(\omega) + w_t}, \tag{2.6}$$

while $\hat{p}_t$ is the direction of polarization of *p*-polarized light in the medium given by

$$\hat{p}_t = \frac{\kappa\hat{z} + w_t\hat{\kappa}}{n\widetilde{\omega}} = f_s\hat{z} + f_c\hat{\kappa}\,. \tag{2.7}$$

where $n = \sqrt{\varepsilon(\omega)}$ is the complex refractive index of the medium, and f_s and f_c are the Fresnel factors. Note that if n is real, f_s and f_c are simply the sine and cosine of the angle of beam propagation in the medium, respectively.

We introduce the analogous equations to Eqs. (2.4)-(2.7) for the SH fields, viz.,

$$\begin{aligned}
&\widetilde{\Omega} = \frac{2\omega}{c}, K = 2\kappa, N = \sqrt{\varepsilon(2\omega)},\\
&W_t = [\widetilde{\Omega}^2\varepsilon(2\omega) - K^2]^{1/2}, W_i = [\widetilde{\Omega}^2 - K^2]^{1/2},\\
&\hat{P}_t = \frac{K\hat{z} + W_t\hat{\kappa}}{N\widetilde{\Omega}} = F_s\hat{z} + F_c\hat{\kappa},\\
&\hat{P} = F_s\hat{z} - F_c\hat{\kappa},\\
&T_s = \frac{2W_t}{W_i + W_t}, T_p = \frac{2NW_t}{W_i\varepsilon(2\omega) + W_t}.
\end{aligned} \tag{2.8}$$

Again, if N is real, F_s and F_c are the sine and cosine of the angle of SH beam propagation in the medium. $\hat{P}_t$ and $\hat{P}$ are the directions of polarization of *p*-polarized SH light in the medium and vacuum, respectively. T_s and T_p are the

Fresnel transmission coefficients from the medium into the ambient for *s*- and *p*-polarized SH light, respectively.

The amplitude of the generated SH field in vacuum can be expressed as a superposition of *p*- and *s*-polarized components as

$$\vec{E}^{(2\omega)} = E_p^{(2\omega)}\hat{P} + E_s^{(2\omega)}\hat{s} \ . \tag{2.9}$$

If the dielectric constant of the medium and the wave-vector of the incident beam are known, all of the Fresnel factors and coefficients should be readily calculated using these equations.

2.3 Rotational-anisotropy SHG

2.3.1 Bulk and surface SH contributions

For a centrosymmetric medium, SHG due to the electric dipole response is forbidden in the bulk because of inversion symmetry, but is allowed at the surface because of broken symmetry. At the surface, in addition to the dipole response, a discontinuity in the normal component of the electric field can produce SHG due to the non-local response as well. Both effects have been discussed in details before [26] and combined through the definition of an effective dipole response characterized by a surface susceptibility tensor $\chi_{ijk}^{(2)}$. In the bulk, although SHG due to the dipole response is zero, higher-order terms of polarization, such as the electric quadrupole response [12, 45] give a contribution to SHG, which could be quite significant in comparison with the surface SH contribution. In the presence of an external dc electric field in the medium and at the surface, SHG can have a contribution arising

from dc electric-field-induced SH (EFISH) effect. The EFISH effect should be split into a bulk and a surface contribution, because the symmetry at the surface is different from that in the bulk.

For a centrosymmetric medium, second-order nonlinear polarization $\vec{P}^{(2\omega)}$ at the SH frequency 2ω is given by

$$\vec{P}^{(2\omega)} = \vec{P}^{SD,(2\omega)} + \vec{P}^{BQ,(2\omega)} + \vec{P}^{BE,(2\omega)} + \vec{P}^{SE,(2\omega)} . \qquad (2.10)$$

These four terms correspond to the surface dipole, bulk quadrupole, bulk EFISH, and surface EFISH polarizations, respectively.

The bulk quadrupole response can be written in terms of an effective polarization [24, 27], as

$$P_i^{BQ,(2\omega)}(\vec{r}) = \Gamma_{ijkl}^{(2)} E_j(\vec{r}) \nabla_k E_l(\vec{r}) , \qquad (2.11)$$

where the gradient is determined with respect to the field coordinates and the summation convention is used. $E_i(\vec{r})$ is the fundamental field inside the medium as a function of position $\vec{r}$. $\Gamma_{ijkl}^{(2)}$ is a 4th rank susceptibility tensor that connects the fundamental field and the SH field.

For a crystal with bulk cubic symmetry, such as Si, when the crystal axes are taken to be the standard cubic axes, all distinct elements for the tensor $\Gamma_{ijkl}^{(2)}$ are given by [46]

$$\Gamma_{ijkl}^{(2)} = a_0 \delta_{ijkl} + a_1(\delta_{ij}\delta_{kl} + \delta_{il}\delta_{jk}) + a_2 \delta_{ik}\delta_{jl} , \qquad (2.12a)$$

where a_i are non-zero phenomenological constants. In summation of indices, $\delta_{ij}\delta_{kl}$ implies $i, j \neq k, l$. If such a restriction is eliminated, the tensor is written as

$$\Gamma_{ijkl}^{(2)} = (a_0 - 2a_1 - a_2)\delta_{ijkl} + a_1\delta_{ij}\delta_{kl} + a_1\delta_{il}\delta_{jk} + a_2\delta_{ik}\delta_{jl} . \quad (2.12b)$$

Here, the relation $a_0 \neq 2a_1 + a_2$ holds for cubic symmetric media.

We consider the transformation characteristics of $\Gamma_{ijkl}^{(2)}$ under the symmetry operation of rotating the crystal about its surface normal. The last three terms are all isotropic, because each term keeps it own form under an arbitrary rotation with the transformation matrix R, i.e.,

$$\delta_{ij}\delta_{kl} = R_{io}R_{jp}R_{kq}R_{lr}\delta_{op}\delta_{qr} . \quad (2.13)$$

The first term of Eq. (2.12b) is anisotropic because such an arbitrary rotation operation does not exist in general.

By using Eq. (2.12b), Eq. (2.11) can then be written in the form

$$P_i^{BQ,(2\omega)} = \zeta E_i \nabla_i E_i + a_1 E_i [\nabla \cdot \vec{E}] + a_1 [\vec{E} \cdot \nabla] E_i + \gamma \nabla_i (\vec{E} \cdot \vec{E}) , \quad (2.14)$$

where $E_i = E_i(\vec{r})$ for simplicity and

$$\zeta = a_0 - 2a_1 - a_2 , \qquad \text{and } \gamma = \frac{1}{2} a_2 . \quad (2.15)$$

Notice that Eq. (2.14) is similar to the previous usual form [27], but the second-order nonlinear polarization of magnetic dipole origin is not included here. However, adding of the magnetic dipole effect is equivalent to adjusting of the phenomenological constants.

For excitation of a homogeneous medium by a single transverse plane wave, the middle two terms of Eq. (2.14) are zero, thus, we recover the polarization to the previous results [27]. The bulk susceptibility tensor is split into an isotropic piece, $\Gamma_{ijkl}^{(2),i} = 2\gamma\delta_{ik}\delta_{jl}$, and an anisotropic piece, $\Gamma_{ijkl}^{(2),a} = \zeta\delta_{ijkl}$.

The isotropic nonlinear polarization is given by

$$\vec{P}^{(2\omega),i} = \gamma\nabla(\vec{E}\cdot\vec{E}) = 2i\gamma(\vec{\kappa} - w\hat{z})(E_s^2 + E_p^2)e^{2i(\vec{\kappa}\cdot\vec{R} - wz)}, \tag{2.16}$$

where $\vec{R} = (x, y)$, $\vec{r} = \vec{R} + z\hat{z}$, and $w = w_t$.

The SH fields arising from the bulk isotropic source are identical for all crystal faces and independent of the surface orientation. Following Sipe [27], the generated isotropic fields at 2ω outside of the medium for general linear polarized light and for either *s*- or *p*-polarized harmonic light are

$$E_s^{BQ,(2\omega),i} = 0, \tag{2.17}$$

$$E_p^{BQ,(2\omega),i} = A_0 T_p F_s \gamma(E_s^2 + E_p^2). \tag{2.18}$$

Here $A_0 = 2\pi i\widetilde{\Omega} / NF_c$ is a constant.

2.3.2 RA-SHG from vicinal Si faces

We first study a vicinal surface, which is disoriented by a small angle α from the Si(001) face but still has a mirror plane of symmetry normal to the surface plane, as shown in Fig. 2.2. The offset direction is from the [001] axis toward [110]. For cubic centrosymmetric crystals, Lüpke presented two ways of miscutting to form a surface with symmetry of one mirror plane in the vicinal face [47]: the misorientation from [001] toward [011] and the misorientation from [001] toward [110]. It is important to note that for crystals with diamond structure, which preserve cubic centrosymmetry, the first way of miscut does not produce a vicinal surface with one mirror plane of symmetry.

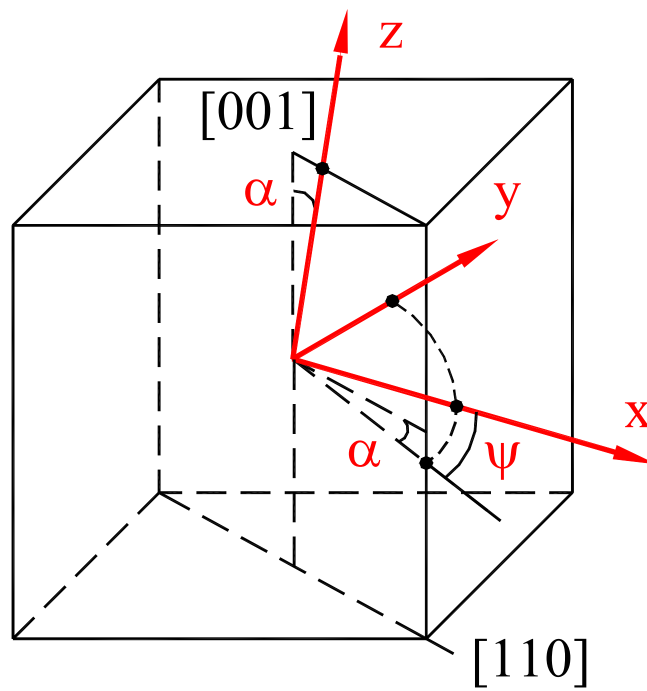

Fig. 2.2. Diagram of the beam frame and the vicinal surface with respect to the cubic crystal axes.

The angles α =0, $\arccos(1/\sqrt{3})$, and $\pi/2$ yield the low-index (001), (111), and (110) crystal faces, respectively; therefore the results of RA-SHG from such a general face is applicable to low-index crystal faces by adjusting the vicinal angle.

To study the transformation properties of anisotropic susceptibility tensors, we establish three coordinate systems. The coordinates ($\hat{x}_0, \hat{y}_0, \hat{z}_0$) are chosen as the natural crystallographic coordinate system corresponding to the [100], [010], and [001] directions, respectively. The coordinates ($\hat{x}_1, \hat{y}_1, \hat{z}_1$) are defined to be the crystallographic directions corresponding to the [110], $[\bar{1}10]$, and [001] directions, respectively. The coordinates $(\hat{x}, \hat{y}, \hat{z})$ are defined to be a fixed beam frame with the $\hat{z}$ axis to be the normal of the macroscopic vicinal surface, as shown in Fig. 2.2. By virtue of these definitions, the azimuthal angle ψ is defined to between $\hat{x}$ and the downward miscut direction.

The susceptibility tensor is transformed from the natural crystallographic coordinates to the final beam coordinates following three steps. First, is the rotation of coordinate counterclockwise about the $\hat{z}_0$ axis by an angle $\psi_0 = 45^\circ$ from the coordinates ($\hat{x}_0, \hat{y}_0, \hat{z}_0$) to ($\hat{x}_1, \hat{y}_1, \hat{z}_1$) with the transformation matrix

$$R_z(\psi_0) = \begin{bmatrix} \cos(\psi_0) & \sin(\psi_0) & 0 \\ -\sin(\psi_0) & \cos(\psi_0) & 0 \\ 0 & 0 & 1 \end{bmatrix}. \tag{2.19}$$

Second, is the rotation counterclockwise about the $\hat{y}_1$ axis by an angle α from ($\hat{x}_1, \hat{y}_1, \hat{z}_1$) to $(\hat{x}, \hat{y}, \hat{z})$ when ψ =0 following the transform matrix

$$R_y(\alpha)=\begin{bmatrix}\cos(\alpha) & 0 & -\sin(\alpha)\\ 0 & 1 & 0\\ \sin(\alpha) & 0 & \cos(\alpha)\end{bmatrix}. \qquad (2.20)$$

Third, is the rotation of coordinate counterclockwise about the $\hat{z}$ axis for an angle ψ from the coordinates $(\hat{x},\hat{y},\hat{z})$ when ψ =0 to the coordinates $(\hat{x},\hat{y},\hat{z})$ when ψ >0. The transform matrix is $R_z(\psi)$, which has the same matrix form as $R_z(\psi_0)$ but with a different rotation angle. Thus, the final transformation matrix is the ordered product of the three matrixes, written as

$$R = R_z(\psi)R_y(\alpha)R_z(\psi_0)\,. \qquad (2.21)$$

The tensor $\Gamma^{(2),a}_{opqr}$ in the crystallographic coordinate is transformed to $\Gamma'^{(2),a}_{ijkl}$ in the beam coordinate according to the tensor transformation rule

$$\Gamma'^{(2),a}_{ijkl} = R_{io}R_{jp}R_{kq}R_{lr}[\Gamma^{(2),a}_{opqr}]\,. \qquad (2.22)$$

With respect to the final beam coordinates $(\hat{x},\hat{y},\hat{z})$, we obtain the bulk anisotropic nonlinear polarization

$$P_i^{(2\omega),a}(\vec{r}) = \Gamma'^{(2)}_{ijkl}\,\vec{E}'_j(\vec{r})\nabla'_k\,\vec{E}'_l(\vec{r})\,. \qquad (2.23)$$

Following Sipe [27, 48], the SH fields outside of the medium generated with a half-space filled with air (or vacuum) are calculated. For simplicity, the polarizations of both the fundamental and harmonic fields are limited to *s* and *p*. The notation *(g, h)* is established to represent *g* polarized fundamental and *h* polarized harmonic radiation, where *g* and *h*=*s* or *p*.

For the (*g, p*) cases, the SH fields $E_{g,p}^{BQ,(2\omega),a}$ arising from bulk anisotropic quadrupole source are

$$E_{g,p}^{BQ,(2\omega),a} = A_0 T_p \zeta \Gamma [b_{00,(g,p)}^{BQ} + \sum_{m=0}^{4} b_{m,(g,p)}^{BQ} \Phi_m(\alpha)\cos(m\psi)][E_g^{(\omega)}]^2 ,$$

(2.24a)

and for the (*g, s*) cases, the SH fields are

$$E_{g,s}^{BQ,(2\omega),a} = A_0 T_s \zeta \Gamma [\sum_{m=1}^{4} b_{m,(g,s)}^{BQ} \Phi_m(\alpha)\sin(m\psi)][E_g^{(\omega)}]^2 . \quad (2.24b)$$

Here, $\Gamma = n\widetilde{\Omega}/8(2w_t + W_t)$. $\Phi_m(\alpha)$ are the angular functions for the specific misorientation as shown in Fig. 2.2, which are listed in Table 2.1 in the same form as that from Lüpke [47]. The coefficients $b_{00,(g,h)}^{BQ}$ and $b_{m,(g,h)}^{BQ}$ are the combinations of Fresnel factors specific to each Fourier coefficient, as listed in Table 2.2. These results are from a complete and systematic calculation rather than a repeat of previous report [47].

Table 2.1. Angular functions $\Phi_m(\alpha)$

$\Phi_0(\alpha)$	$\frac{1}{32}[25 + 4\cos(2\alpha) + 3\cos(4\alpha)]$
$\Phi_1(\alpha)$	$\frac{1}{16}[2\sin(2\alpha) + 3\sin(4\alpha)]$
$\Phi_2(\alpha)$	$-\frac{1}{16}[1 - 4\cos(2\alpha) + 3\cos(4\alpha)]$
$\Phi_3(\alpha)$	$-\frac{1}{16}[14\sin(2\alpha) - 3\sin(4\alpha)]$
$\Phi_4(\alpha)$	$-\frac{1}{32}[7 + 28\cos(2\alpha) - 3\cos(4\alpha)]$

Table 2.2. $b^{BQ}_{00,(g,h)}$ and $b^{BQ}_{m,(g,h)}$ as functions of Fresnel factors

	(s, s)	*(p, s)*	*(s, p)*	*(p, p)*
b^{BQ}_{00}	*0*	*0*	$4f_cF_s$	$4[F_cf_s(-2f_c^2+f_s^2)+F_sf_c(f_c^2-3f_s^2)]$
b^{BQ}_{0}	*0*	*0*	$F_cf_s-4f_cF_s$	$F_cf_s(11f_c^2-4f_s^2)-4F_sf_c(f_c^2-4f_s^2)]$
b^{BQ}_{1}	$3f_c$	$f_c(f_c^2-6f_s^2)$	$-f_cF_c-f_sF_s$	$F_cf_c(10f_s^2-3f_c^2)+F_sf_s(4f_s^2-11f_c^2)]$
b^{BQ}_{2}	f_s	$f_s(5f_c^2-2f_s^2)$	$-2f_cF_s$	$2F_cf_s(f_s^2-3f_c^2)+2F_sf_c(f_c^2-2f_s^2)]$
b^{BQ}_{3}	$-f_c$	$f_c(f_c^2-2f_s^2)$	$f_cF_c+f_sF_s$	$f_c(-f_c^2F_c+2F_cf_s^2-f_cf_sF_s)]$
b^{BQ}_{4}	f_s	$-f_c^2f_s$	$-F_cf_s$	$f_c^2F_cf_s$

We apply the formalism of the bulk anisotropic SHG to calculate the analogous equations for bulk EFISH in reflection with emphasis on dependence of the EFISH field on crystal symmetry. To our knowledge, a theoretical expression for the EFISH effect in the bulk of a medium has not been developed. The bulk dc field induced dipole polarization can be written phenomenologically as,

$$P_i^{BE,(2\omega)} = \chi^{(3)}_{ijkl}E_jE_k^dE_l \ , \qquad (2.25)$$

where $\vec{E}^d$ is the dc electric field, which is a function of normal position measured from the surface and directed along the surface normal, written as $\vec{E}^{\mathrm{d}}(z)=\hat{z}E^d(z)$.

For a cubic centrosymmetric medium, when the coordinate axes are taken to be the standard cubic axes, $\chi^{(3)}_{ijkl}$ preserves the same symmetry properties as $\Gamma^{(2)}_{ijkl}$, and it is written as,

$$\chi^{(3)}_{ijkl} = (b_0-2b_1-b_2)\delta_{ijkl} + b_1(\delta_{ij}\delta_{kl}+\delta_{il}\delta_{jk}) + b_2\delta_{ik}\delta_{jl}\,. \qquad (2.26)$$

Equation (2.25) can be written in the form

$$P_i^{BE,(2\omega)} = \zeta^d E_i E_i^d E_i + \eta^d E_i (\vec{E}^{\mathrm{d}} \cdot \vec{E}) + \gamma^d E_i^d (\vec{E} \cdot \vec{E}), \quad (2.27)$$

where

$$\zeta^d = b_0 - 2b_1 - b_2, \eta^d = 2b_1, \text{ and } \gamma^d = \frac{1}{2} b_2 . \quad (2.28)$$

Notice that there is a difference between the bulk quadrupole and the bulk EFISH polarizations. The middle term of the latter is non-zero in general, even for excitation of a homogeneous medium by a single transverse plane wave. The SH polarization arising from the middle term is isotropic, written as

$$\vec{P}^{BE,(2\omega),\eta,i} = \eta^d \vec{E}(\vec{E}^d \cdot \vec{E}) = E^d(z) f_s \eta^d E_p \vec{E} . \quad (2.29)$$

The generated fields at 2ω from this source outside of the medium for either *s*- or *p*-polarized harmonic light are

$$E_s^{BE,(2\omega),\eta,i} = A_0 T_s \Gamma^d f_s \eta^d E_p E_s , \quad (2.30a)$$

$$E_p^{BE,(2\omega),i} = A_0 T_p \Gamma^d f_s F_s \eta^d E_p^2 . \quad (2.30b)$$

Here, $\Gamma^d = \int_{-\infty}^{0} E^d(z) \exp[-i(2w_t + W_t)z] dz$ and the integration is over the half infinite medium.

Similarly, the polarization arising from the last term is

$$\vec{P}^{BE,(2\omega),\gamma^d,i} = \gamma^d \vec{E}^d (\vec{E} \cdot \vec{E}) = \gamma^d \vec{E}^d (E_s^2 + E_p^2) e^{2i(\vec{\kappa}\cdot\vec{R} - wz)} , \quad (2.31)$$

and the generated fields at 2ω from this source outside of the medium for either *s*- or *p*-polarized harmonic light are

$$E_s^{BE,(2\omega),\gamma^d,i} = 0 , \quad (2.32a)$$

$$E_p^{BE,(2\omega),\gamma^d,i} = A_0 T_p \Gamma^d F_s \gamma^d (E_s^2 + E_p^2) . \quad (2.32b)$$

For the anisotropic term and with the polarization of the fundamental and harmonic fields limited to *s* and *p* states, the calculation proceeds the same way as bulk quadrupole SH source. For the (*g, p*) cases, the SH fields $E_{g,p}^{BE,(2\omega),a}$ arising from anisotropic EFISH source are

$$E_{g,p}^{BE,(2\omega),a} = A_0 T_p \zeta^d \Gamma^d [b_{00,(g,p)}^d + \sum_{m=0}^{3} b_{m,(g,p)}^d \Phi_m(\alpha)\cos(m\psi)][E_g^{(\omega)}]^2 \quad ,$$

(2.33a)

and for the (*g, s*) cases, the SH fields are

$$E_{g,s}^{BE,(2\omega),a} = A_0 T_s \zeta^d \Gamma^d [\sum_{m=1}^{3} b_{m,(g,s)}^d \Phi_m(\alpha)\sin(m\psi)][E_g^{(\omega)}]^2 \quad .$$

(2.33b)

Here, $b_{00,(g,h)}^d$ and $b_{m,(g,h)}^d$ are the combinations of Fresnel factors specific to each Fourier coefficient, as listed in Table 2.3.

Table 2.3. $b_{00,(g,h)}^d$ and $b_{m,(g,h)}^d$ as functions of Fresnel factors

	(s, s)	*(p, s)*	*(s, p)*	*(p, p)*
b_{00}^d	*0*	*0*	$4F_s$	$4(-2F_c f_c f_s + f_c^2 F_s - f_s^2 F_s)$
b_0^d	*0*	*0*	$-4F_s$	$-4(-2F_c f_c f_s + f_c^2 F_s - 2f_s^2 F_s)$
b_1^d	*3*	$f_c^2 - 4f_s^2$	$-F_c$	$-3f_c^2 F_c + 4F_c f_s^2 - 8f_c f_s F_s$
b_2^d	*0*	$4f_c f_s$	$-2F_s$	$2f_c(-2F_c f_s + f_c F_s)$
b_3^d	f_c^2	f_c^2	F_c	$-f_c^2 F_c$

Symmetry properties of the bulk SH contribution are predicted from the above calculation. Now we consider the surface SH contribution. The SH polarization arising from the surface dipole response is given by

$$P_i^{SD,(2\omega)} = \chi_{ijk}^{S,(2)} E_j E_k \tag{2.34}$$

For a surface with one mirror plane of symmetry, with the $\hat{y}$ axis perpendicular to the plane of symmetry, Eq. (2.34) can be rewritten in the usual piezoelectric contracted notation as [49, 50]

$$\begin{bmatrix} P_x^{(2\omega)} \\ P_y^{(2\omega)} \\ P_z^{(2\omega)} \end{bmatrix} = \begin{bmatrix} \partial_{11} & \partial_{12} & \partial_{13} & 0 & \partial_{15} & 0 \\ 0 & 0 & 0 & \partial_{24} & 0 & \partial_{26} \\ \partial_{31} & \partial_{32} & \partial_{33} & 0 & \partial_{35} & 0 \end{bmatrix} \times \begin{bmatrix} E_x^{\ 2} \\ E_y^{\ 2} \\ E_z^{\ 2} \\ 2E_y E_z \\ 2E_x E_z \\ 2E_x E_y \end{bmatrix}, \tag{2.35}$$

where ∂_{mn} are independent tensor elements of $\chi_{ijk}^{S,(2)}$. Note that the $\hat{x}$ axis should also be specified to relate the surface to the bulk susceptibilities. For the vicinal Si surface, the $\hat{x}$ axis is toward the downward miscut direction when $\psi = 0$, as shown in Fig. 2.2.

For the ideal low-index (001) surface under perfect flatcut condition, the ∂_{mn} simplify considerably to only the nonzero elements, $\partial_{31}, \partial_{32}, \partial_{15}, \partial_{24}$, and ∂_{33}. For a practical Si(001) surface, to a good approximation it is macroscopic fourfold symmetric; therefore, these nonzero elements can be simplified again to $\partial_{31} = \partial_{32}, \partial_{15} = \partial_{24}$, and ∂_{33} [27].

With the fundamental and SH beams limited to *s*- or *p*-polarized states, the SH fields $E_{g,h}^{SD,(2\omega)}$ for the (*g, p*) cases are

$$E_{g,p}^{SD,(2\omega)} = A_0 T_p [\sum_{m=0}^{3} s_{m,(g,p)}^{SD} \cos(m\psi)][E_g]^2 , \tag{2.36}$$

and for the (*g, s*) cases are

$$E_{g,s}^{SD,(2\omega)} = A_0 T_s [\sum_{m=1}^{3} s_{m,(g,s)}^{SD} \sin(m\psi)][E_g]^2 . \tag{2.37}$$

Here, $s_{m,(g,h)}^{SD}$ are the combinations of Fresnel factors and independent tensor elements, as listed in Table 2.4. In the table, the following expressions have been introduced for notational convenience [47]:

$$\begin{aligned} \partial_{11}^{(1)} &= \frac{1}{4}(3\partial_{11} + \partial_{12} + 2\partial_{26}), \\ \partial_{12}^{(1)} &= \frac{1}{4}(\partial_{11} + 3\partial_{12} - 2\partial_{26}), \\ \partial_{11}^{(3)} &= \frac{1}{4}(\partial_{11} - \partial_{12} - 2\partial_{26}). \end{aligned} \tag{2.38}$$

Table 2.4. $s_{m,(g,h)}^{SD}$ as combinations of Fresnel factors and tensor elements

	(s, s)	*(p, s)*	*(s, p)*	*(p, p)*
s_0^{SD}	*0*	*0*	$\frac{1}{2}\varepsilon(2\omega)F_s(\partial_{31}+\partial_{32})$	$\varepsilon(2\omega)F_s[f_s^2\partial_{33}+\frac{1}{2}f_c^2(\partial_{31}+\partial_{32})]-F_cf_cf_s(\partial_{15}+\partial_{24})$
s_1^{SD}	$\partial_{11}^{(1)}$	$f_c^2\partial_{12}^{(1)}+f_s^2\partial_{13}$	$-F_c\partial_{12}^{(1)}$	$2\varepsilon(2\omega)F_sf_cf_s\partial_{35}-F_c[f_s^2\partial_{13}+f_c^2\partial_{11}^{(1)})$
s_2^{SD}	*0*	$f_cf_s(\partial_{15}-\partial_{24})$	$-\frac{1}{2}\varepsilon(2\omega)F_s(\partial_{31}-\partial_{32})$	$\frac{1}{2}\varepsilon(2\omega)F_sf_c^2(\partial_{31}-\partial_{32})-F_cf_cf_s(\partial_{15}-\partial_{24})$
s_3^{SD}	$-\partial_{11}^{(3)}$	$f_c^2\partial_{11}^{(3)}$	$F_c\partial_{11}^{(3)}$	$-f_c^2F_c\partial_{11}^{(3)}$

If there is a dc electric field at the surface (or interface), SHG has a contribution from the surface EFISH polarization $\vec{P}^{SE,(2\omega)}$, given by

$$P_i^{SE,(2\omega)} = \chi_{ijkl}^{S,(3)} E_j E_k^d E_l \, . \qquad (2.39a)$$

At the surface or interface, the symmetry is different from in the bulk. The dc field here is limited to the surface normal direction. Considering the small size of the interfacial region, we treat the EFISH polarization as a surface effect by integrating the *z*-dependent variables across the interfacial layer, written as

$$P_i^{d,s,(2\omega)} = \int_I \chi_{ij3k}^{s,(3)}(z) E_3^d(z) dz E_j E_k = M_{ijk}^{S,(2)} E_j E_k \, . \qquad (2.39b)$$

If $\chi_{ijkl}^{S,(3)}$ is a mathematical tensor, the new variable $M_{ijk}^{S,(2)}$ is not a tensor, strictly speaking; however, it possesses the same symmetry properties as $\chi_{ijk}^{S,(2)}$ when the symmetry operation is limited to rotation about the surface normal. Therefore, the surface EFISH effect can be combined into the surface SH without the dc field by defining a new set of field-dependent tensor elements ∂_{mn}^d and adding them one by one to the field-independent tensor ∂_{mn}, written as $\partial_{mn} + \partial_{mn}^d$. The symmetry properties of the rotational-anisotropy SHG should be the same with or without the EFISH effect.

The total SH field $E_{g,h}^{(2\omega)}$ arising from both the bulk and surface for the (*g, p*) cases are

$$E_{g,p}^{(2\omega)} = [\sum_{m=0}^{4} C_{m,(g,p)} \cos(m\psi)][E_g]^2 \, , \qquad (2.40a)$$

and for the (*g, s*) cases are

$$E_{g,s}^{(2\omega)} = [\sum_{m=1}^{4} C_{m,(g,s)} \sin(m\psi)][E_g]^2 . \qquad (2.40b)$$

The fourfold Fourier coefficient C_4 is unique in that it originates from only anisotropic bulk quadrupole contribution. The SH intensity $I^{(2\omega)}$ is proportional to the magnitude squared of the SH field, written as $I^{(2\omega)} \propto |E^{(2\omega)}|^2$.

2.3.3 RA-SHG from the Si(001) face

In calculating SHG from vicinal Si surfaces, the polarizations of both the fundamental and the SH fields are limited to either s or p in order to simplify the expressions of the SH fields for a complicated surface susceptibility tensor. In contrast, for the Si(001) surface, the surface susceptibility tensor is much simpler than that of vicinal surfaces; therefore, we consider a general linear polarization configuration for both the fundamental and the SH fields. The notation $(\Delta\alpha, \Delta\beta)$ is introduced to represent a specific linear polarization configuration, as shown in Fig. 2.3, where $\Delta\alpha$ represents the polarization direction of the incident field $\vec{E}_0(\Delta\alpha)$ that is an angle $\Delta\alpha$ counterclockwise from its s-polarization, and $\Delta\beta$ represents the polarization of the SH field $\vec{E}^{(2\omega)}(\Delta\beta)$ that is an angle $\Delta\beta$ counterclockwise from its s-polarization. Here, counterclockwise is with respect to the forward beam propagation direction.

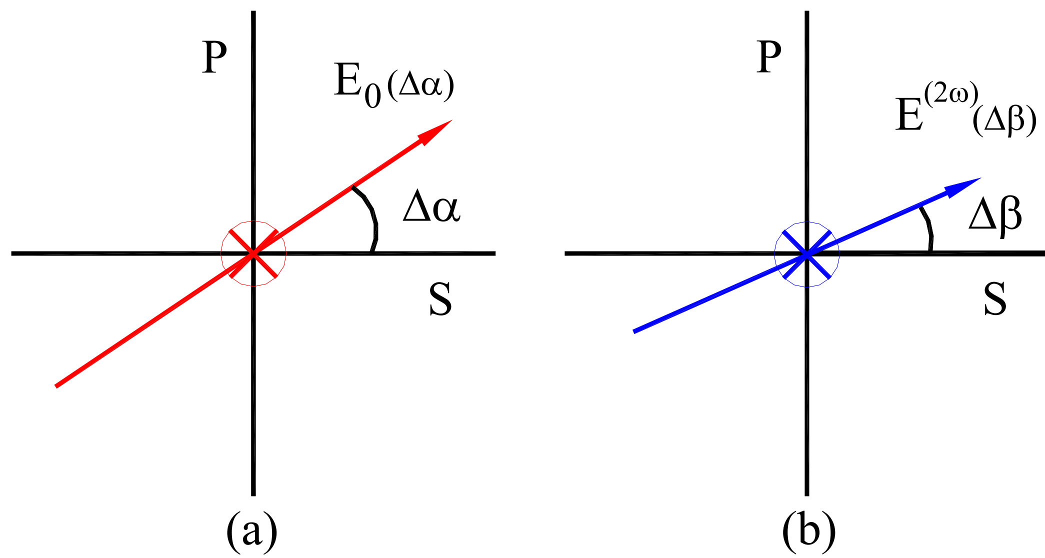

Fig. 2.3. Definition of the linear polarization configuration with the incident fundamental beam (a) and the reflected SH beam (b).

Under the excitation of a $\Delta\alpha$ polarized fundamental beam, the generated *s*-polarized SH field due to the bulk anisotropic source is

$$E_{\Delta\alpha,s}^{(2\omega),ani} = A_0 T_s \Gamma \zeta f_s \{-f_c t_s t_p \sin(2\Delta\alpha) + [t_s^{\ 2}\cos^2(\Delta\alpha) - f_c^{\ 2} t_p^{\ 2}\sin^2(\Delta\alpha)]\sin(4\phi) + f_c t_s t_p \sin(2\Delta\alpha)\cos(4\phi)\}[E_0]^2, \quad (2.41a)$$

and the generated *p*-polarized SH field is

$$E_{\Delta\alpha,p}^{(2\omega),ani} = A_0 T_p \Gamma \zeta f_s \{[F_c t_s^{\ 2}\cos^2(\Delta\alpha) + (3F_c f_c^{\ 2} + 4F_s f_s f_c) t_p^{\ 2}\sin^2(\Delta\alpha)] + f_c F_c t_s t_p \sin(2\Delta\alpha)\sin(4\phi) - F_c[t_s^{\ 2}\cos^2(\Delta\alpha) - f_c^{\ 2} t_p^{\ 2}\sin^2(\Delta\alpha)]\cos(4\phi)\}[E_0]^2 .$$

(2.41b)

Here, ϕ is the azimuthal angle between the [100] crystal axis and the incident plane.

For the $(\Delta\alpha, \Delta\beta)$ polarization, the total SH field arising from bulk anisotropic source is

$$E_{\Delta\alpha,\Delta\beta}^{(2\omega),ani} = E_{\Delta\alpha,s}^{(2\omega),ani}\cos(\Delta\beta) + E_{\Delta\alpha,p}^{(2\omega),ani}\sin(\Delta\beta) . \quad (2.42)$$

The isotropic SH field arising from both bulk and surface sources is written together as

$$E_{\Delta\alpha,\Delta\beta}^{(2\omega),iso} = (A_0 T_s \partial_{15} f_s t_s t_p \sin(2\Delta\alpha)\cos(\Delta\beta) + A_0 T_p \{[\varepsilon(2\omega)\partial_{31} + \gamma]F_s[t_s^{\ 2}\cos^2(\Delta\alpha) + t_p^{\ 2}\sin^2(\Delta\alpha)] + [\varepsilon(2\omega)(\partial_{33} - \partial_{31})F_s f_s^{\ 2} - 2\partial_{15} f_s F_c f_c] t_p^{\ 2}\sin^2(\Delta\alpha)\}\sin(\Delta\beta))[E_0]^2$$

. (2.43)

Thus, the total SH field under the $(\Delta\alpha, \Delta\beta)$ polarization is

$$E_{\Delta\alpha,\Delta\beta}^{(2\omega)} = E_{\Delta\alpha,\Delta\beta}^{(2\omega),ani} + E_{\Delta\alpha,\Delta\beta}^{(2\omega),iso} . \quad (2.44)$$

In case that there is an EFISH effect, we treat it as an additional SH contribution. The surface EFISH field is easily treated by replacing ∂_{15}, ∂_{31}, and ∂_{33} with $\partial_{15} + \partial_{15}^d$, $\partial_{31} + \partial_{31}^d$, and $\partial_{33} + \partial_{33}^d$, respectively.

For the $(\Delta\alpha, \Delta\beta)$ polarization, the bulk EFISH field is calculated following Green's function formalism [48, 51], written as

$$E^{BE,(2\omega)}_{\Delta\alpha,\Delta\beta} = (A_0 T_s \Gamma^d \eta^d f_s t_s t_p \sin(2\Delta\alpha)\cos(\Delta\beta) + A_0 T_p \Gamma^d F_s \{\gamma^d [t_s{}^2 \cos^2(\Delta\alpha) + t_p{}^2 \sin^2(\Delta\alpha)] + (2\eta^d f_s + f_s{}^2 \zeta^d) t_p{}^2 \sin^2(\Delta\alpha)\} \sin(\Delta\beta))[E_0]^2 .$$

(2.45)

2.4 Separation of bulk and surface SH contributions

Using SHG as a surface-specific probe for centrosymmetric materials is based on the fact that SHG is forbidden under the dipole approximation in the bulk but allowed at the surface. The involvement of a bulk SH contribution complicates the interpretation of SHG data. Separation of bulk and surface contributions is a problem of fundamental importance if one intends to use SHG as a strict surface probe. Great effort has been put on the bulk-surface discrimination [26, 52, 53], but it has been shown that it is fundamentally difficult under certain circumstances, even for static medium properties [28]. If there exists any time-dependence of SHG or EFISH effect, discrimination of different SH contributions would be considerably complicated. The theoretical predictions also show that there is no advantage in using vicinal Si surfaces to distinguish different SH contributions because the surface susceptibility tensor for vicinal surfaces is much complicated.

For simplicity, we consider SHG from a flatcut Si(001) face without any time-dependent effect of SHG and EFISH effect. If all of the five independent tensor elements ζ, γ, ∂_{15}, ∂_{31}, and ∂_{33} are known, SH response from the Si(001) surface would be fully determined, and then different SH contributions would be neatly

separated. We consider here the possibilities of separation of these elements by combining polarization selection and RA-SHG. From our theoretical predictions, the h-polarized SH fields $E_{g,h}^{(2\omega)}$ are related to the g-polarized incident fundamental fields E_g by the following equations,

$$E_{g,s}^{(2\omega)} = a_{4,(g,s)} \sin(4\phi) e^{i\delta_{g,s}} E_g^2 , \tag{2.46}$$

$$E_{g,p}^{(2\omega)} = [a_{0,(g,p)} + a_{4,(g,p)} \cos(4\phi)] e^{i\delta_{g,p}} E_g^2 , \tag{2.47}$$

where the polarization (g or h) of both fields is limited to be s or p. On the other hand, for a special polarization (q, s), this relation takes the form,

$$E_{q,s}^{(2\omega)} = [a_{0,(q,s)} + a_{4,(q,s)}^{s} \sin(4\phi) + a_{4,(q,s)} \cos(4\phi)] e^{i\delta_{q,s}} E_q^2 . \tag{2.48}$$

Here, the letter q (-q) represents the linear polarization that is 45° counterclockwise (clockwise) from s when facing in the propagation direction.

The Fourier coefficients in Eqs. (2.46)-(2.48) are functions of susceptibility tensor elements and linear optical preparation factors, as shown in Eqs. (2.41)-(2.43). We choose the anisotropic coefficient a_4 be positive and real (with its phase included in $\delta_{g,h}$), then the isotropic term a_0 is complex in general and can be split into real and imaginary parts, written as $a_0 = a_{0,r} + ia_{0,i}$. Because all of the a_4 's for different polarizations are a function of the bulk anisotropic tensor element ζ , they are related by linear optical coefficients. The SH intensity is proportional to the magnitude square of the SH field. For cubic centrosymmetric media, ζ is usually nonzero, so is a_4. From Eq. (2.46), the (p, s) or (s, s) RA-SHG intensity should show eightfold symmetry. From Eqs. (2.47) and (2.48), the (p, p), or (s, p), or (q, s) RA-SHG

intensity may show either eightfold or fourfold symmetry, depending on whether $a_{0,r}$ is zero or not. For the (*p, p*) polarization, if the RA-SHG intensity shows fourfold symmetry, the peak locations of RA-SHG discerns the sign of $a_{0,r}$, i.e., if a peak appears at ϕ=0°, $a_{0,r} > 0$, and if a peak appears at ϕ=45°, $a_{0,r} < 0$.

From one scan of either (*s, s*) or (*p, s*) RA-SHG signal, the absolute value of ζ can be determined by fitting the RA-SHG to Eq. (2.46). We note that it also possible to avoid the ζ SH contribution by combining polarization and RA-SHG, for example, by measuring the (*s, p*) polarized SH signal at a fixed azimuthal angle ϕ=0°. The relative phase between the SH field and fundamental field is unknown from only intensity measurement. The surface tensor element ∂_{15} is determined from the (*q, s*) RA-SHG signal with the known ζ. For the (*q, s*) polarized RA-SHG, bulk and surface SH contributions can be strictly separated in theory. As shown in Eq. (2.43), ∂_{31} and γ are always together, thus thorough separation of ∂_{31}, γ, and ∂_{33} is impossible from this theory. However, if the γ contribution is negligible, ∂_{31} is determined from (*s, p*) RA-SHG, and then ∂_{33} is determined from (*p, p*) RA-SHG.

The anisotropic coefficient $a_{4,(p,s)}$ can be obtained from fitting the measured (*p, s*) RA-SHG signal to Eq. (2.46), the remaining $a_{4,(g,h)}$ of other polarizations and $a^{s}_{4,(q,s)}$ are derived using optics coefficients that take into account linear propagation and beam geometry. Both the real part ($a_{0,r}$) and the imaginary part ($a_{0,i}$) of a_0 can be extracted from the measured RA-SHG signals using Eqs. (2.47) and (2.48); however, the value of a_0 can not be uniquely determined by only one scan of RA-

SHG. For example, both $a_{0,r} \pm ia_{0,i}$ give the same RA-SHG intensity as shown from Eq. (2.47), i.e.,

$$|E_{g,p}^{(2\omega)}|^2 = |[a_{0,r,(g,p)} \pm ia_{0,i,(g,p)} + a_{4,(g,p)}\cos(4\phi)]E_g^2|^2 \quad (2.49)$$

We present a theoretical method to solve the ambiguity in fit coefficients by combining two scans of differently polarized RA-SHG signals. By subtracting the *(-q, s*) RA-SHG signal from the (*q, s*) RA-SHG signal, as shown from Eqs (2.41)-(2.44), we obtain the difference between these two scans of RA-SHG signal, which is proportional to

$$\begin{aligned} |E_{q,s}^{(2\omega)}|^2 - |E_{-q,s}^{(2\omega)}|^2 = \{&4[a_{0,r,(q,s)} + a_{4,(q,s)}\cos(4\phi)]a_{4,r,(q,s)}^s \sin(4\phi) \\ &+ 4a_{0,i,(q,s)}a_{4,i,(q,s)}^s \cos(4\phi)\}|E_q^4| \end{aligned} \quad . \quad (2.50)$$

This is a linear function of the fit coefficients $a_{0,r,(q,s)}$ and $a_{0,i,(q,s)}$; therefore, ∂_{15} can be uniquely determined. To determine ∂_{31} uniquely, which is impossible from only one scan of the (*s, p*) RA-SHG, we need combine a differently polarized scan of RA-SHG. A convenient example is subtracting the (*s, -q*) polarized RA-SHG signal from the (*s, q*) polarized RA-SHG signal, then we obtain a similar linear fit equation as Eq. (2.50). Similarly, by combining appropriate RA-SHG scans ∂_{33} can be determined uniquely.

2.5 Summary

We have used a phenomenological theory of SHG to predict the symmetry properties of RA-SHG from Si surfaces. Four SH sources (surface dipole, bulk quadrupole, surface EFISH, and bulk EFISH) have been systematically calculated. For vicinal Si(001) surfaces, the polarizations of both the fundamental and harmonic

fields were limited to *s* or *p* in the calculation. For the Si(001) surface, we considered configurations of mixed linear polarization.

Both the surface dipole and surface EFISH contributions can be combined into an effective surface dipole response, which is isotropic for the Si(001) surface but anisotropic for vicinal Si(001) surfaces. The bulk EFISH effect, which is characterized by ζ^d, η^d, and γ^d, can not be combined into the bulk quadrupole response, which is characterized by ζ and γ. The ζ contribution is anisotropic for both major and vicinal Si(001) surfaces, but the ζ^d contribution is anisotropic for vicinal Si(001) surfaces but isotropic for the Si(001) surface. The remaining tensor elements η^d, γ^d, and γ are all isotropic.

For the Si(001) surface, we showed that bulk and surface SH contributions can be separated exactly both in theory and in experiment by combining polarization selection and RA-SHG. In addition, we presented methods of uniquely determining both the amplitude and the phase of individual susceptibility tensor elements from RA-SHG scans.

Compared with other crystalline Si surfaces, the Si(001) surface is characterized by the simplest surface susceptibility tensor. Furthermore, for the Si(001) surface, it is possible to separate out or eliminate the bulk anisotropic SH contribution, which is independent of surface conditions and can be used as a reliable reference signal for surface SHG. Both properties are significant advantages of using the Si(001) surface for SHG studies.

Chapter 3

Bulk and surface contributions to resonant SHG

3.1 Introduction

Surface SHG has proven to be a powerful diagnostic technique for studying the properties of buried Si-SiO_2 interfaces [29, 54], which are important to semiconductor technology. It has been shown that SHG is very sensitive to medium surface conditions, such as crystal orientation [24], miscut [55, 56], and roughness [56-58]. It is also well known that SHG is sensitive to laser parameters, such as polarization and wavelength [33, 59]. Thus, care must be taken when interpreting results or inter-comparing published results.

The SHG signal from Si(001) consists of a strong electric-dipole allowed contribution from the surface (or interface) and a weaker one due to the electric-quadrupole and magnetic-dipole terms in the bulk [60] (also see Chapter 2). The expectation that the bulk contribution is relatively independent of surface conditions suggests that it can be used as a reference to aid in comparison between samples, as has been done in studying the effect of interface roughness [56-58]. However, by combining spectroscopic and rotational-anisotropy SHG (RA-SHG) measurements, we have discovered that the bulk contribution displays resonant behavior. This was not reported in earlier spectroscopic studies of SHG from oxidized [33, 59] or hydrogen terminated [61] silicon. The resonant behavior must be accounted for if the bulk contribution is used as a reference to compare samples. Furthermore, the bulk

contribution can interfere with the surface contribution, thereby shifting the apparent resonance position for data taken at a single azimuthal angle [33, 59].

The SHG response is described by nonlinear optical susceptibility tensors that connect the generated signal to the electric field of the incident beam, as shown in Chapter 2. Ideally, it would be possible to completely measure all of the tensor elements of the susceptibility tensors that describe the bulk and surface contributions. For spectroscopic measurements, the variation of the tensor elements as function of the photon energy of the emitted (or incident) light would be measured. However, it is fundamentally difficult to separate the isotropic bulk and surface contributions [28]. Nevertheless, by careful use of RA-SHG in combination with polarization selective SHG, we are able to provide some separation of the tensor elements, which improves comparison among samples. While full phase information can be obtained by dispersion detection with a reference [62] or by homodyne detection with a reference [63], we can obtain relative phase information from our simpler experiment. We observe that the isotropic response, which includes contribution from both surface and bulk, displays a resonance that is sensitive to surface preparation. The two photon resonant energy is 3.39 eV for native oxide silicon (NO-Si), while it shifts to 3.35 eV for a thermal oxide (TO-Si) sample. The anisotropic component, which in a simple picture is only due to the bulk, has a resonance at 3.42 eV, for NO-Si, TO-Si, and hydrogen terminated Si (H-Si). Prior work observed resonances around 3.3 eV and ascribed them to the E_1 critical point (CP) due to the band structure of bulk silicon with a red shift due to sub-interface strain of the Si-Si bonds by the oxide layer [33]. Based on studying the effect of surface modification, this earlier work concluded that

the resonance was purely in the surface contribution and not due to the bulk contribution. This is contrary to our conclusions based on RA-SHG; however, we can explain this difference as arising from interfering surface and bulk contributions that can distort the spectroscopic results taken for a single azimuthal angle.

3.2 Bulk and surface SHG contributions

In bulk crystalline Si, SHG arises only from the nonlocal response characterized by two phenomenological constants ζ and γ, which are anisotropic and isotropic respectively [27]. SHG from a (001) surface or interface is isotropic. These symmetry properties are systematically presented in Chapter 2. With the polarizations limited to s and p states, we write the total SH fields $E_{g,h}^{(2\omega)}$ from a Si(001) crystal face as

$$E_{g,p}^{(2\omega)}(\phi) = [a_{0,(g,p)}e^{i\theta_{g,p}} + a_{4,(g,p)}\cos(4\phi)]e^{i\delta_{g,p}}E_g^2, \qquad (3.1)$$

$$E_{g,s}^{(2\omega)}(\phi) = a_{4,(g,s)}\sin(4\phi)e^{i\delta_{g,s}}E_g^2. \qquad (3.2)$$

Here, E_g is the incident fundamental field, and ϕ is the azimuthal angle between the incident plane and [100] direction in the sample surface plane. The notation (*g, h*) represents *g* polarized fundamental and *h* polarized harmonic radiation, where *g* and *h* = *s* or *p*. The SHG intensity $I_{g,h}^{(2\omega)}(\phi)$ is proportional to the magnitude square of the SH field, i.e., $I_{g,h}^{(2\omega)}(\phi) \propto |E_{g,h}^{(2\omega)}(\phi)|^2$. Both θ and δ provide phase information, but δ is irrelevant when only the intensity is measured. The constants a_0 and a_4 are the magnitudes of the isotropic and anisotropic contributions to the RA-SHG signal, respectively. They are determined by the relevant susceptibility elements, Fresnel

factors, and dielectric functions. The dependence of a_4 on the laser frequency, ω, involves only ζ and two dielectric functions $\varepsilon(\omega)$ and $\varepsilon(2\omega)$, as shown in Chapter 2. It can be written as

$$a_{4,(g,h)}(\omega) = f_{(g,h)}(\zeta(\omega), \varepsilon(\omega), \varepsilon(2\omega)) = L_{(g,h)}(\omega) \,|\, \zeta(\omega) \,|\,, \quad (3.3)$$

where $L_{(g,h)}(\omega)$ is a function of frequency arising from linear optics. The polarization dependence in a_4 and L results from the geometry of experiment.

3.3 Sample preparation and experimental method

The samples were prepared from the same undoped (ρ >20 $\Omega \cdot$cm), on-axis Si(001) wafer. The NO-Si sample, covered with 2 nm thick native oxide, was investigated as received from the manufacturer. The TO-Si sample was prepared by oxidation of chemically cleaned NO-Si at 1000 ^{o}C in a dry oxygen atmosphere to yield an oxide of 14 nm thickness. Before the thermal oxidation process, natively oxidized Si wafers were cleaned followed the standard the RCA cleaning process [64]. Two H-Si samples were obtained by dipping NO-Si and TO-Si samples in an NH_4F:HF buffered oxide etch (BOE). The durations of the BOE were controlled, so that oxides were just removed but the samples were not over-etched [65]. The difference in the SH signals from these two H-terminated samples are negligible, so we do not distinguish between them.

The experimental setup is described in detail in Chapter 1. We used a modelocked laser with ~150 fs pulse width, 76 MHz repetition rate, and wavelength tunable from 700 to 810 nm. The ~60 mW beam was focused to <30 μm on the samples at 45° incident angle. During the experiment, the samples were held in a

chamber purged by dry N_2 to reduce the charging effect [66] and oxidation of the H-Si samples. The SHG signals in reflection were detected by photomultiplier tubes with 1 sec gate time. The SHG spectra were calibrated against the SHG signal in reflection from a quartz sample. The uncertainty at each point is estimated by taking multiple scans and calculating the standard deviation at each point. These uncertainty estimates are then used in the fitting procedure to estimate the uncertainty of the fit coefficients. The uncertainty in the photon energy is due to the laser bandwidth, which was measured at each wavelength and varies between 20 and 30 meV (two-photon energy). Error bars are omitted in the figures if they are smaller than the plot symbol.

3.4 Experimental results

3.4.1 Spectroscopic results of the bulk anisotropic contribution

To separate out the bulk anisotropic contribution, we use a combination of polarization and RA-SHG. For Si(001) surfaces, the anisotropic coefficient, a_4, is only due to the bulk while the isotropic coefficient, a_0, is mainly due to the surface, but includes a weak bulk contribution. To provide a clean measurement of the bulk anisotropic contribution, we measured RA-SHG in the (*p, s*) configuration as a function of photon energy. The spectra obtained this way showed negligible dependence on surface modification. The spectrum of $a_{4,(p,s)}$ for NO-Si is shown in Fig. 3.1, which shows a peak at 3.42 eV two-photon energy. Using Eq. (3.3), we can obtain a spectrum for $\zeta(\omega)$. The function $L_{(p,s)}(\omega)$ is calculated using the phenomenological theory in Chapter 2 and tabulated values for the dielectric

functions of crystalline silicon [67]. $L_{(p,s)}(\omega)$ displays a weak minimum around 3.35 eV, which shifts the resonance of $\zeta(\omega)$ compared to that of $a_{4,(p,s)}$, yielding a peak at 3.38 eV for $\zeta(\omega)$ as shown in Fig. 3.1. This resonance energy is between the $E_0^{'}$ CP energy of 3.33 eV and E_1 CP energy of 3.42 eV [68], which suggests contributions from both critical points. We note that the data in Fig. 3.1 are normalized so that $a_{4,(s,s)}$(3.26 eV) = 1 by using Eq. (3.3), i.e., the appropriate ratios of $L_{(g,h)}$. All peak positions have an uncertainty of ±0.01 eV due to the laser bandwidth in the vicinity of the peaks.

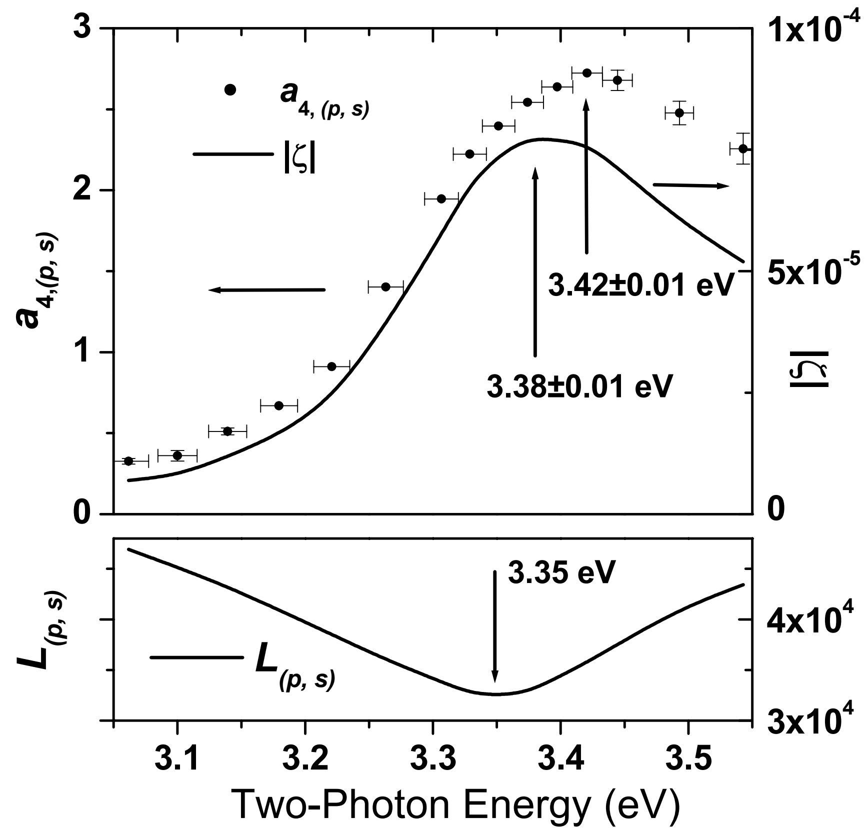

Fig. 3.1. Spectra of the anisotropic SHG contribution $a_{4,(p,s)}$ (normalized to $a_{4,(s,s)}$ at 3.26 eV), the linear optics coefficient $L_{(p,s)}$ and the magnitude ($|\zeta|$) of the anisotropic element ζ. The normalization of $a_{4,(p,s)}$ determines the magnitude of $|\zeta|$. The vertical error bars come from data fitting and the horizontal error bars come from the laser bandwidth.

3.4.2 Spectroscopic results of the isotropic contribution

Based on this measurement of the spectrum of the anisotropic bulk component from $a_{4,(p,s)}$, we obtain the spectrum of $a_{4,(p,p)}$ by using the calculated spectrum of $L_{(p,s)}$ and $L_{(p,p)}$. Combined with measured (*p, p*) polarized RA-SHG spectrum, this allows us to accurately determine both the amplitude and relative phase of the isotropic component, which includes an inseparable combination of bulk and surface contributions. Previous spectral measurements have not used a combination of (*p, s*) and (*p, p*) measurements but rather only the latter [69, 70]. However, we find the fits to the RA-SHG data are not robust when only (*p, p*) data are used, resulting in a large uncertainty in the fit coefficients. Typical RA-SHG data at a two-photon energy of 3.26 eV (fundamental wavelength of 760 nm) for all three samples are shown in Fig. 3.2. Clearly the azimuthal dependence of the RA-SHG signal for H-Si displays a phase shift with respect to the other two signals. This is indicative of a phase shift of the isotropic response with respect to the anisotropic bulk response, which is confirmed by our analysis. Based on complex phasor notation, we designate the quadrature components of the isotropic response with respect to the anisotropic bulk response as $a_{0,r}$ and $a_{0,i}$, i.e., $a_{0,r} + ia_{0,i} = a_{0,(g,p)}e^{i\theta_{g,p}}$ in Eq. (3.1). This conveniently breaks the isotropic response into interfering ($a_{0,r}$) and non-interfering ($a_{0,i}$) components. Note that there is an ambiguity in sign of $a_{0,i}$ obtained from our analysis.

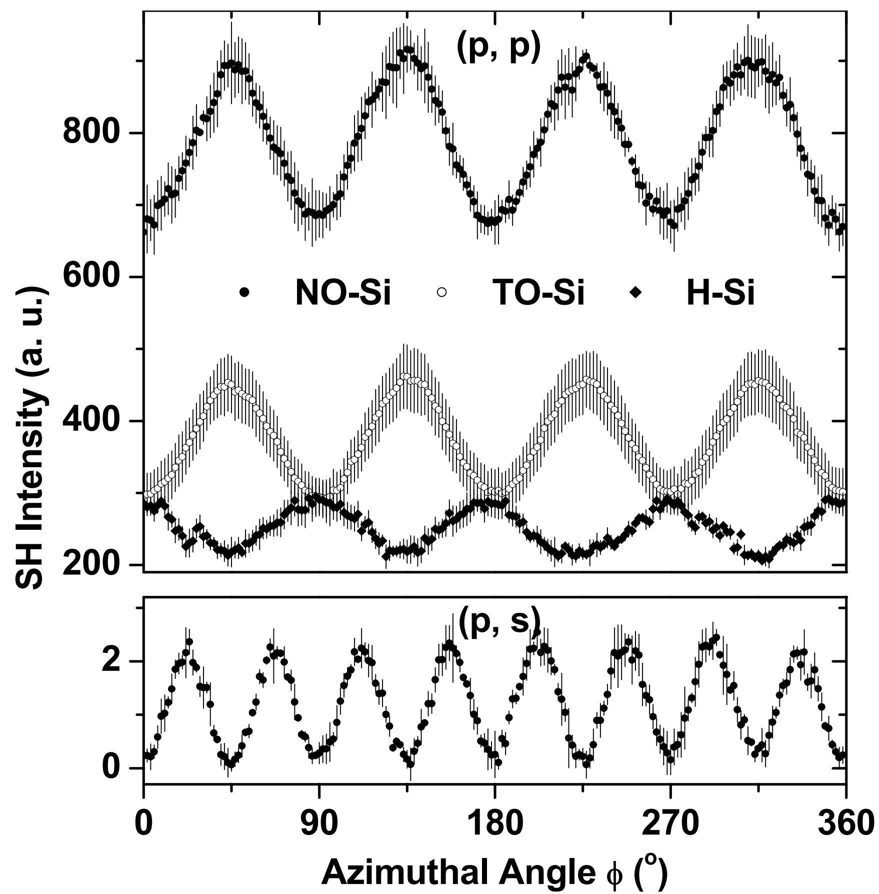

Fig. 3.2. RA-SHG intensities from modified Si(001) surfaces (NO-Si, TO-Si and H-Si) at a two-photon energy of 3.26 eV for different polarization configurations: (*p, p*), top panel and (*p, s*), bottom panel. The error bars are the standard deviation obtained from averaging successive scans.

The spectra of $a_{0,r}$ (for NO-Si and TO-Si), $a_{0,r}$ and $a_{0,i}$ (for H-Si) are shown in Fig. 3.3. The measurements show that for NO-Si and TO-Si $\theta \sim \pi$, thus $a_{0,i}$ is negligible and $a_{0,r} < 0$ (we actually plotted $-a_{0,r}$). The $a_{0,r}$ for NO-Si peaks at two-photon energy of 3.39 eV, while for TO-Si, it peaks at 3.35 eV. Both of these show a shift to lower energy as compared to the bulk resonance, with a larger shift for the thicker oxide. The shift direction is consistent with previous results [33, 59]. As expected from the phase shift in Fig. 3.2, $a_{0,r}$ for H-Si is opposite sign (> 0) as compared to the oxide samples. In addition, the non-interfering quadrature, $a_{0,i}$, is comparable in magnitude to $a_{0,r}$ for H-Si although their relative strength varies with photon energy.

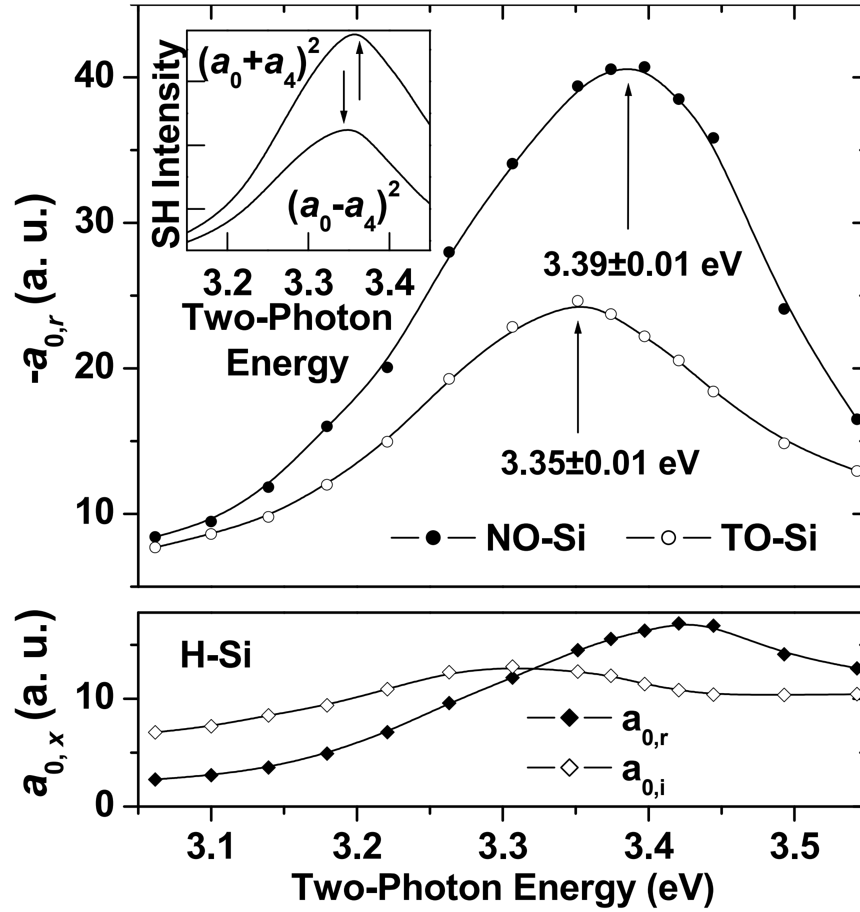

Fig. 3.3. Spectra of the isotropic amplitudes $a_{0,r}$ for NO-Si and TO-Si (top panel) and the interfering and non-interfering isotropic amplitudes $a_{0,r}$ and $a_{0,i}$ for H-Si (bottom panel). The inset in the top panel shows the resonance energy shift due to interference between a_0 and a_4 for TO-Si for fixed azimuthal angles of 0° (a_0-a_4) and 45° (a_0+a_4). The uncertainties in energy are the same as Fig. 3.1.

3.5 Discussion

The stronger signal for the NO-Si, as compared to the TO-Si, is in part due to an induced electric field across the Si-SiO_2 interface [66]. This occurs because photo-excited electrons become trapped in the oxide or at the interface, yielding a time-dependent enhancement of the signal. In the NO-Si sample, this enhancement happens within a few seconds, and thus can cause a significant enhancement within the 1 second gate time of the photon-counting electronics. In the TO-Si sample, the enhancement takes tens of seconds to occur and thus is weak within the 1 sec gate time (the rotation brings a new portion of the sample into the focal spot for each measurement). It is important to note that the enhancement itself also displays resonant behavior, which further complicates interpretation of the spectrum obtained for a sample with a thin oxide. The original work on this time-dependent increase observed that it is enhanced when oxygen was present in the ambient [66]. Based on this, we used a nitrogen purge to try to reduce the effect, but nevertheless observe a strong time-dependent signal on resonance. This suggests that additional processes may contribute to the time-dependent enhancement for on-resonance excitation.

The remarkable phase difference of the SHG signal from the H-Si sample, compared to the oxidized samples, is indicative of the different properties of the hydrogen terminated surface compared to an oxidized surface. An ideal truncated Si surface would be electrically neutral; however the electronic structure is modified by the presence of hydrogen or oxygen, which have differing electronegativity. The peak of the signal for H-Si sample is very close to that of the bulk anisotropic response, consistent with a lack of the strain present in the oxidized samples.

The interference between the bulk anisotropic term and the isotropic terms can cause a shift in the apparent resonance position of the SHG signal if spectral data are only taken at a single azimuthal angle, as has been done in some experiments [33, 59]. This arises because of the shift between the bulk resonance and the surface resonance. As illustrated in the inset to Fig. 3.3, the peak position for the net resonance depends on whether the interference is constructive or destructive. Although a small shift, it can be comparable to the shifts due to sample preparation. Furthermore, the π phase shift of $a_{0,r}$ between oxidized silicon and H-Si may lead to misleading conclusions about the relative strength of the SHG signals for data taken at a fixed angle.

3.6 Summary

We have used a careful combination of rotational anisotropy SHG and polarization dependent SHG from Si(001) samples to separate anisotropic bulk terms from isotropic terms, which are dominated by the surface. This shows that the bulk response does display a resonance. Using this information, we are then able to identify the amplitude and phase of the isotropic terms. A bulk anisotropic resonance is observed at a two-photon energy of 3.42 eV, which results from the interaction of the bulk susceptibility tensor element ζ (peak at 3.38 eV) and linear optical propagation factors. The isotropic surface contributions for native oxide Si and thermal oxide Si show peaks at 3.39 eV and 3.35 eV, respectively. Interference between these contributions and the bulk signal can shift the apparent resonance position if they are not separated. Oxidation clearly induces a red shift of the resonance relative to the bulk, which is ascribed to interface strain induced by the

oxide layer. For the (*p, p*) polarization, oxidized surfaces only produce a signal that interferes with the anisotropic bulk signal, whereas H-Si produces both interfering and non-interfering (in-quadrature) signals. Furthermore, there is a phase shift between the interfering terms for oxidized Si as compared to H-Si. These effects can modify the apparent spectrum obtained for a fixed azimuthal angle.

Chapter 4

Phase inversion in rotational-anisotropy SHG

4.1 Introduction

We present the observation of phase inversion in RA-SHG signals. Specifically, the azimuthal angle at which a peak occurs in the RA-SHG signal switches to being one at which a valley occurs. The phase inversion can be induced by either tuning the energy of the incident photons or by surface modification, specifically the phase of H-terminated Si is inverted with respect to that of oxidized silicon at certain photon energies. The phase inversion is observed for the specific polarization configuration of *s* polarized incident light and detection of the *p* polarized SH. Such phase inversion in the presence of an applied electric field across the interface in metal-oxide-silicon structures has been reported for (*p*, *p*) polarization [69, 71]. RA-SHG phase inversion, without an applied electric field but rather induced by a combination of tuning of the photon energy and proper selection of the polarization configuration, has not been presented previously. We ascribe the phase inversion as function of photon energy to the presence of a resonance in the surface contribution. Because the phase is actually a relative phase between surface and bulk contributions, we conclude that this resonance must be purely a surface state that does not arise from the bulk band structure. Earlier spectroscopic studies have found resonances with this nature [59]. Furthermore, by comparing (*s, p*) data to (*q, s*) data, it is possible to distinguish the resonant behavior of ∂_{15} from that of ∂_{31}. The phase inversion due to H-termination is attributed to the change in interfacial electronic

structure as compared to the Si-SiO_2 interface. This is most pronounced for (*s, p*) polarization, although we have also observed it for (*p, p*) polarization, as shown in Chapter 3.

4.2 Experimental conditions and sample preparation

The experimental setup was the same as described in Chapter 1. RA-SHG curves were obtained by rotating the sample about the surface normal. The azimuthal angle is defined as being between plane of incidence and the [100] crystal direction. The same three samples as that in Chapter 3 were studied. They are a native oxide Si (NO-Si), a thermal oxide Si (TO-Si), and a hydrogen terminated Si (H-Si). All were prepared from the same undoped Si(001) wafer.

4.3 Observed phase inversions

4.3.1 Phase inversion due to photon energy variation

The (*s, p*) RA-SHG curves for the TO-Si and NO-Si samples are shown in Fig. 4.1 for a range of two-photon energies between 3.40 and 3.52 eV. The phase inversion is obvious between the curves for the lowest and highest photon energies, specifically the location of a peak in one corresponds to a valley in the other. By taking finer steps in photon energy, we can observe the phase inversion taking place. Most strikingly, we observe eightfold symmetry at one specific photon energy for each oxidized sample. Aside from the intensity, we find that the appearance of the RA-SHG signal depends sensitively on the photon energy.

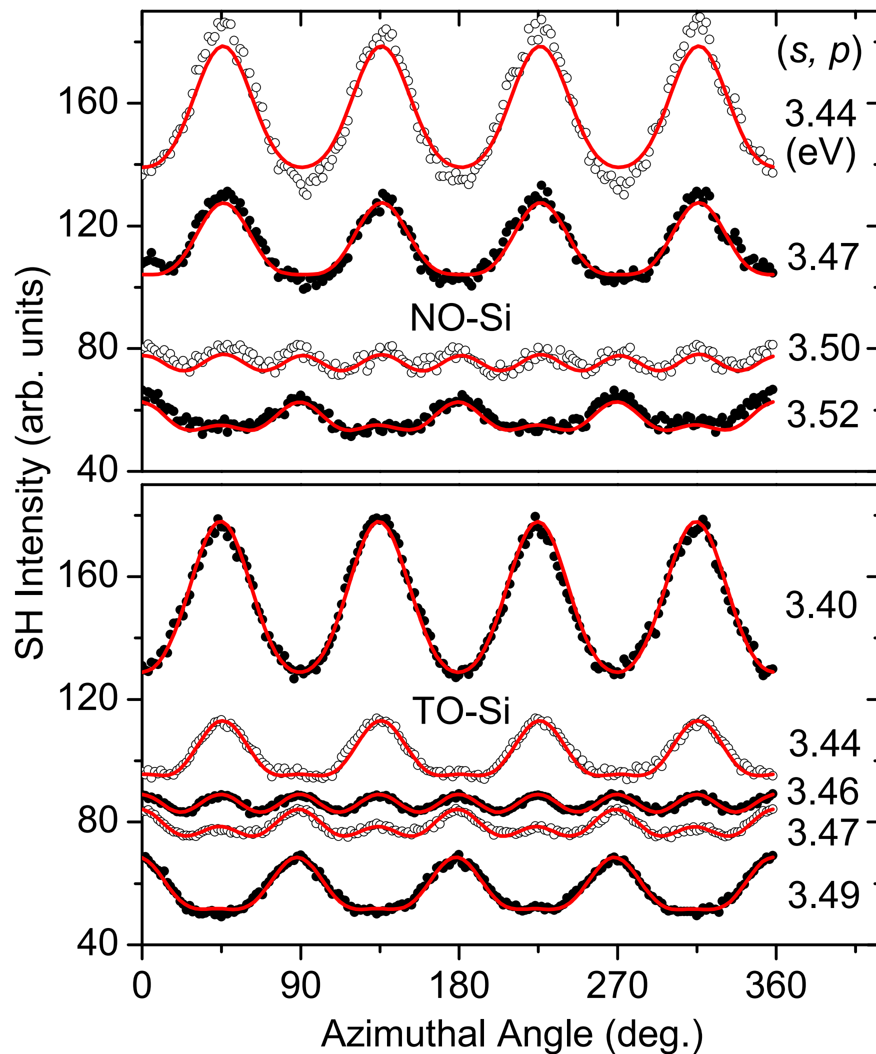

Fig. 4.1. RA-SHG signals from both NO-Si and TO-Si samples for the polarization (*s, p*) at several two-photon energies. The vertical displacement reflects the changing signal strength with two-photon energy. Note that the RA-SHG signals show eightfold symmetry at 3.50 and 3.46 eV for the NO-Si and TO-Si samples, respectively. The solid lines show the fits.

4.3.2 Phase inversion due to surface modification

In Fig. 4.2, we show the RA-SHG curves for all three samples at a fixed two-photon energy of 3.26 eV for both (*s, p*) and (*q, s*) polarization configurations. Here we observe that for both polarizations the phase of the H-Si sample is inverted compared to that of either oxidized sample. We have also observed that this happens for (*p, p*) polarization in Chapter 3 as well. To verify that doping does not play a role, we have also taken data on NO-Si samples with *n* and *p* doped substrates. They have the same phase as the oxidized samples shown in Fig. 4.2.

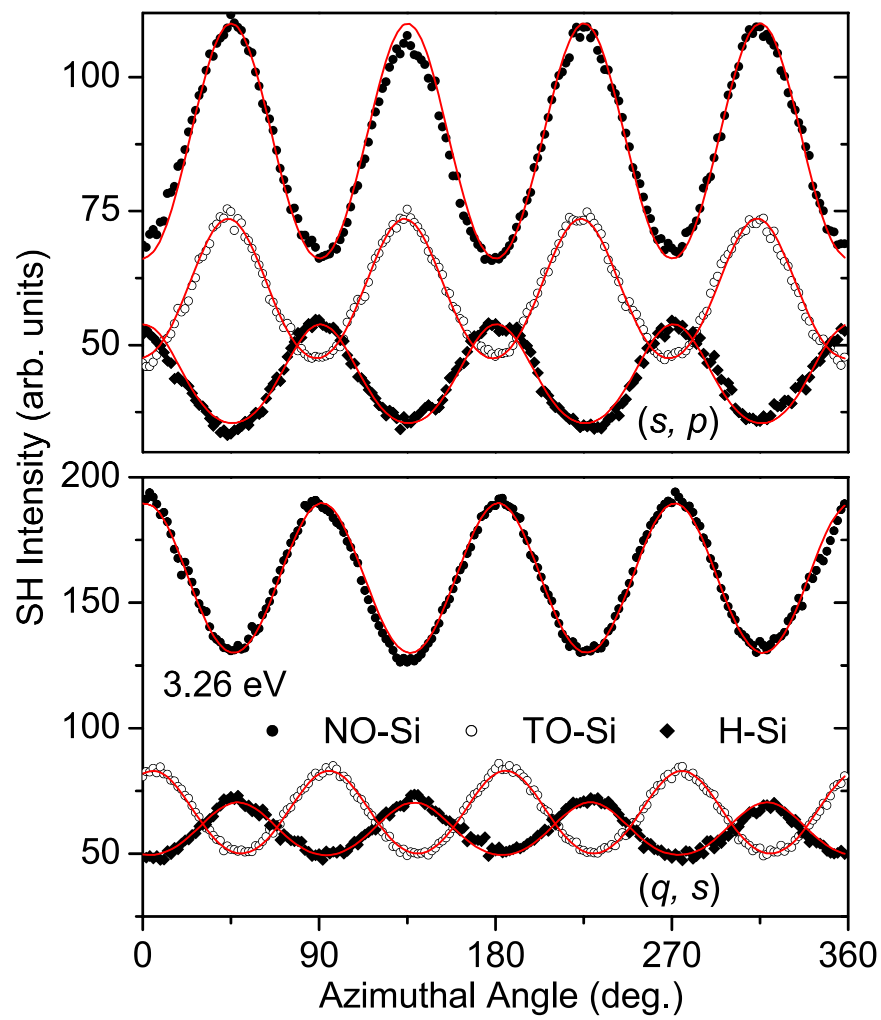

Fig. 4.2. RA-SHG intensities from modified Si(001) surfaces (NO-Si, TO-Si, and H-Si) at a two-photon energy of 3.26 eV for different polarizations: (*s, p*), top panel, and (*q, s*), bottom panel. Solid lines show the fits.

4.4 Phase and amplitude of susceptibility tensors

To analyze the RA-SHG data, we fit the curves to theoretical predictions from Chapter 2, which shows that the SH field, $E_{g,h}^{(2\omega)}$, is related to the incident field, E_g, by

$$E_{s,p}^{(2\omega)} = [a_{0(s,p)} + a_{4(s,p)} \cos(4\phi)] e^{i\theta_{(s,p)}} E_s^2 , \quad (4.1)$$

$$E_{q,s}^{(2\omega)} = [a_{0(q,s)} + a'_{4(q,s)} \sin(4\phi) + a_{4(q,s)} \cos(4\phi)] e^{i\theta_{(q,s)}} E_q^2 , \quad (4.2)$$

where ϕ is the azimuthal angle, the $a_{n(g,h)}$'s are the fit coefficients describing the anisotropic bulk component, $a_{4(g,h)}$, and the isotropic component that includes both bulk and surface contributions, $a_{0(g,h)}$. The intensity of the measured SH signal is proportional to the magnitude squared of the SH fields given in Eq. (4.1) or (4.2). The $a_{4(g,h)}$ coefficients are related to each other by expressions that only involve the linear optical properties, as shown in Chapter 2. We find that the most robust procedure is to obtain $a_{4(p,s)}$ from (*p, s*) data (not shown), which suppresses isotropic contributions, and then use the values of $a_{4(s,p)}$, $a_{4(q,s)}$ and $a'_{4(q,s)}$ derived from $a_{4(p,s)}$ in fitting the other data. The bulk anisotropic contribution was utilized as a phase reference and therefore we choose $a_{4(g,h)}$ to be real and positive by including its phase, $\delta_{4(g,h)}$, in $\theta_{(g,h)}$. Since $\theta_{(g,h)}$ represents an overall phase, our intensity measurements are insensitive to it. The relative phase between the bulk and surface contribution is included by allowing $a_{0(g,h)}$ to be complex. For a given polarization configuration, we write $a_{0(g,h)} = |a_{0(g,h)}| e^{i\delta_{0(g,h)}}$, i.e., in terms of the magnitude and phase relative to the

anisotropic bulk component. Note that we do not determine the sign of the imaginary part of $a_{0(g,h)}$, which makes the sign of $\delta_{0(g,h)}$ ambiguous. The eightfold symmetry occurs when $a_{0(g,h)}$ is exactly 90° out of phase with $a_{4(g,h)}$, in which case there is no cross term when the intensity is calculated from Eqs. (4.1) and (4.2). The cross term has the fourfold symmetry observed in most of the traces, whereas the eightfold symmetry arises from taking the square of the $\cos(4\phi)$ terms. Similarly, an eightfold symmetry is observed in (*p, s*) data where the isotropic term is suppressed entirely, also eliminating the cross term.

Based on the theory, the fit coefficients can be related to the susceptibility tensor elements. Although the actual equations, as shown in Eqs. (2.41)-(2.43) in Chapter 2, are complicated, it is sufficient to note that $a_{0(q,s)}$ is a function of the surface element ∂_{15} and the bulk element ζ, while $a_{0(s,p)}$ is a function of the linear combination of surface and bulk elements $\varepsilon(2\omega)\partial_{31}+\gamma$ and the bulk element ζ, where $\varepsilon(2\omega)$ is the complex dielectric constant at the frequency of the SH. The advantage of these two polarization configurations is that they isolate the two surface tensor elements ∂_{15} and ∂_{31}, whereas (*p, p*) yields a combination of elements. Also, since we observe that the data for the (*s, p*) configuration strongly depends on surface modification, we can make some separation of ∂_{31} and γ, because the latter is insensitive to the surface. Specifically, the phase inversion of the (*s, p*) signal with surface modification leads us to conclude that it is dominated by ∂_{31}; thus we ignore γ in our analysis. It has been shown fundamentally that such a separation cannot be done otherwise [28].

The phase and amplitude of ∂_{15} and ∂_{31} as a function of two-photon energy obtained from the fitting are shown in Fig. 4.3 for all three samples. The phase angles of ζ, ∂_{15}, and ∂_{31} are designated by δ_{ζ}, δ_{15}, and δ_{31}, respectively. Since there is ambiguity in the sign of the imaginary part of $a_{0(g,h)}$, we plot both possible values of the phases at each two-photon energy. Note that, in principle, the sign ambiguity in the fit coefficients can be lifted so that the phases of ∂_{31} and ∂_{15} can be determined uniquely, as shown in Eq. (2.50) in Chapter 2. However this requires virtually perfect polarization alignment and a better signal to noise ratio than we achieved in most of our data. By choosing to make $a_{4(g,h)}$ real and positive, we are measuring the phases of ∂_{15} and ∂_{31} with respect to the phase of the bulk component ζ. To obtain these tensor elements from the fit coefficients, we have calculated the linear optical coefficients from published values for the linear optical susceptibility of silicon [67]. These coefficients are complex, i.e., they result in phase shifts, thus the point of phase inversion in the signal does not correspond to 90° phase difference between the tensor elements. Furthermore, it means that two possible phase angles are not just different by a minus sign.

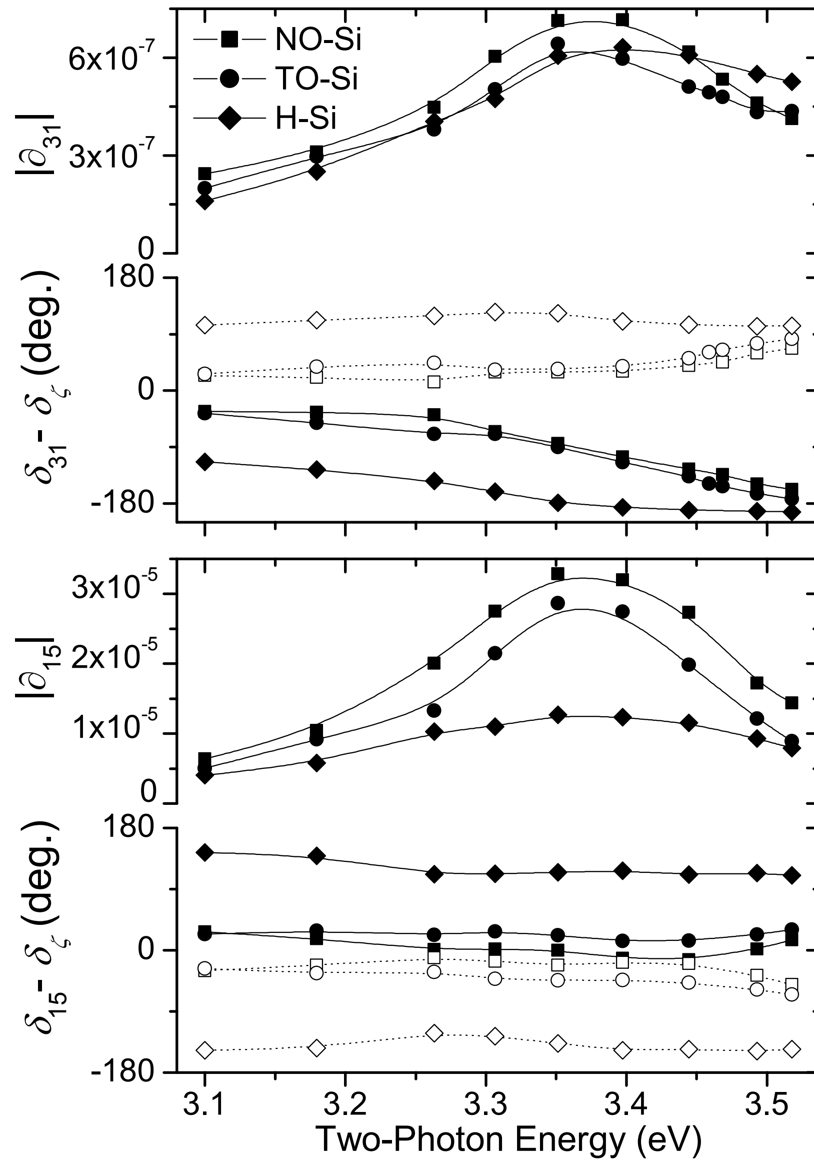

Fig. 4.3. Spectra of the amplitudes and relative phases of the tensor elements ∂_{31} (upper panel) and ∂_{15} (lower panel) for all three samples: TO-Si, NO-Si and H-Si. The amplitudes are normalized so that $a_{4(s,s)} = 1$ at 3.26 eV. Both possible phases, arising from the ambiguity in the sign of the imaginary part of the fit coefficient, are plotted as open and filled symbols. Lines are to guide the eye.

4.5 Discussion

Comparing the present experimental results of SHG spectroscopy with the previous microscopic theory of SHG at Si(001) surfaces [35], we find some agreement in the resonant energy but considerable discrepancy in the magnitudes of the surface susceptibility tensor elements. Previous microscopic theories [34, 35] usually neglected the bulk SH contribution, but our results show it may significantly alter the SH spectroscopy through interference effect. From this point of view, some previous consistences between theory and experiment should be revised. For the Si-SiO_2 interface, we show here that SHG spectroscopy is sensitive to the sample preparation conditions and the sample azimuthal angle, and we will show in Chapter 6 that it is also sensitive to the polarization configuration. Therefore, a feasible microscopic theory to calculate the SH spectrum from a realistic Si-SiO_2 interface would be hard to develop and to apply to various circumstances. For hydrogen-terminated surfaces, however, the SH spectra of ∂_{15} , ∂_{31} , and ∂_{33} have been calculated microscopically [35]; therefore, we can conveniently compare them to our experimental results. The theory and our experimental results are in agreement with that the (*p, p*) polarized SH contributions from all three surface tensor elements are comparable. However, our measured relative magnitude of ∂_{15} and ∂_{31} is very different from the theoretical prediction. Our results show that $|\partial_{31}|$ is about two orders of magnitudes smaller than $|\partial_{15}|$, but the microscopic theory predicted that ∂_{15}, ∂_{31}, and ∂_{33} are all comparable in magnitude. As evident in Fig. 4.2, the (*s, p*) and (*q, s*) SH intensities, which are due to ∂_{31} and ∂_{15}, respectively, are comparable

because the SH intensity is proportional to the susceptibility multiplied by its radiation factors, and not the bare susceptibility alone. Our observed peak energies of the magnitudes of ∂_{31} and ∂_{15} are very close to the theoretical prediction.

The data show the clear trend that δ_{31} varies significantly with respect to δ_{ζ}, for increasing photon energy for the oxidized samples. The variation of δ_{31} is weaker for the hydrogen terminated sample. The variation of δ_{15} is much weaker than that of δ_{31} for all the samples, although it appears to begin varying at the highest photon energies in the plot. Note that the magnitudes for both ∂_{15} and ∂_{31} show some degree of resonant behavior at approximately 3.38 eV for all three samples.

Change in phase with respect to driving frequency (here, the photon energy) is generally due to the presence of resonant behavior. For a simple driven oscillator, the oscillator is in phase with the driving term below resonance, lags it by 90° on resonance, and lags by 180° if the driving frequency is significantly higher than the resonance frequency. Since we are measuring the relative phase between surface and bulk terms, which also have resonances (see Chapter 3), care must be taken in interpreting the meaning of the phase; in particular, a 90° phase shift does not necessarily occur exactly on resonance. The observed phase inversion by photon energy has been predicted by the calculation of SH spectra using polarizable-bond model [34]. However, this phase inversion was not experimental reported before, probably due to an ambiguity in the origin of the azimuthal angle. We suggest that in the future experiments the initial direction against which one measure ϕ should remain fixed throughout the whole set of frequencies.

The fact that the relative phase between ∂_{31} and ζ is shifting with photon energy is evidence that one has a resonance that is not present in the other tensor element. Since ∂_{15} and the H-terminated sample show smaller or no phase shifts, although the bulk response should be identical, we conclude that the resonance is present in ∂_{31}. Based on the magnitude, all the tensor elements show a resonant peak around 3.38 eV. This peak has been attributed to the E_1 critical point in the bulk band structure, which also appears in the surface terms due to strain imposed by the oxide layer. Since the E_1 resonance is also present in the bulk response (see Chapter 3), we would expect ζ to display a similar resonance and thus no photon energy dependent phase shifts, as occurs in the H-terminated sample. Thus ∂_{31} must have a resonance that is not present in the bulk.

Spectroscopic measurements that only measured the amplitude of the SHG signal, and not its phase, showed the existence of resonances at higher photon energies [59]. Based only on the energetics of these resonances, it was concluded that they must be due to transitions that were unique to the interface as there are no equivalent bulk transitions. Since (*p, p*) polarization was used, the resonant behavior of the SH intensity was a combined effect of the interface (including ∂_{31}, ∂_{33}, and ∂_{15}) and bulk contributions. Our separation of individual tensor elements reveals the effect of excitation orientation. As shown in Fig. 4.3, the resonant energy of ∂_{31} discriminates different strains at the interface because the resonant energies of ∂_{31} increases from TO-Si to NO-Si then to H-Si. The amplitude of ∂_{15} is most sensitive to the difference between oxidized and hydrogen terminated surfaces. This indicates

that in-plane excitation probes the interfacial strain while out-of-plane excitation probes the interfacial bond. The presence of interface only transitions explains the shift in the relative phase between the surface and bulk contributions that we observe. Furthermore, our phase measurements prove that there are transitions that are only due to the interface and do not occur in the bulk, otherwise there would not be a phase shift.

For low photon energy, i.e., below the E_1 resonance, there is a consistent phase shift between the oxidized samples and the H-terminated sample. We attribute this to the difference in the electronic structure of the H-Si interface compared to that of the SiO_2-Si interface. Specifically, O is substantially more electronegative than H. Although the actual interface bonds are not resonant at these photon energies, it has been shown theoretically that simply changing the electronegativity of ad-atoms can dramatically change the spectrum of SHG [72]. Although this study did not address the phase of the SHG, it would be expected that it would also be affected. This is presumably due to modification of the band structure of the first few monolayers of the crystal, which is consistent with the fact that phase inversion can be induced by a dc electric field across the SiO_2-Si interface [69, 71].

4.6 Summary

We have shown that the RA-SHG signals provide information about the relative phase of the surface or interface tensor elements compared to the bulk elements. The phase of the azimuthal dependence of second harmonic generation from Si(001) interfaces is observed to undergo an inversion for appropriate

polarization configurations. The azimuthal dependence is due to interference between second harmonic generation from bulk anisotropic tensor elements and isotropic elements, which include both bulk and surface terms. The inversion can be induced by either varying the photon energy or by surface modification. In the former case, the inversion is ascribed to the presence of a resonance in the surface contribution and it enhances the ability to identify resonance positions. The photon energy dependence of the phase reveals resonances that are only present in the Si-SiO_2 interface and have no equivalent in the band structure of the bulk. The careful analysis presented here shows that significantly more information can be extracted from RA-SHG scans, particularly with regard to separating the bulk and surface contributions, than has been done heretofore.

Chapter 5

Surface SHG from Cr-SiO_2-Si(001) structures

5.1 Introduction

Silicon is the dominant semiconductor material for electronic circuits and devices. Ongoing miniaturization of electronic systems drives critical regions of integrated circuits ever closer to silicon interfaces. SiO_2-Si interfaces are of particular importance due to their almost ubiquitous presence in metal-oxide-semiconductor (MOS) structures and MOS field-effect transistors. The thickness of the gate insulator (commonly SiO_2) for MOS transistors is being scaled down. However, there exists a scaling limit because tunneling current through the gate oxide increases drastically with reduced thickness. In addition, dopants may penetrate from the heavily doped polysilicon gate into the substrate, which causes instability in the threshold voltage. Performance and reliability of MOS structures depends more and more on the microscopic quality of dielectrics and their interfaces. Traditionally, the properties of SiO_2-Si interfaces were investigated by means of electrical characterization, such as capacitance voltage (C-V), current voltage (I-V) and constant voltage stress (I-t) measurements [73, 74]. The nonlinear optical method of second-harmonic generation (SHG) has been developed into a sensitive surface or interface probe [19, 20, 54]. Among the many advantages of this technique, the features of non-contact sampling and accessibility to buried interfaces are most attractive to the microelectronics industry. It has been shown that surface SHG is sensitive to a number of properties of

the SiO_2-Si interface, such as crystalline orientation [24], interfacial structure [33, 75], preparation and roughness [57, 58], and charge transfer [66, 76].

The Cr-SiO_2-Si(001) structures have been used to study the SHG dependence on the bias dc field across the SiO_2-Si interface [37, 69-71], but the sources of SHG in reflection from such complicated MOS structures were not systematically investigated. It was found that the SHG signals produced in reflection from silicon or silver surface showed a significant variation with a dc bias electric field applied normal to the surface [77]. The dc field was applied by immersing the sample in an electrolyte solution with a bias voltage between it and an electrode. SHG at the SiO_2-Si interface was also found to be very sensitive to a dc field across the interface. The enhancement of SHG is caused by the electric-field-induced SHG (EFISH) effect. In the original experiment on the EFISH effect at the SiO_2-Si interface [36], the dc field was applied between the Si substrate and a ring shaped metal electrode on top of the SiO_2 layer, and SHG was measured in transmission geometry through the metal ring; therefore, the propagation of light was not affected by the electrode. Several further EFISH experiments were performed on Cr-SiO_2-Si structures using a reflection geometry [37, 69-71]. In these studies, the dc biases were applied between the Si substrate and an ultrathin semitransparent Cr film, which fully covered the SiO_2 layer, so the incident light was transmitted through the Cr coating film to reach the SiO_2-Si interface. The measured SHG signals and the bias dependent SHG spectroscopy were treated as if they came from the SiO_2-Si interface alone with no contribution from the Cr coating. With the experimental evidence for high sensitivity of SHG to surface conditions, it is reasonable to question the pre-condition that the SHG signal in

reflection from such a Cr-SiO_2-Si(001) structure has negligible contribution from the Cr coating film. Several regions of the MOS structure, such as the outer surface of the Cr film, the Cr-SiO_2 interface, or even the SiO_2 or Cr bulk, could be possible SHG sources. The experimental evidence of strong enhancement of SHG at metal surfaces by a dc bias [77] also suggests that the SHG bias dependence could come from the Cr-SiO_2 interface as well.

In this chapter, we present a comprehensive study of the effect of ultrathin Cr coating film on the SHG response in reflection from the Cr-SiO_2-Si(001) MOS structures. In addition, we study the influence of the thickness of the SiO_2 layer on the SHG response. The aims of this work are to identify the sources of SHG from MOS structures and to explore the potential for using the surface SHG to characterize the electronic dynamics in MOS structures. We compare SHG signals from Cr coated and uncoated SiO_2-Si surfaces and compare SHG signals from thin oxide and thick oxide covered Si surfaces in several respects, including rotational-anisotropy SHG (RA-SHG), SHG spectroscopy, and time-dependent SHG (TD-SHG). We find that the RA-SHG peak locations (azimuthal angles) of the RA-SHG signals from Cr coated and uncoated SiO_2-Si surfaces differ at higher photon energies but are the same at lower photon energies for several polarizations. The modulation of peaks and valleys in RA-SHG signals arises from interference between isotropic and anisotropic SHG contributions (see Chapters 3 and 4), whereas the anisotropic contribution is generated only from the bulk and is independent of surface preparation. Therefore, RA-SHG signals carry phase information about the surface SHG relative to the bulk anisotropic SHG. The altered peak location of the RA-SHG signals indicates that the

Cr layer on oxidized Si(001) surfaces produces an additional SHG contribution compared to uncoated surfaces. The strength of SHG contribution originated from the Cr coating varies with photon energy. The observed SHG signal from the Cr coated natively oxidized Si surface is weaker than the Cr coated thermally oxidized Si surface; but this relation is reversed for samples before the Cr coating. The observed TD-SHG signals decrease with time for Cr coated SiO_2-Si surfaces while increase for uncoated surfaces. To further identify the additional sources of SHG, we investigate SHG from the surface of a very thick Cr film and from the SiO_2-Cr interface with and without a dc bias. We show that SHG contributions from all these surfaces (or interfaces) are non-negligible at certain photon energies. We attribute the difference in the SHG spectrum from Cr coated and uncoated samples to interference between additional and original SHG contributions.

5.2 Theoretical background

From the phenomenological theory in Chapter 2, both bulk and surface contribute to the SHG. We take advantage of this natural co-existence of bulk and surface SHG and show that we can actually obtain reliable phase information for surface SHG, which can be easily utilized to distinguish different surface conditions. This is realized by combining polarization selection and RA-SHG. The fact that the bulk anisotropic SHG can be independently detected from the Si(001) face makes it a good choice for studying surface SHG.

From Chapter 2, the *h*-polarized SHG fields $E_{g,h}^{(2\omega)}$ are related to the *g*-polarized incident fundamental fields E_g by,

$$E_{g,s}^{(2\omega)} = a_{4,(g,s)} \sin(4\phi) e^{i\delta_{g,s}} E_g^2, \tag{5.1}$$

$$E_{g,p}^{(2\omega)} = [a_{0,(g,p)} + a_{4,(g,p)} \cos(4\phi)] e^{i\delta_{g,p}} E_g^2, \tag{5.2}$$

where ϕ is the azimuthal angle measured between the plane of incidence and the [100] axis in the surface. The coefficients a_n 's are functions of related susceptibility tensors elements and linear optical factors (see Chapter 2). Here, the polarization (*g* or *h*) of both fields is limited to be *s* or *p*.

On the other hand, for a special polarization (*q, s*), for which the bulk and surface SHG can be exactly separated in theory, this relation takes the form,

$$E_{q,s}^{(2\omega)} = [a_{0,(q,s)} + a_{4,(q,s)}^{s} \sin(4\phi) + a_{4,(q,s)} \cos(4\phi)] e^{i\delta_{q,s}} E_q^2. \tag{5.3}$$

The SHG intensity is proportional to the magnitude squared of the SHG field. If the anisotropic coefficient, a_4, is chosen to be positive and real (with its phase included in $\delta_{g,h}$), then the isotropic term, a_0, is complex in general. As shown in Chapter 2, if the γ SHG contribution is neglected, all other tensor elements can be determined from polarization selected RA-SHG signals, specifically, ζ from (*s, s*) or (*p, s*), ∂_{15} from (*q, s*), ∂_{31} from (*s, p*), and ∂_{33} from (*p, p*). Thus, the SHG response from the Si(001) surface is fully characterized by this set of measurements.

If there is a dc electric field along the surface normal, SHG has an additional source from the EFISH effect, as shown in Chapter 2. The surface EFISH effect can be effectively combined into the field-independent surface SHG effect by defining a new set of elements, ∂_{31}^{d}, ∂_{33}^{d}, and ∂_{15}^{d}, and then adding them to the original field-independent elements one by one, written as $\partial_{31} + \partial_{31}^{d}$, $\partial_{33} + \partial_{33}^{d}$, and $\partial_{15} + \partial_{15}^{d}$.

Therefore, the surface EFISH effect is isotropic for the (Si(001) surface. The bulk EFISH polarization is treated by introducing additional tensor elements, ζ^d, η^d, and γ^d. SHG from the bulk EFISH effect is still isotropic for the Si(001) surface. However, it is not appropriate to combine it into either bulk or surface field-independent effect, because ζ^d and η^d have no equivalents in field-independent elements. Moreover, the presence of the EFISH effect greatly complicates the separation of different SHG contributions.

5.3 Experimental conditions and sample preparation

The experimental setup is described in Chapter 1. Four samples were prepared from the same undoped silicon wafer ($\rho > 20\Omega$ cm), <100> oriented. The natively oxidized Si (NO-Si) and the thermally oxidized Si (TO-Si) samples are the same as in Chapter 3. Two MOS structures were prepared by depositing Cr on oxidized Si substrates to form Cr coated NO-Si (Cr-NO-Si) and Cr coated TO-Si (Cr-TO-Si), with both Cr coatings 1.5 nm thick. The Cr coating was performed in an Edwards Auto 306 vacuum chamber (~1×10^{-6} Torr) using thermal evaporation. The substrate temperature was kept at 20~45 ^{o}C during deposition.

5.4 Experimental results

5.4.1 Comparison of RA-SHG from Cr-SiO_2-Si and SiO_2-Si surfaces

At a two-photon energy of 3.40 eV (fundamental wavelength 730 nm), the RA-SHG signals from the Cr-NO-Si and Cr-TO-Si samples are shown in Fig. 5.1, and those from the NO-Si and TO-Si samples are shown in Fig. 5.2, for (*p, p*), (*s, p*), and

(*q, s*) polarization configurations. All these patterns show a fourfold symmetry, but the RA-SHG signals from Cr coated and uncoated samples consistently differ in peak locations for all these polarizations. The (*p, p*) RA-SHG signal shows a valley at $\phi=45^{o}$ for Cr coated samples while a peak for uncoated samples. The SHG signal from the NO-Si is stronger than that from the TO-Si, while this relation reverses after the Cr coating. Clearly, the Cr coating produces a large change in the RA-SHG response compared to that before coating. The question arises here whether the Cr coating process affects the structure at the SiO_2-Si interface. Based on the deposition condition of thermal evaporation at room temperature, such a possibility is not likely. An additional way to check this is to vary the thickness of the SiO_2 layer on Si(001) surfaces and measure the RA-SHG signal from each sample. A series of oxidized Si(001) surfaces with oxide thickness up to 40 nm were prepared and it was found that the peak locations of the (*p, p*) RA-SHG signals are all consistent with the observed trends, which further demonstrate that the Cr coating does not affect the structure at the SiO_2-Si interface.

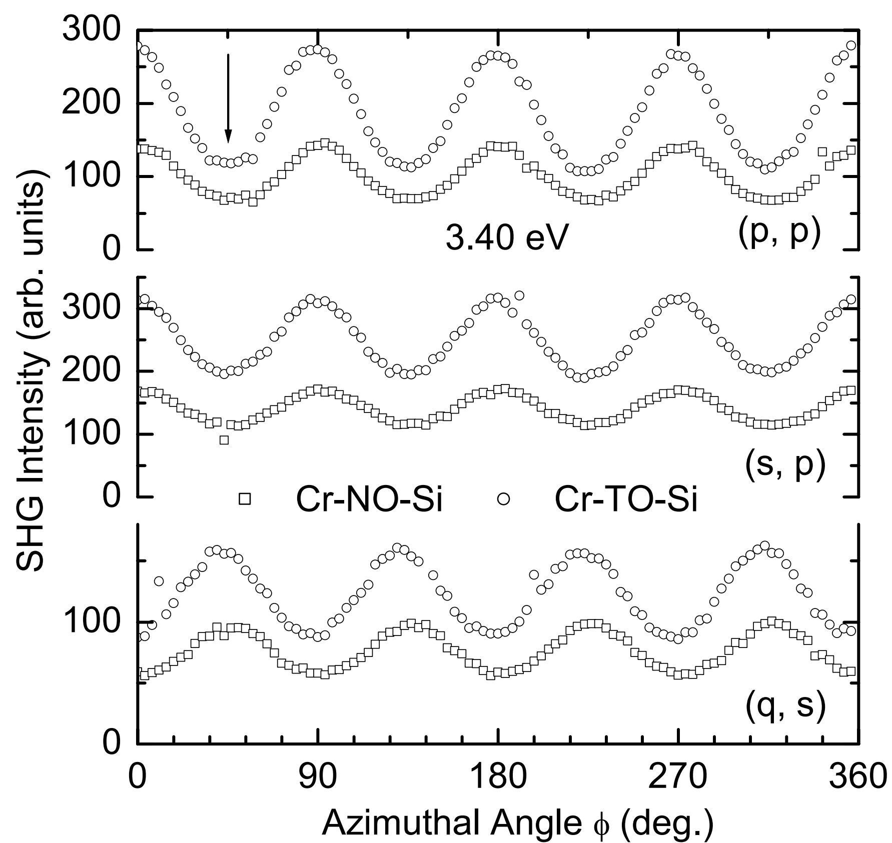

Fig. 5.1. RA-SHG signals from Cr-NO-Si and Cr-TO-Si samples for the (*p, p*), (*s, p*), and (*q, s*) polarizations at a two-photon energy of 3.40 eV.

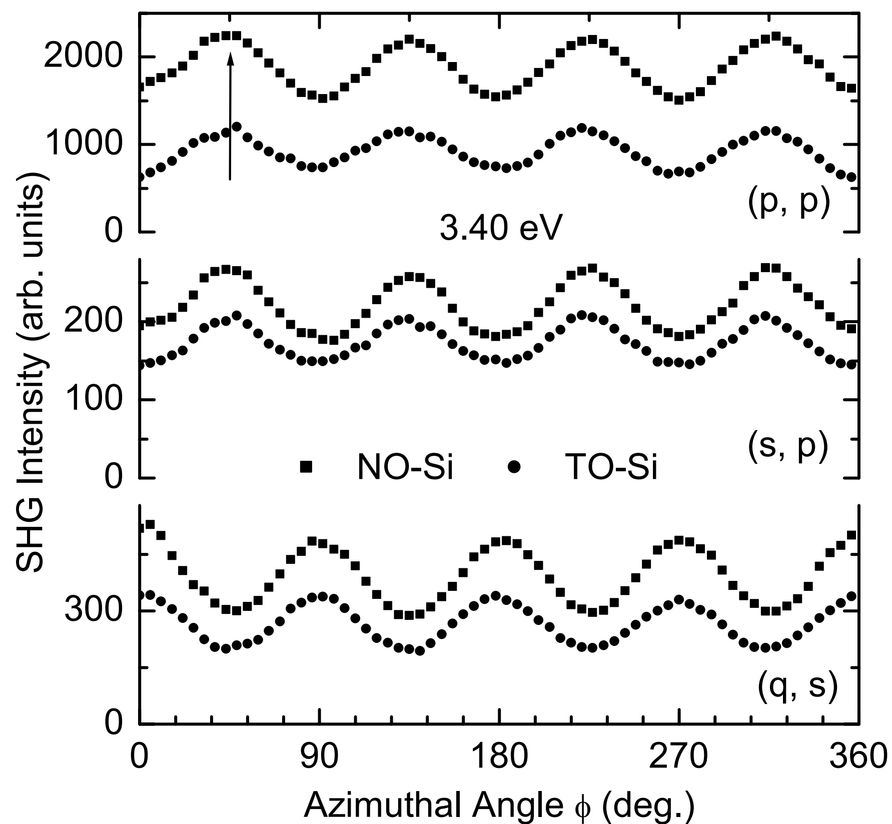

Fig. 5.2. RA-SHG signals from both NO-Si and TO-Si samples for the (*p, p*), (*s, p*), and (*q, s*) polarizations at a two-photon energy of 3.40 eV. Note that the peak locations are different from that of Cr coated samples consistently for all these polarizations.

Besides the difference in the peak locations of RA-SHG, the SHG intensities are also very different, especially in the case of (*p, p*) polarization. However, we should keep in mind that the thin Cr layer changes the linear optical properties at the outside surface of the oxide, which is verified by the comparison of the (*p, s*) RA-SHG signals from the TO-Si and Cr-TO-Si samples, as shown in Fig. 5.3. The (*p, s*) RA-SHG signals from the NO-Si is also weaker than that from the Cr-NO-Si (data not shown). Based on the phenomenological theory in Chapter 2, bulk SHG is the only contribution to observed SHG signals. The bulk Si is untouched by surface coating. The weaker SHG signal from Cr coated samples is easily understood to be caused by decreased transmission of both the fundamental and the SHG light through the coating layer, which also suggests that comparison of SHG intensities before and after the Cr coating should take into account of linear optics effects.

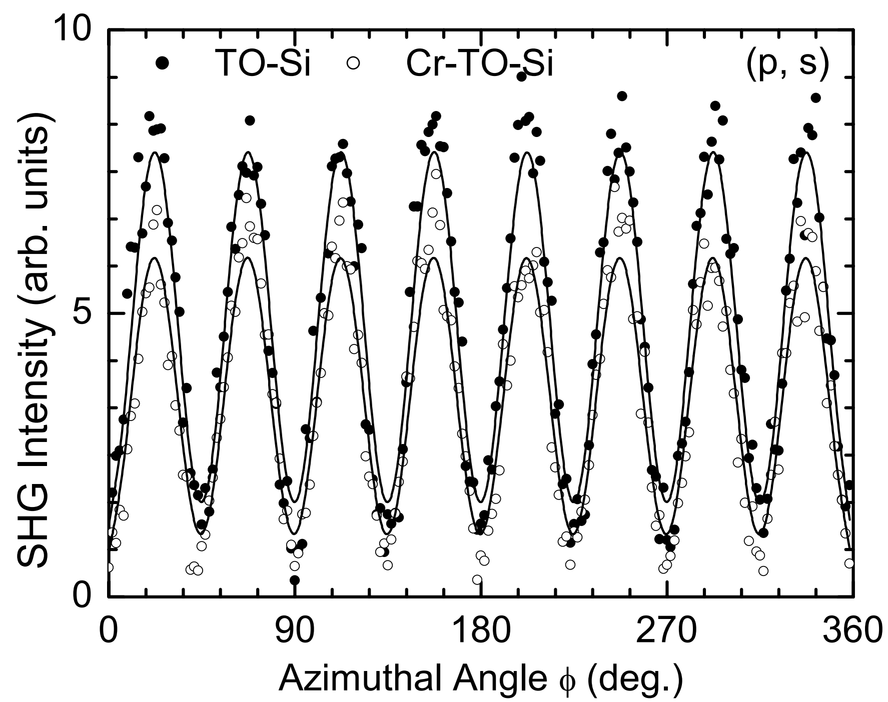

Fig. 5.3. Comparison of the (*p, s*) polarized RA-SHG signals from TO-Si and Cr-TO-Si samples at a two-photon energy of 3.40 eV. The solid lines show the fits.

5.4.2 Spectroscopic study of RA-SHG from Cr-SiO_2-Si

The relationship of the peak positions in the RA-SHG signals for Cr coated and uncoated samples does not stay the same with variation of the photon energy. The (*p, p*) RA-SHG signals from the Cr-TO-Si samples at several two-photon energies are shown in Fig. 5.4. At the azimuthal angle ϕ=45°, RA-SHG signals show a valley at higher photon energies but a peak at lower photon energies. The RA-SHG signal has eightfold symmetry at the two-photon energy 3.28 eV (fundamental wavelength 755 nm), which is significant because absolute SHG intensity is not needed to see the eight peaks. A similar trend is observed for the Cr-NO-Si sample, but the photon energy where the eightfold symmetry appears slightly shifts to blue (data not shown). We showed in Chapter 3 that the peak locations of the (*p, p*) RA-SHG signals from both the NO-Si and TO-Si samples does not change in the two-photon energy range of 3.06-3.54. This inconsistency in peak locations clearly indicates that the Cr layer affects the spectroscopic behavior of SHG compared to before coating.

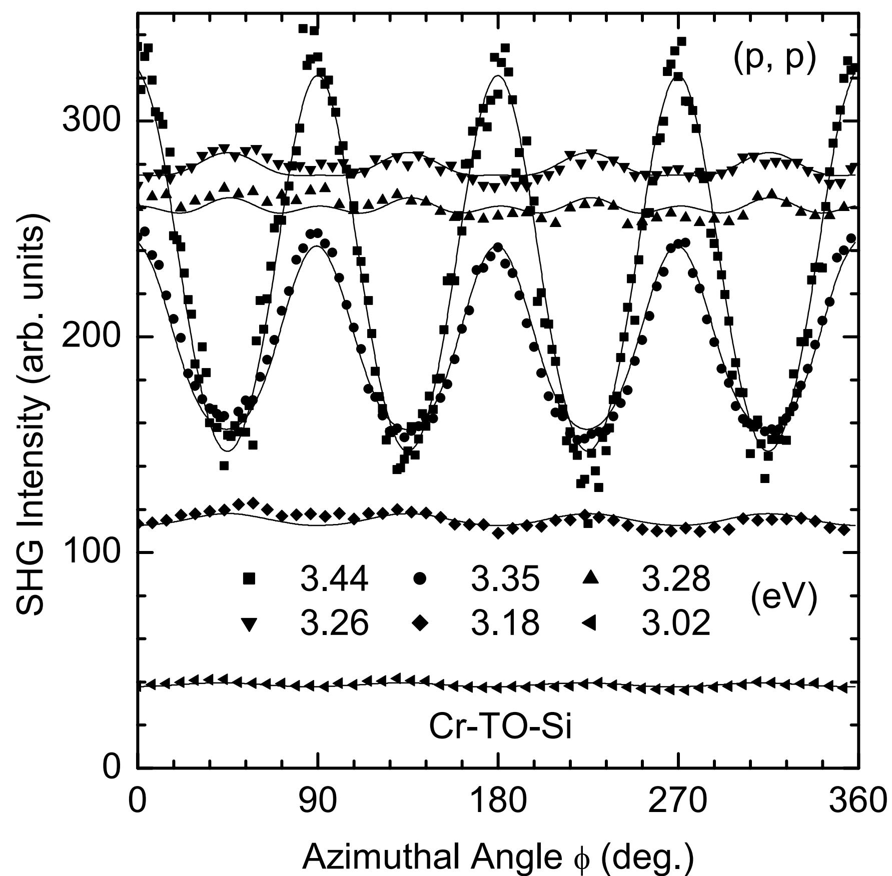

Fig. 5.4. (*p, p*) polarized RA-SHG intensities from the Cr-TO-Si sample at several two-photon energies. Note that the RA-SHG with eightfold symmetry appears at the two-photon energy of 3.35 eV. Note that these curves are different from the RA-SHG signal from the TO-Si sample for corresponding photon energy.

5.4.3 Comparison of the TD-SHG responses

The Cr coating significantly changes the time-dependent SHG (TD-SHG). Figure 5.5 shows the comparison of the (*p, p*) TD-SHG signals from all four samples at a two-photon energy of 3.40 eV. To observe the TD-SHG, we moved the sample so that a fresh spot, i.e., one that the laser beam has been kept away for a long period of time, was used for each measurement. Using the shutter, we started to illuminate the sample at time zero and then began recording the signal over a series of 0.5 sec counting intervals. After 80 sec, when the signal was close to its asymptotic value, the shutter was closed. To observe the variation of the SHG signal with time when the laser beam is blocked, we repeated the following procedure. After 30 sec, the shutter was opened for a 0.5 sec gate and the SHG signal was recorded and then shutter was closed again. At the initial charging stage, the TD-SHG signals increase with time for samples without coating while they decrease with time for Cr coated samples. During the measurement, the sample azimuthal angle was fixed at a peak RA-SHG signal for each sample. We note that these trends of increase and decrease in the TD-SHG signals are the same at all other azimuthal angles. The measured time-dependent effect for the (*p, s*) TD-SHG is negligible for all of the samples.

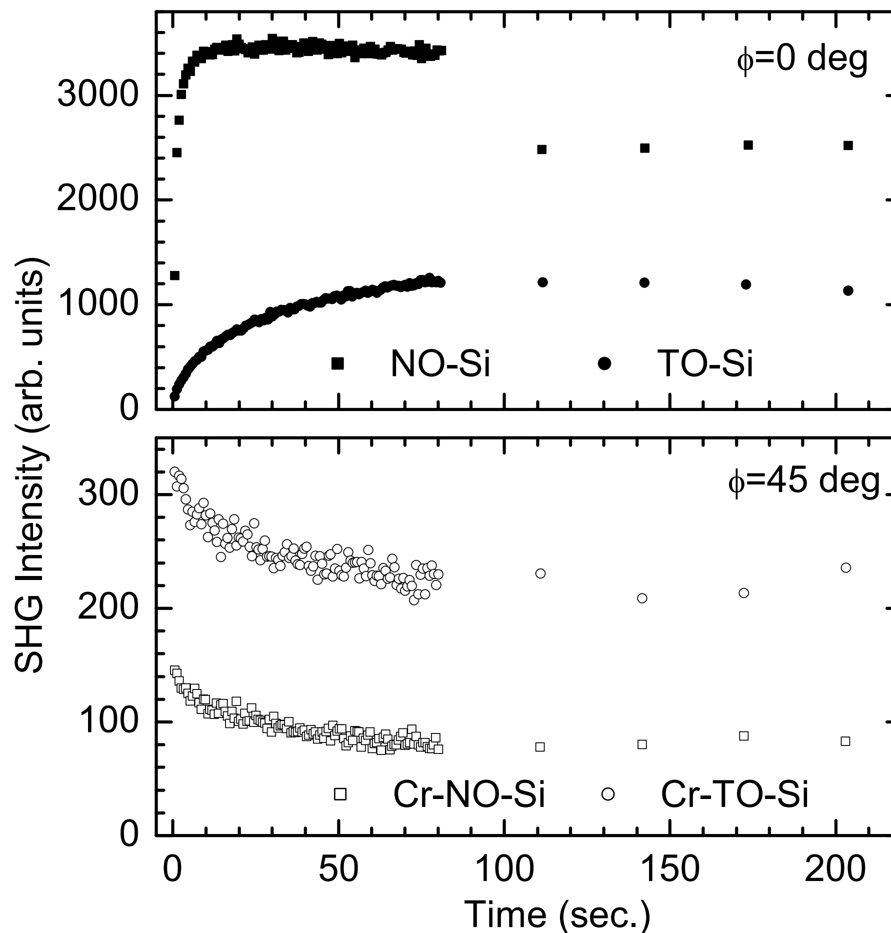

Fig. 5.5. Comparison of the TD-SHG signals for the (*p, p*) polarization at a two-photon energy of 3.40 eV for different samples: NO-Si and TO-Si (upper panel); Cr-NO-Si and Cr-TO-Si (lower panel). Note that the sample azimuthal angle is chosen to be where the RA-SHG signal shows a peak, i.e., ϕ=0 deg for uncoated samples and ϕ=45 deg for Cr coated samples.

5.5 Discussion and further experimental results

5.5.1 Phase inversion due to additional SHG sources

The observed azimuthal dependence of the SHG intensity follows directly from the phenomenological prediction based on symmetry consideration. As shown in Eqs. (5.1), (5.2), and (5.3), the peaks and valleys in the RA-SHG signal comes from interference between isotropic and anisotropic SHG contributions. The latter originates from only the bulk and is independent of surface preparation; therefore, it serves as a reference for both the phase and the amplitude of surface SHG, as we showed in Chapters 3 and 4. We split the isotropic coefficient, a_0, in Eqs. (5.2) and (5.3) into a real part and an imaginary part, written as $a_0 = a_{0,r} + ia_{0,i}$, and designate them as interfering and non-interfering isotropic SHG contributions, respectively. They are so named because only the real part interferes with the bulk anisotropic SHG contribution, while the imaginary part functions as an azimuthal independent increase in the SHG signal. For the (*p, p*) polarization, the isotropic SHG is usually much stronger than the anisotropic SHG, thus the RA-SHG scan usually shows fourfold symmetry. If $a_{0,r}$ and a_4 are the same sign, a valley appears at ϕ=45° in RA-SHG, and if $a_{0,r}$ and a_4 are opposite in sign, a peak appears at ϕ=45°. If $a_{0,r}$=0, the RA-SHG is eightfold symmetric, as shown in one the RA-SHG scans in Fig. 5.4. Compared with the eightfold symmetry in the (*p, s*) RA-SHG, the dc level of the RA-SHG signal on which the modulation rides is much higher for the (*p, p*) polarization than that for the (*p, s*) polarization, which is about zero for the latter. It should be

noted that the measured peak locations of the (*p, p*) RA-SHG signal from Cr coated samples at the two-photon energy 3.40 eV is consistent with previous SHG results on a similar MOS structure at zero dc bias [69] but inconsistent with our results on uncoated samples in Chapter 3.

5.5.2 Further experiments to determine the sources of SHG

In order to investigate the reason for such an apparent difference of the SHG responses from the surfaces of Cr coated and uncoated samples, we prepared a series of new samples to detect possible SHG sources from silica, Cr, and Cr-Silica interfaces. Figure 5.6 shows the results of the SHG signals from different samples at several two photon energies. Based on previous results of SHG on metal surfaces [77, 78], it is reasonable to predict that the Cr layer might introduce an additional SHG contribution. The first sample, designated as Silica, was a 1mm thick fused silica slab without Cr coating. The measured SHG signal in reflection from it is very weak (not shown in Fig. 5.6). The second sample, designated as Cr-Silica, was prepared by coating a 1.5 nm thick Cr film on top of the fused silica sample, using the same coating condition as that for the Cr coated Si samples. The measured SHG signal from the Cr-Silica surface is about two orders of magnitude stronger than that from the Silica surface. This is a clear evidence that the Cr coating has an effect on the total reflected SHG signal; however, we should expect that the additional SHG signal originated from the Cr coating on the Cr-TO-Si is even stronger than the measured SHG signal from the Cr-Silica sample, because Si substrate reflects much more SHG light than silica does, due to different indices of refraction between Si and silica. The third sample, designated as Cr, was prepared by depositing a 125 nm thick Cr film on

a 0.16 mm thick fused silica substrate. The measured SHG signal in reflection from the upper surface of the Cr film is very strong, as shown in Fig. 5.6. Because the thick Cr layer is opaque, light can not penetrate to the Cr-Silica interface, thus no SHG signal is generated from it. This signal is strong, but we should consider that the SHG response from a 1.5 nm thick Cr film is different from that from a very thick Cr film. The trend of increasing SHG signal with increasing coating thickness is expected to be similar to previously measurements on silver films [78]. To study the SHG response from the Cr-Silica interface, we just turned over the Cr sample (125 nm thick Cr coated on a 0.16 mm thick silica substrate) and measured the SHG signal in reflection from the upper surface of silica, which we designate as Silica-Cr. As shown in Fig. 5.6, this signal is about one order of magnitude weaker than that from the Cr sample; however, we expect to see similar SHG signals from Silica-Cr and Cr surfaces. Differences in interfacial morphology and electron mobility between these two interfaces are possibly responsible for the discrepancy. Combining these facts, we conclude that the Cr coating adds an SHG contribution to original SHG from samples without the Cr coating and the outermost surface of Cr film is likely the main source of additional SHG. The change of peak locations in RA-SHG signals at the two-photon energy 3.40 eV is caused by interference effect from additional SHG sources.

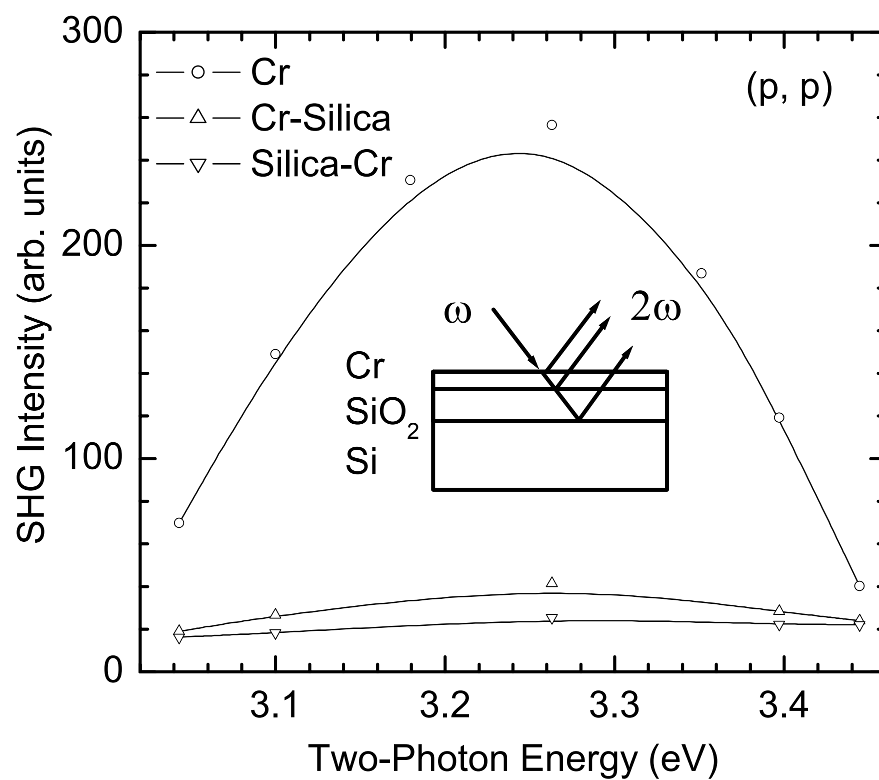

Fig. 5.6. Isotropic SHG signals from the surfaces of a thick Cr film, a thin Cr coated silica sample, and a silica covered Cr sample at different two-photon energies. The inset shows that the measured SHG signal is an interfering combination of different sources.

With the additional sources of SHG from Cr coated samples compared to uncoated samples, an additional concern for the SHG response from MOS structures is whether the bias dependence of SHG originates from the additional SHG sources or original ones. If an external bias voltage is applied between the Cr film and an electrode underneath the Si substrate of the MOS structure, an electric field is applied both across the Cr-SiO_2 interface and the SiO_2-Si interface. To study the bias dependence of the SHG at the Cr-SiO_2 interface, we attached a copper foil on top of a silica slab that has a 125 nm thick Cr film on the backside. A capacitor was formed between the copper foil and the Cr film. A small hole was left in the middle of the copper foil so that both the incident and SHG light were able to travel through it without being affected by the copper foil. The SHG signal was measured in reflection from the silica side through the hole. Up to 40 volts of dc voltage between the Cr film and the copper foil was applied, but a change in the SHG signal with and without the dc bias was not observable, even when the thickness of the SiO_2 was decreased from 1 mm to 0.16 mm. Further experiments is needed to investigate the SHG response under a stronger dc field across the Cr-SiO_2 interface, but the field used here is comparable to previous used values, at which the bias dependence of the SHG signal was observable [71]. Therefore, these previous results [37, 69-71] of SHG on MOS structures characterized the bias dependence of the SHG signal at the SiO_2-Si interface, but SHG signals originated from other unwanted sources were involved in the measured RA-SHG.

By spectroscopic comparison of RA-SHG signals from Cr coated and uncoated samples, we obtain the relative strength of the SHG contribution arising

from the Cr coating. As shown in Fig. 5.4, the SHG signal at ϕ=22.5° is only due to the isotropic SHG signal, which peaks at the two-photon energy 3.26 eV nm for the Cr-TO-Si sample. This energy is a significant shift from our earlier result of 3.35 eV for the TO-Si sample in Chapter 3. The SHG signal from the Cr sample also varies with photon energy, as shown in Fig. 5.6. Exact separation of different SHG sources is difficult due to interference among different SHG fields, and the involvement of additional sources of SHG complicates the interpretation of spectroscopic results. At higher photon energy, the effect of the Cr coating on the RA-SHG signal is very strong; while at lower photon energy, it appears to be negligible. Figure 5.4 also shows that the SHG spectrum from Si(001) surfaces strongly depends on the azimuthal angle at which the SHG signal is taken.

5.5.3 Insight into the Charge Trapping Process

The observed trends in the TD-SHG signals can be explained in terms of the self-induced EFISH effect. The dc electric field across the SiO_2-Si interface is not an external field but an effective field, which arises from charge transfer by photon injection and subsequent trapping in the charge traps at the SiO_2-Si interface and inside of the bulk oxide [66, 76]. Comparing the RA-SHG signals in Figs. 5.1 and 5.2, we find that the peak locations for Cr coated samples fall into the valley locations for uncoated samples consistently for all of the (*p, p*), (*s, p*), and (*q, s*) polarizations, which suggests that each field-independent element in ∂_{31}, ∂_{33}, and ∂_{15} is roughly out of phase for Cr coated and uncoated samples. We should note that the RA-SHG signals were taken with a counting gate time of 1 sec and after the samples were fully

discharged. The direction of the effective dc field is the same for both the Cr coated and uncoated samples, because electrons transfer out of the Si substrate in one direction. Therefore, the self-induced EFISH effect enhances the TD-SHG signal for uncoated samples while it diminishes the TD-SHG for Cr coated samples. This explains the increasing SHG signals with time from the NO-Si and TO-Si surfaces while decreasing SHG signals from the Cr-NO-Si and Cr-TO-Si surfaces, as shown in Fig. 5.5. The saturated TD-SHG signal is much stronger for NO-Si than for TO-Si, but it is stronger for Cr-TO-Si than for Cr-NO-Si. These results can be understood in terms of the fact that the number of charge traps at the interface between silicon and native oxide is much denser than that after the high temperature thermal oxidation, consistent with other results [79]. The much shorter rise time of the TD-SHG signal for NO-Si compared with TO-Si is due to higher mobility of the hot electrons for NO-Si. No noticeable variation of the (*p, s*) TD-SHG signal with time indicates that the charge sources come from a very shallow region underneath the interface, compared with the estimated ~30 nm escape depth of the SHG light in silicon. In the circumstance of the self-induced EFISH effect, the bulk EFISH source predicted in Chapter 2 is negligible. However, if there is an external dc electric field across a MOS structure, the EFISH effect possibly includes both surface and bulk sources. If the dc field flips its sign, the EFISH field inverts its phase; therefore, peaks of the RA-SHG signal can turn into valleys by applying a dc bias. This explains previous results of bias-dependent RA-SHG signals from Si(001) MOS structures [69, 71].

Comparison of the time-dependent SHG responses between thin and thick oxidized and between Cr coated and uncoated samples allows insight into the carrier

dynamics at interfaces. Previous results suggested that electrons can be injected from the Si substrate to the ambient-SiO_2 interface by a multi-photon process [80-82] and trapping of electrons can be enhanced by using oxygen ambient [66, 83]. An assumption used in these studies is that the electron band structure of the SiO_2 overlayer remains unchanged with decreasing oxide thickness. When the thickness of the SiO_2 insulator is reduced below 3-4 nm, high tunneling currents could be significant in MOS structures. This indicates that using only the band structure of thick SiO_2 to explain the charging dynamics is not applicable to ultrathin SiO_2 films. Another assumption is that the SHG contribution at the ambient-SiO_2 interface is negligible, which is based on the fact that the SHG signal from a thick silica substrate held in air is negligible compared with that from the Si surface, as shown by earlier results [84] and by our results in this chapter. However, if the SiO_2 overlayer is very thin and if there are trapped electrons inside the oxide and at the ambient-SiO_2 interface, considerable SHG signals could be generated from both sources. Previous observed dramatic decrease of the SHG intensity from a metal surface with increasing pressure of ambient oxygen is a clear evidence of ambient influence on SHG [85]. We used N_2 ambient but observed strong TD-SHG signals. This indicates that the charge traps are not likely located at the ambient-SiO_2 interface because N_2 is very inert and its potential for charge trapping is small. If the ambient is changed from N_2 to O_2, we found little change in the TD-SHG signal for the TO-Si but dramatic change for the NO-Si. If electrons can tunnel across the thin SiO_2 overlayer by one photon injection, or if the charge traps are located at the SiO_2-Si interface, then a multiple photon process is not likely to happen. For ultrathin oxide covered Si

samples, further experiments are needed to identify whether the enhancement of the SHG signal by oxygen ambient is caused by more charge traps compared to that of the N_2 ambient or caused by an additional SHG source at the O_2-SiO_2 interface. We also found that the TD-SHG signals from both the Cr-NO-Si and Cr-TO-Si samples show similar noticeable change if the ambient is changed from N_2 to O_2, which can be understood to be due to the same ambient-Cr interface. These results probably suggest that if there are free electrons at the ambient-medium interface, the effect of oxygen ambient on SHG is strong, otherwise it is negligible.

5.6 Summary

The combination of polarization selection and RA-SHG has been applied to study the effect of the ultrathin (1.5 nm) Cr coating film on SHG from Cr-SiO_2-Si(001) structures with either native oxide or thermal oxide gate insulators. By comparing RA-SHG signals from Cr coated and uncoated SiO_2-Si(001) surfaces, we find that the peak locations of the signal as a function of sample azimuthal angle are different at a certain photon energy consistently for several polarizations. This enabled a detailed spectroscopic comparison of the RA-SHG signals from the Cr coated and uncoated samples, which reveals that the peak locations are different for higher photon energies while the same for lower photon energies. In addition, we have shown that the TD-SHG signals decrease for Cr-coated samples and while increase for uncoated samples. These results indicate that the Cr coating has a significant effect on the SHG from Cr-SiO_2-Si(001) structures. Through further investigation, we have identified that the Cr coating introduces additional sources of SHG, of which the most important contribution is from the outermost surface of the

Cr film. The SHG intensity strongly depends on the thickness of the overlayer oxide. For the same thinner overlay oxides, we have observed stronger SHG signal for uncoated samples but weaker SHG signal for Cr coated samples. All these results have been well explained by using a phenomenological theory that takes into account of crystal symmetry and self-induced EFISH effect. In several previous studies [37, 69-71], the Cr-SiO_2-Si(001) MOS structures were used to study the properties of the SiO_2-Si interface and the SHG arising from the Cr coating was neglected. However, we showed here that the Cr coating significantly changes both the spectroscopic and the time-dependent behaviors of SHG by interfering with additional SHG sources introduced by the ultrathin Cr coating.

Chapter 6

SHG from thermally oxidized Si(001) surfaces

6.1 Introduction

Silicon plays an essential role in today's semiconductor industry. It is the inexpensive silicon CMOS technology that initiated and maintains the information revolution. However, the particular role played by silicon is not solely due to its superior properties as a semiconductor. The superior properties of silicon dioxide (SiO_2) and the quality of SiO_2-Si interface greatly contribute to this role as well. The SiO_2 layer is a natural electrical insulator and a natural chemical protector, which is not only easy to produce but also stable and chemically very inert. The quality of the SiO_2-Si interface depends strongly on processing conditions. The characteristics of the interface are critical in determining integrated circuit performance. However, the interface is buried below the oxide and thus not accessible to direct microscopic measurement. Based on the symmetry breaking at the interface, the nonlinear optical technique of surface SHG has been developed as a sensitive and versatile probe for buried interfaces. A number of experiments on SHG at the SiO_2-Si interface have been performed showing the influence of interfacial stain [86, 87], charge and electric field [66, 76], preparation and interface roughness [57, 58], steps on vicinal surfaces [52, 88, 89], the possible presence of a crystalline oxide interface layer [55], and the oxide thickness [90-92]. These various observation and interpretations suggest that SHG at the SiO_2-Si interface is a complex process of nonlinear polarization that is influence by multiple factors.

The observed SHG dependence on a particular interfacial property may not be attributed to that property alone but to incidental or alternative effects. For example, the sensitivity of SHG to interface roughness [57, 58] is possibly explained in terms of charge traps and electric-field-induced SHG. This happens because the SHG measurement is an indirect method for interface roughness. In order to use the SHG technique, one has to relate the measured SHG signal to the roughness being detected. It is convenient that interface roughness at the SiO_2-Si interface can be measured by x-ray scattering [93]. By combining SHG and x-ray scattering measurements, it has been shown that there is a monotonic correlation between SHG signal and interface roughness [57]. The observed trend is that the ratio of the isotropic to anisotropic SH coefficients increases as interface roughness decreases, which is consistent with earlier SHG measurements, where roughness was characterized by atomic force microscopy (AFM) [58]. However, this trend is opposite to our recent results of SHG on a series of thermally oxidized Si(001) samples. The samples are the same samples as before [57], but the laser used here is at shorter wavelengths. As has been shown, the SiO_2-Si interface becomes smoother with increasing oxidation time due to kinetic smoothing of the buried interface [93]. At first glance, interface roughness is well related to the SHG signal by performing SHG studies on the set of thermally oxidized samples. However, it is still not persuasive to say that interface roughness is the main factor of influence to SHG, because side effects, such as changes in charge traps and thermal oxides could cause variation of SHG as well.

In order to use SHG as a probe of the buried SiO_2-Si interface, it is important to understand how the oxide layer influences the total SH signal. Since the oxide

layer has a refractive index between air and Si, and is transparent throughout a large part of the spectrum, multiple reflection for both the fundamental and the SH beams should play a role. As has been shown, the observed periodic variation with oxide thickness of the (*p*, *s*) polarized SH signal from Si(111) surfaces [91] is explained by multiple reflection in the oxide film. It is important to note that in order to study only the multiple reflection effect, the structure of the SiO_2-Si(111) interface should be unchanged by varying oxide thickness because the (*p, s*) SHG from a Si(111) surface has both bulk and surface contributions [27]. Such a condition could be realized by etching the very thick oxide covering the Si sample down to the thickness needed.

In this chapter, we present a systematic study of the effect of thermal oxidation of the Si(001) surface on the SH response from the SiO_2-Si interface. The thermal oxidation time is controlled, so that the transition width from Si to SiO_2 (interface width) and the thickness of the thermal oxide are systematically controlled at the same time. Therefore, both the multiple reflection and interface modification effects may contribute to the dependence of SHG on thermal oxidation. To separate out only the multiple reflection effect, we use a combination of polarization selection and rotational-anisotropy SHG (RA-SHG). The (*p, s*) polarized RA-SHG from the Si(001) surface is generated only from the bulk, and interface modification is an irrelevant factor, thus multiple reflection is readily known from oxide thickness dependence of SHG. We use the (*p, p*) RA-SHG signal to study the influence of interface conditions on SHG and find that larger interface width corresponds to stronger SHG signal. By comparing time-dependent SHG (TD-SHG) signals from samples with different thicknesses of thermal oxide, we show that samples with

thinner oxide have stronger charging effect [38, 66], which is explained in terms of interface width and related charge traps. By performing spectroscopic studies, we find that a peak of the RA-SHG signal can be turned into a valley by varying photon energy. The RA-SHG signal shows eightfold symmetry at a certain critical photon energy. This critical photon energy varies monotonically with thickness of thermal oxide thus providing a means of interface identification. To study the effect of thermal oxidation on the spectra of SHG, we measure the SH spectra on a very thick thermal oxide Si(001) surface under different polarization configurations. By comparison to thinner oxide Si samples, we show that both thermal oxidation and polarization configuration affect the SH spectra.

6.2 Sample preparation and experimental conditions

To study the effect of thermal oxidation on SHG from the SiO_2-Si interface, we prepared a series of Si samples with various thermally grown oxides. The Si(001) wafers, boron doped to 1-2 $\Omega \cdot cm$, were first cleaned in an H_2SO_4/H_2O_2 solution, followed by a 100:1 H_2O/HF dip. The oxides were grown by rapid thermal oxidation in a pure O_2 environment at a temperature of 1000 ^oC. The thickness of the oxide was controlled by oxidation time; longer oxidation time corresponds to thicker oxide. The thickness of the oxide was determined by ellipsometry. Interface width was measured using x-ray scattering [94]. The crystal orientation of the Si wafers was known from the sample supplier prior to the experiment.

The experimental setup was the same as in Chapter 1. RA-SHG curves were obtained by recording the SH signal as the sample was rotated about its surface normal. TD-SHG signals were obtained by sampling the SH signal as a function of

the time of laser illumination on the sample. The laser illumination started from time zero. The test sample was held in a chamber purged by N_2 to reduce O_2 induced charging effect.

6.3 Effect of thermal oxidation on SHG

Surface SHG experiments have shown that the thermal history plays a determinant role in the structures of the interfacial transition region between the crystalline Si substrate and the amorphous SiO_2 layer [95-100]. These SHG studies were performed on the Si(111) surface. For this interface, bulk and surface SH contributions can not been separated by selecting polarization; therefore, interpretation of the results was difficult. Such a difficulty is partially circumvented by using the Si(001) surface.

6.3.1 Isotropic and anisotropic SH contributions

SHG from bulk crystalline Si includes both anisotropic and isotropic components, but SHG from the Si(001) surface or interface is only isotropic. With the polarizations (*g* or *h*) limited to *s* and *p* states, the *h*-polarized SH fields $E_{g,h}^{(2\omega)}$ from a Si(001) crystal face for the *g*-polarized incident fundamental fields E_g can be written as (see Chapter 2)

$$E_{g,p}^{(2\omega)} = [a_{0,(g,p)} + a_{4,(g,p)} \cos(4\phi)] e^{i\delta_{g,p}} E_g^2 , \qquad (6.1)$$

$$E_{g,s}^{(2\omega)} = a_{4,(g,s)} \sin(4\phi) e^{i\delta_{g,s}} E_g^2 . \qquad (6.2)$$

Here ϕ is the azimuthal angle defined as being between plane of incidence and the

[100] crystal direction. The SH intensity is proportional to the magnitude square of the SH field. The coefficients a_0 and a_4 are the isotropic and anisotropic contributions to the RA-SHG signal, respectively. They are functions of the relevant susceptibility elements, Fresnel factors, and dielectric functions, as shown in Chapter 2. Here, a_4 is chosen to be real and positive (its phase is in δ), then a_0 is complex in general and can be split into real and imaginary parts, written as $a_0 = a_{0,r} + ia_{0,i}$.

We fit the measured (*p, p*) and (*p, s*) RA-SHG signals from the series of differently thermally oxidized Si(001) samples to Eqs. (6.1) and (6.2), respectively, and obtain the isotropic and anisotropic coefficients. Figure 6.1 shows $a_{0,r,(p,p)}/a_{4,(p,p)}$ and $a_{0,i,(p,p)}/a_{4,(p,p)}$ (upper panel), and $a_{4,(p,s)}$ (lower panel) as a function of oxide thickness at different two-photon energies: 3.44 eV, 3.40 eV, and 3.26 eV. For the (*p, p*) polarization, the multiple reflection effect is cancelled out by dividing the isotropic coefficient by the anisotropic coefficient. This is the reason for using the ratios $a_{0,r,(p,p)}/a_{4,(p,p)}$ and $a_{0,i,(p,p)}/a_{4,(p,p)}$ to characterize the SiO_2-Si interface. As shown, the coefficient $a_{4,(p,s)}$ increases with increasing oxide thickness, which is consistent with the prediction that the oxide layer functions as an antireflection coating. At a two photon energy of 3.26 eV, the magnitude of $a_{0,r,(p,p)}/a_{4,(p,p)}$ decreases with decreasing interface width. Note that thinner interface width corresponds to larger oxide thickness [57, 93]. Such a trend does not hold for all photon energies. As shown, at a two-photon energy of 3.44 eV, $a_{0,r,(p,p)}/a_{4,(p,p)}$ changes from negative to positive as the oxide thickness increases, which means that its magnitude is not a monotonic function of oxide thickness any more. For all these

photon energies, the magnitude of $a_{0,i,(p,p)} / a_{4,(p,p)}$ is relatively flat with increasing interface width, except that it drops to lower values when the oxide is very thin. The strength of the anisotropic and isotropic contributions to the total SH signal also varies with photon energy, as shown Fig. 6.1.

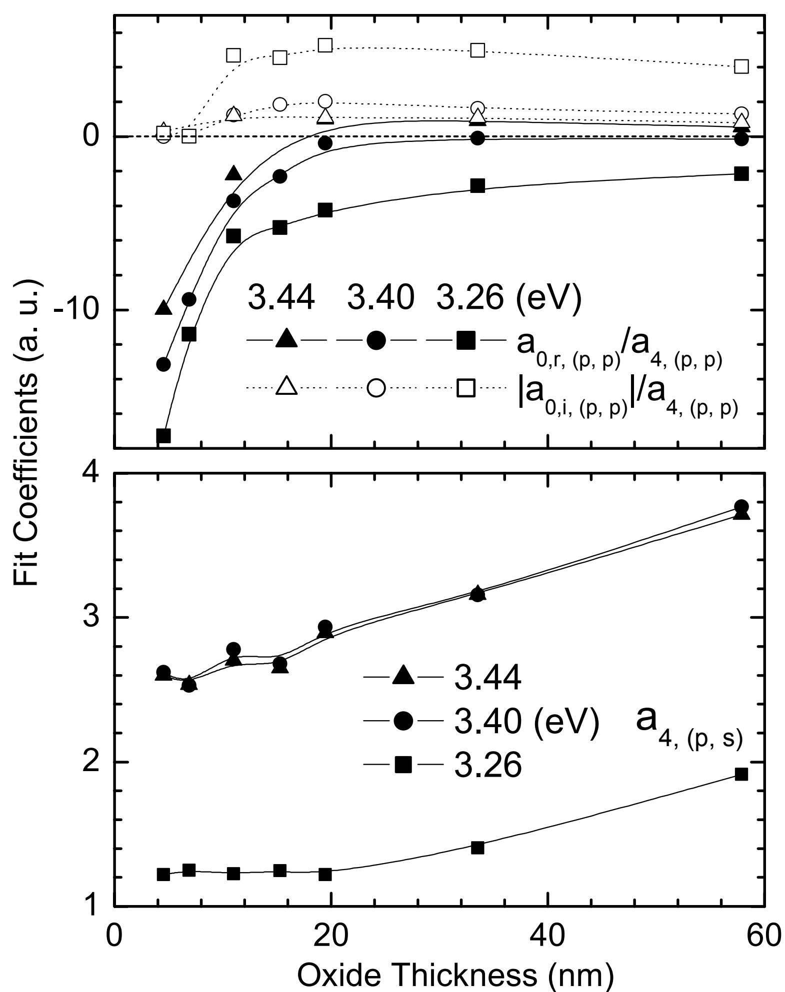

Fig. 6.1. Ratio of the isotropic to anisotropic SHG components for the (*p, p*) polarization (upper panel) and anisotropic SHG components for the (*p, s*) polarization (lower panel) as a function of oxide thickness at several two-photon energies: 3.44 eV, 3.40 eV, and 3.26 eV.

6.3.2 Phase inversion photon energy

The critical two-photon energy at which RA-SHG shows eightfold symmetry differs for different interfaces. For the (*p, p*) polarized RA-SHG, we observe that $a_{0,r,(p,p)}$ can be either positive or negative depending on the sample and on the photon energy. For a given sample, it is possible to find a critical photon energy, at which $a_{0,r,(p,p)}$ is zero, in other words, the RA-SHG signal shows eightfold symmetry. We name the critical photon energy as the phase inversion photon energy. As we showed in Chapter 4, phase inversion by varying photon energy happens for the (*s, p*) polarization. We show here that it happens for the (*p, p*) and (*q, s*) polarizations as well. In Fig. 6.2, the upper panel shows the variation of the phase inversion photon energy with oxide thickness for (*p, p*), (*s, p*), and (*q, s*) polarizations, and the lower panel shows the (*s, p*) RA-SHG curves from a 57.9 nm thick oxide covered Si(001) sample at different photon energies. The appearance of eightfold symmetry in RA-SHG curves is significant. A small deviation of photon energy from the phase inversion photon energy leads to a large change in the relative height between two adjacent peaks, which can be easily detected by eye. Therefore, the phase inversion photon energy can be accurately determined. Combining with the fact that it is sensitive to interface conditions (rather than oxide thickness), we can use it as a reliable probe for interface identification.

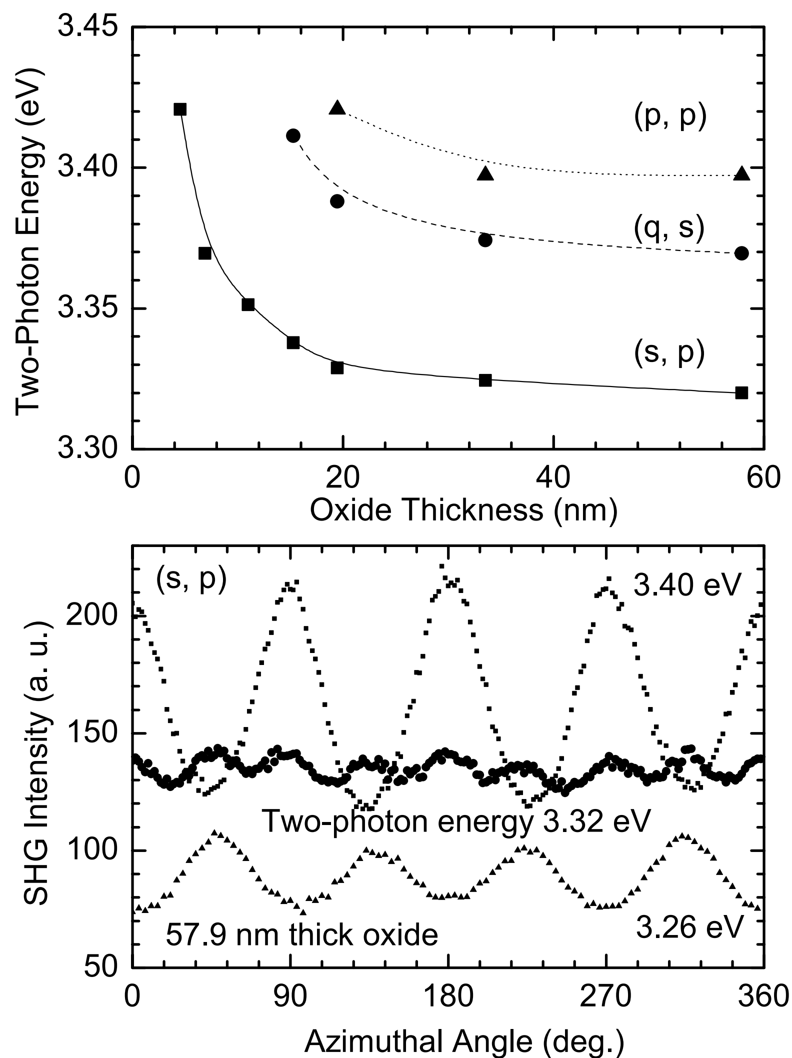

Fig. 6.2. Upper panel: oxide thickness dependence of the two-photon energy at which the RA-SHG signal shows eightfold symmetry for (*p, p*), (*q, s*), and (*s, p*) polarizations. Lower panel: RA-SHG signals from a thermally oxidized Si(001) sample with 57.9 nm thick oxide for the (*s, p*) polarization, showing either eightfold or fourfold symmetry.

6.3.3 Time-dependent SHG

Thermal oxidation greatly affects the time-dependent SHG (TD-SHG) signal, as shown in Fig. 6.3 for the (*p, p*) polarized TD-SHG signals from several Si(001) samples with different thicknesses of thermally grown oxide (and different interfaces) at a two photon energy of 3.26 eV. During the measurement, the azimuthal angle was fixed at a peak the RA-SHG signal. Before the TD-SHG measurement, the samples were fully discharged by leaving them in a dark environment for a long time. The fundamental beam started to continuously illuminate the sample at time zero. The SH signal was taken with a counting gate time of 0.5 sec. As shown, the TD-SHG signal increases rapidly with time and gradually saturates for samples with thin oxide layers, but it stays about the same value for samples with thick oxide layers. The saturated SH signal decreases with increasing thickness of the oxide layer, consistent with previous results [66]. The TD-SHG signal was measured in a N_2 (research grade purity) ambient, but no noticeable difference in the TD-SHG response was observed when the ambient was changed from N_2 to O_2. This suggests that the ambient-oxide interface is not likely responsible for the charge trapping, which makes the SH signal time-dependent. The stronger time-dependence of SHG from thinner oxide covered Si samples can be attributed to more charge traps at the SiO_2-Si interface. The number of charge traps is reduced by conducting high temperature oxidation for longer time. The observation of the time-dependence in SHG response indicates that the SH susceptibility at the SiO_2-Si interface is a dynamic rather than a static value for thin oxide covered samples. In addition, the measured SH signal depends on the charging history and the gate time of the counting system.

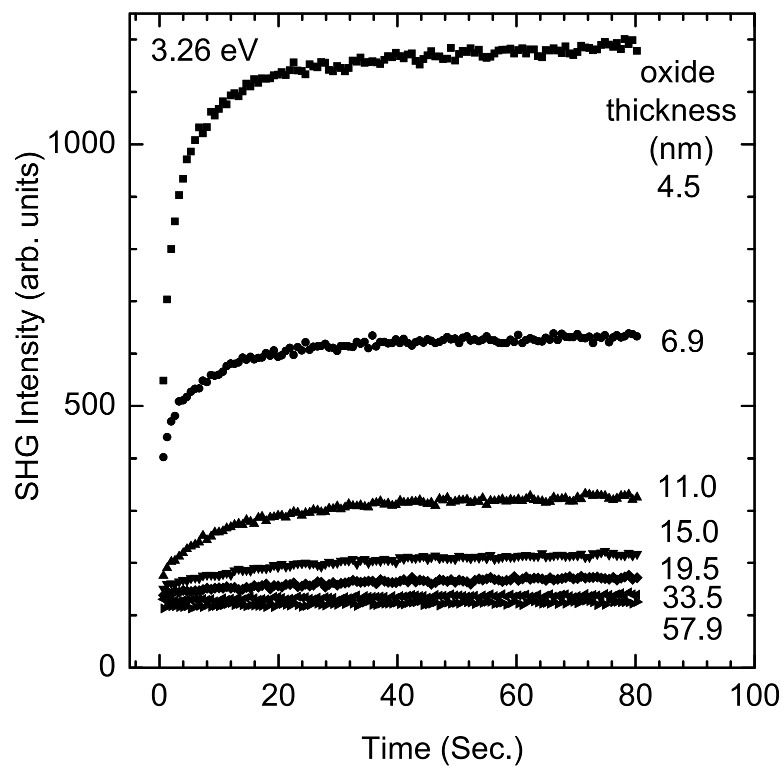

Fig. 6.3. Time-dependent SHG signal for the (*p, p*) polarization at a two-photon energy of 3.26 eV for several thermally oxidized Si(001) surfaces with different thicknesses of the oxide layer.

6.3.4 Effect of thermal oxidation on SHG spectroscopy

To systematically study the effect of thermal oxidation on SH spectra, we compare SHG from different samples. The SH spectrum is expected to change with interface conditions if the interface SH contribution dominates. Figure 6.4 shows the SH spectra from a Si(001) sample with 57.9 nm thick thermally grown oxide at a fixed azimuthal angle of 22.5^o for different polarization configurations: (*p, p*), (*s, p*), and (*q, s*). By choosing this azimuthal angle, the anisotropic SH signal is eliminated totally for the (*p, p*) and (*s, p*) polarizations and mostly for the (*q, s*) polarization. However, the measured SH signal still includes both bulk and surface contributions. Combining the SH spectra results in Chapters 3 and 4, we find that the resonant energy of 3.27 eV for the (*p, p*) polarization for the thick oxide sample is significantly red shifted from that for thin oxide samples, thus thicker oxide leads to a larger red-shift. This resonance is known as E_1 resonance because its energy is close to the E_1 critical point of the band-gap of bulk Si [68]. The directions of the observed strong energy and intensity variations of this resonance as a result of the different oxidation procedures are consistent with previous results [59]. The redshift in resonant energy was previously explained by oxide-induced lattice strain in the Si layers near the interface, leading to weakening of Si-Si bonds in these layers [33]. This explanation in terms of strain sounds reasonable, but it is probably hard to convince that it is the main effect because methods of direct measurement of the interfacial strain are very limited. The measured SH signal consists of bulk and surface contributions. In the case that there is charging effect, the electric-field-induced SHG should also be included and can be treated as an effective surface SHG. The bulk SH contribution

increases with increasing oxide thickness, but the measured total SH intensity drastically decrease with increasing oxide thickness. Therefore, the relative strength (including phase) between bulk and surface SH contributions varies strongly with oxide thickness. Interference between these two SH contributions can shift the measured resonant energy, as shown in Chapter 3.

In addition to the dependence of SH spectra on thermal oxidation, we find that resonant behavior of SHG depends strongly polarization configuration, as shown in Fig. 6.4. For the same sample, resonant energies and SH intensities clearly differ between polarizations. For the (*p, p*) polarization, the resonance energy is 3.27 eV, but for the (*q, s*) polarization, it is 3.33 eV. It is interesting to notice that this resonance almost disappears for the (*s, p*) polarization. At higher photon energies, the SH intensities for the (*q, s*) and (*s, p*) polarizations are much stronger than that for the (*p, p*) polarization. If the SH response is described by susceptibility tensors, polarization selection helps in discriminating among tensor elements. These results indicate that different tensor elements may have different spectra, and the relative importance of tensor elements depends strongly on photon energy. SHG responses for different polarization configurations represent different types of excitation and bond orientation. In addition, different orientation of the excitation field may have different ability on charge injection across the SiO_2-Si interface, which causes different band bending at the interface. For example, electrons can be excited more easily across the angstrom scale interface by an out-of-plane excitation field than an in-plane excitation field. Moreover, the relative strength between bulk and surface SH contributions may shift the apparent resonance.

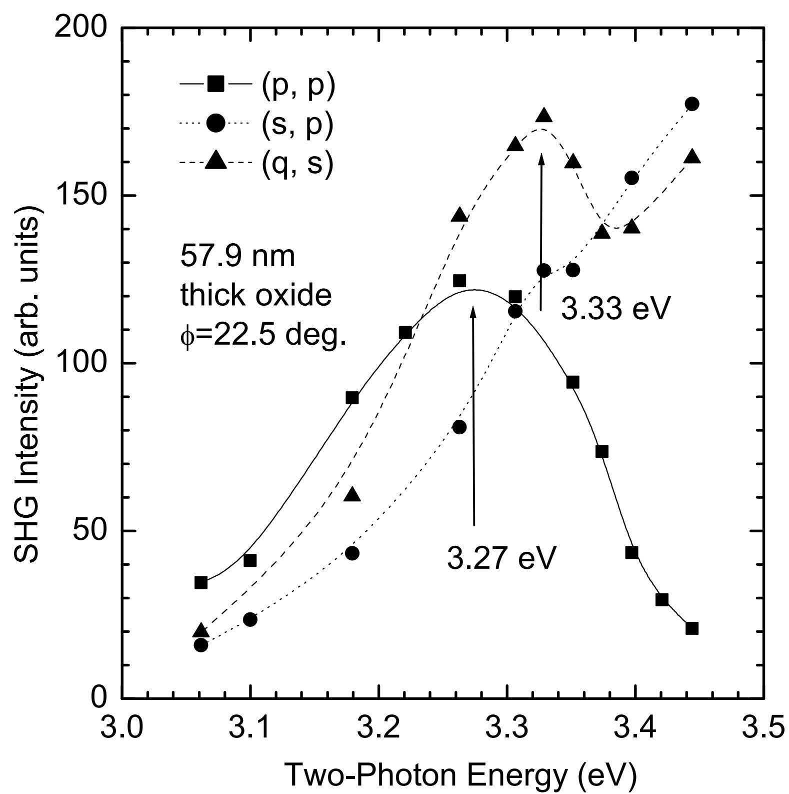

Fig. 6.4. SH spectra from a thermally oxidized Si(001) sample with 57.9 nm thick oxide at a fixed azimuthal angle of 22.5° for different polarization configurations: (*p, p*), (*s, p*), and (*q, s*).

6.4 Discussion

To explain the apparent discrepancy in the dependence of SHG on interface width between the new results and previous results [57, 58], we need to investigate the differences in experimental conditions and characterization variables used in these studies. The tunable photon energy used in this research is larger than the previous used the value of two-photon energy 2.92 eV [57]. However, photon energy in the vicinity probably does not affect the direction of variation of SHG with interface width because some photon energies used in this work are detuned from the resonance and no considerable variation with photon energy in the band from the present and previous photon energies is expected for linear and nonlinear optical properties. The observed trends of the SHG signal varying with interface width are similar for several photon energies, as shown in Fig. 6.1. The pulse spectral widths here are much narrower than the previously used pulse. The fit equations of the RA-SHG data are slightly different for the two studies. Using real isotropic fit coefficient for a_0 in the previous studies [57, 58] is apparently a crude approximation. When the (*p, p*) polarized RA-SHG signal shows eightfold symmetry at a certain photon energy, the isotropic and the anisotropic coefficients are 90° out of phase. This is a clear evidence of the phase issue in SHG. Taking into account the complex property of a_0 would be closer to the physical reality. We also notice that the anisotropic coefficients a_4 should increase with increasing thin oxide thickness because of the multiple reflection effect, but it was assumed previously to be independent of surface

preparation. These considerations may account for the discrepancy on whether the ratio $|a_{0,(p,p)}|/a_{4,(p,p)}$ increases or decreases with interface width.

The time dependence of SHG can be related to the interface width. Macroscopically, the volume of the medium with broken symmetry affects the SH intensity. Thermal oxidation performed with shorter time leaves more defects in the transition region, which can cause stronger charging effect. However, even the TD-SHG signal is taken with very short gate time so that the charging effect is negligible at the initial stage, the initial SH signal from samples with thinner oxides is still stronger than that from samples with thicker oxide. This is qualitatively understood in terms of the fact that the mobility of interfacial electrons is greater for thicker interface width than for thinner interface.

In the future work, we hope to study how the TD-SHG signals change with oxide thickness while the SiO_2-Si(001) interface stays the same. This can be done by using a series of samples prepared by etching a very thick thermally grown oxide on the Si(001) surface to various thicknesses. If the SH signal decreases with decreasing oxide thickness and the TD-SHG signal shows similar behavior of negligible time-dependence for different samples, our results in this chapter will be further confirmed.

6.5 Summary

We have studied the effect of thermal oxidation on SHG by using a series of Si(001) samples with different oxidation conditions. By comparing the (*p, s*) polarized RA-SHG, we found that multiple reflection in the oxide film enhances the measured SH signal. By comparing the (*p, p*) polarized RA-SHG, we found the

interface condition can be characterized by the ratio of the isotropic coefficient to the anisotropic coefficient (multiplication effect is cancelled out). Through spectroscopic studies, we found that the RA-SHG signal can be either fourfold symmetric or eightfold symmetric depending on photon energy. This leads to the important issues of the relative phase between the isotropic and anisotropic SH contributions. Eightfold symmetric RA-SHG signals were found for all the (*p, p*), (*s, p*) and (*q, s*) polarizations, and the corresponding photon energy varies monotonically with interface width, thus it provides a reliable way for interface identification. We showed that the time-dependence of the SH signal is stronger for a larger interface width. Thermal oxidation affects SH spectra and the resonant behaviors for the same sample are significantly different for different polarization configuration. These results suggest that surface SHG is a sensitive probe for oxidized Si interfaces, but a probe with multiple effects.

Chapter 7

Conclusions

The experiments described here have helped improve the understanding the physics of SHG at Si surfaces or interfaces. The experimental results show that the SH spectroscopy from Si surfaces is closely related to the band structure of the bulk Si, but surface modification can shift the apparent resonance through interference among or between different SH contributions. The major advantage of SHG is the extreme surface sensitivity. As shown for oxidized Si, hydrogen terminated Si, and ultrathin Cr coated SiO_2-Si surfaces, the measured RA-SHG signals for appropriate polarizations at a certain photon energy are apparently different between samples. This sensitivity can be greatly enhanced by combination with the phase information of the surface SH field. The observed peak-to-valley transition of RA-SHG by varying photon energy or by surface modification clearly demonstrates the phase variation of the surface SH field. With this information, SHG from Cr-SiO_2-Si structures and thermally oxidized Si surfaces have been comprehensively studied and new results of SHG have been obtained with respect to the sources of SHG.

A major weakness of the SHG technique is the lack of specificity for a certain given interfacial property. The observed variation of SHG with surface condition is possibly explained by alternative effects. Many conclusions drawn from SHG studies are not straightforward. It is also clear that SHG from SiO_2-Si interfaces is considerably time-dependent, especially for ultrathin oxide surfaces. Measured SH signals depend strongly on experimental conditions, thus quantitative characterization

is difficult. Another problem with the SHG probe is the possibility of damaging the surface with the high field intensity required to generate an observable response. For Si surfaces, our SHG studies so far have given adequate signals well below the threshold for optical damage. Further understanding of the interfacial electronic structure and a feasible microscopic theory are needed to explain microscopically the phase variation of SHG and the SH spectroscopy.

However, the high sensitivity of the SHG probe to interface properties can be put to the best use by comparing SH signals from different surfaces, as I demonstrated in this thesis. The use of SHG to monitor the time-evolution of the surface or interface and the carrier dynamics at the surface or interface is also very exciting. I have performed a new spectroscopic study of SHG from technologically important Si(001) surfaces. The SH spectroscopy with the phase information of the SH field is far more sensitive to interface properties than that with the SH intensity only.

Bibliography

[1] P. A. Franken, A. E. Hill, C. W. Peters, and G. Weinreich, "Generation of Optical Harmonics" Phys. Rev. Lett. **7**, 118 (1961).

[2] N. Bloembergen, *Nonlinear Optics* (Benjamin, New York, 1965).

[3] Y. R. Shen, *The Principles of Nonlinear Optics* (Wiley, New York, 1984).

[4] M. Schubert and B. Wilhelmi, *Nonlinear Optics and Quantum Electronics* (Wiley, New York, 1986).

[5] R. W. Boyd, *Nonlinear Optics* (Academic Press, San Diego, CA, 2003).

[6] J. A. Armstrong, N. Blembergen, J. Ducuing, and P. S. Pershan, "Interactions between Light Waves in a Nonlinear Dielectric" Phys. Rev. **127**, 1918 (1962).

[7] N. Bleombergen and P. S. Pershan, "Light Waves at the Boundary of Nonlinear Media" Phys. Rev. **128**, 606 (1962).

[8] J. Ducuing and N. Bloembergen, "Observation of Reflected Light Harmonics at the Boundary of Piezoelectric Crystals" Phys. Rev. Lett. **10**, 474 (1963).

[9] R. K. Chang, J. Ducuing, and N. Bloembergen, "Relative Phase Measurement between Fundamental and Second-Harmonic Light" Phys. Rev. Lett. **15**, 6 (1965).

[10] R. W. Terhune, P. D. Marker, and C. M. Savage, "Optical Harmonic Generation in Calcite" Phys. Rev. Lett. **8**, 404 (1962).

[11] J. E. Bjorkholm and A. E. Siegman, "Accurate cw Measurements of Optical Second-Harmonic Generation in Ammonium Dihydrogen Phosphate and Calcite" Phys. Rev. **154**, 851 (1967).

[12] N. Bloembergen, R. K. Chang, S. S. Jha, and C. H. Lee, "Optical Second-Harmonic Generation in Reflection from Medium with Inversion Symmetry" Phys. Rev. **174**, 813 (1968).

[13] C. C. Wang, "Second-Harmonic Generation of Light at the Boundary of an Isotropic Medium" Phys. Rev. **178**, 1457 (1969).

[14] F. Brown and M. M., "Effect of Adsorbed Surface Layers on Second-Harmonic Light from Silver" Phys. Rev. **185**, 985 (1969).

[15] J. M. Chen, J. R. Bower, C. S. Wang, and C. H. Lee, "Optical Second Harmonic Generation from Submonolayer Na-covered Ge Surfaces" Opt. Commun. **9**, 132 (1973).

[16] N. Bloembergen, "Surface Nonlinear Optics: A Historical Overview" Appl. Phys. B **68**, 289 (1999).

[17] M. C. Downer, "A New Low for Nonlinear Optics" Science **298**, 373 (2002).

[18] Y. R. Shen, "Optical 2nd Harmonic-Generation at Interfaces" Annu. Rev. Phys. Chem. **40**, 327 (1989).

[19] Y. R. Shen, "Surface-Properties Probed by 2nd-Harmonic and Sum-Frequency Generation" Nature **337**, 519 (1989).

[20] G. L. Richmond, J. M. Robinson, and V. L. Shannon, "2nd Harmonic-Generation Studies of Interfacial Structure and Dynamics" Prog. Surf. Sci. **28**, 1 (1988).

[21] T. F. Heinz, C. K. Chen, D. Richard, and Y. R. Shen, "Spectroscopy of Molecular Monolayers by Resonant 2nd-Harmonic Generation" Phys. Rev. Lett. **48**, 478 (1982).

[22] T. F. Heinz, H. W. K. Tom, and Y. R. Shen, "Determination of Molecular-Orientation of Monolayer Adsorbates by Optical 2nd-Harmonic Generation" Phys. Rev. A **28**, 1883 (1983).

[23] D. Guidotti, T. A. Driscoll, and H. J. Gerritsen, "2nd Harmonic-Generation in Centro-Symmetric Semiconductors" Solid State Commun. **46**, 337 (1983).

[24] H. W. K. Tom, T. F. Heinz, and Y. R. Shen, "2nd-Harmonic Reflection from Silicon Surfaces and Its Relation to Structural Symmetry" Phys. Rev. Lett. **51**, 1983 (1983).

[25] J. A. Litwin, J. E. Sipe, and H. M. Vandriel, "Picosecond and Nanosecond Laser-Induced 2nd-Harmonic Generation from Centrosymmetric Semiconductors" Phys. Rev. B **31**, 5543 (1985).

[26] P. Guyotsionnest, W. Chen, and Y. R. Shen, "General-Considerations on Optical 2nd-Harmonic Generation from Surfaces and Interfaces" Phys. Rev. B **33**, 8254 (1986).

[27] J. E. Sipe, D. J. Moss, and H. M. van Driel, "Phenomenological Theory of Optical 2nd-Harmonic and 3rd- Harmonic Generation from Cubic Centrosymmetric Crystals" Phys. Rev. B **35**, 1129 (1987).

[28] J. E. Sipe, V. Mizrahi, and G. I. Stegeman, "Fundamental Difficulty in the Use of 2nd-Harmonic Generation as a Strictly Surface Probe" Phys. Rev. B **35**, 9091 (1987).

[29] Y. R. Shen, "Surfaces Probed by Nonlinear Optics" Surf. Sci. **300**, 551 (1994).

[30] J. F. McGilp, "Optical Characterization of Semiconductor Surfaces and Interfaces" Prog. Surf. Sci. **49**, 1 (1995).

[31] G. Lüpke, "Characterization of Semiconductor Interfaces by Second-Harmonic Generation" Surf. Sci. Rep. **35**, 77 (1999).

[32] D. E. Spence, P. N. Kean, and W. Sibbett, "60-Fsec Pulse Generation from a Self-Mode-Locked Ti-Sapphire Laser" Opt. Lett. **16**, 42 (1991).

[33] W. Daum, H. J. Krause, U. Reichel, and H. Ibach, "Identification of Strained Silicon Layers at Si-SiO_2 Interfaces and Clean Si Surfaces by Nonlinear-Optical Spectroscopy" Phys. Rev. Lett. **71**, 1234 (1993).

[34] B. S. Mendoza and W. L. Mochan, "Polarizable-Bond Model for Second-Harmonic Generation" Phys. Rev. B **55**, 2489 (1997).

[35] B. S. Mendoza, A. Gaggiotti, and R. Del Sole, "Microscopic Theory of Second Harmonic Generation at Si(100) Surfaces" Phys. Rev. Lett. **81**, 3781 (1998).

[36] O. A. Aktsipetrov, A. A. Fedyanin, V. N. Golovkina, and T. V. Murzina, "Optical Second-Harmonic Generation Induced by a Dc Electric-Field at the Si-SiO_2 Interface" Opt. Lett. **19**, 1450 (1994).

[37] C. Ohlhoff, G. Lüpke, C. Meyer, and H. Kurz, "Static and High-Frequency Electric Fields in Silicon MOS and MS Structures Probed by Optical Second-Harmonic Generation" Phys. Rev. B **55**, 4596 (1997).

[38] J. G. Mihaychuk, J. Bloch, Y. Liu, and H. M. van Driel, "Time-Dependent 2nd-Harmonic Generation from the Si-SiO_2 Interface Induced by Charge-Transfer" Opt. Lett. **20**, 2063 (1995).

[39] K. E. Petersen, "Silicon as a Mechanical Material" P. IEEE **70**, 420 (1982).

[40] C. Kittel, *Introduction to Solid State Physics* (Wiley, New York, 1996).

[41] Y. Q. An and S. T. Cundiff, "Bulk and Surface Contributions to Resonant Second-Harmonic Generation from Si(001) surfaces" Appl. Phys. Lett. **81**, 5174 (2002).

[42] Y. Q. An and S. T. Cundiff, "Phase Inversion in Rotational-Anisotropy of Second-Harmonic Generation at Si(001) Interfaces" Phys. Rev. B **67**, 193302 (2003).

[43] T. H. DiStefano and D. E. Eastman, "Photoemission Measurements of Valence Levels of Amorphous SiO_2" Phys. Rev. Lett. **27**, 1560 (1971).

[44] T. H. DiStefano and D. E. Eastman, "Band Edge of Amorphous SiO_2 by Photoinjection and Photoconductivity Measurements" Solid State Commun. **9**, 2259 (1971).

[45] P. S. Pershan, "Nonlinear Optical Properties of Solids: Energy Considerations" Phys. Rev. **130**, 919 (1963).

[46] S. V. Popov, Y. P. Svirko, and N. I. Zheludev, *Susceptibility tensors for nonlinear optics* (Institute of Physics Pub., Bristol, [Eng.]; Philadelphia, Pa, 1995).

[47] G. Lüpke, D. J. Bottomley, and H. M. Vandriel, "2nd-Harmonic and 3rd-Harmonic Generation from Cubic Centrosymmetric Crystals with Vicinal Faces - Phenomenological Theory and Experiment" J. Opt. Soc. Am. B **11**, 33 (1994).

[48] J. E. Sipe, "New Green-Function Formalism for Surface Optics" J. Opt. Soc. Am. B **4**, 481 (1987).

[49] R. J. Pressley, in *Handbook of Lasers*, edited by R. J. Pressley (Chemical Rubber Company, Cleveland, 1971).

[50] M. D. Levenson, *Introduction to Nonlinear Laser Spectroscopy* (Academic, New York, 1982).

[51] V. Mizrahi and J. E. Sipe, "Phenomenological Treatment of Surface 2nd-Harmonic Generation" J. Opt. Soc. Am. B **5**, 660 (1988).

[52] C. W. Vanhasselt, M. A. Verheijen, and T. Rasing, "Vicinal Si(111) Surfaces Studied by Optical 2nd-Harmonic Generation - Step-Induced Anisotropy and Surface-Bulk Discrimination" Phys. Rev. B **42**, 9263 (1990).

[53] D. J. Bottomley, G. Lüpke, C. Meyer, and Y. Makita, "Exact Separation of Surface and Bulk Contributions to Anisotropic 2nd-Harmonic Generation from Cubic Centrosymmetric Media" Opt. Lett. **20**, 453 (1995).

[54] G. Lüpke, "Characterization of Semiconductor Interfaces by Second-Harmonic Generation" Surf. Sci. Rep. **35**, 77 (1999).

[55] G. Lüpke, D. J. Bottomley, and H. M. van Driel, "SiO_2/Si Interfacial Structure on Vicinal Si(100) Studied with 2nd-Harmonic Generation" Phys. Rev. B **47**, 10389 (1993).

[56] S. T. Cundiff, W. H. Knox, F. H. Baumann, K. W. Evans-Lutterodt, and M. L. Green, "Second-Harmonic Generation at the Interface between Si(100) and Thin SiO_2 Layers" J. Vac. Sci. Technol. A **16**, 1730 (1998).

[57] S. T. Cundiff, W. H. Knox, F. H. Baumann, K. W. EvansLutterodt, M. T. Tang, M. L. Green, and H. M. van Driel, "Si/SiO_2 Interface Roughness: Comparison between Surface Second Harmonic Generation and X-ray Scattering" Appl. Phys. Lett. **70**, 1414 (1997).

[58] J. I. Dadap, B. Doris, Q. Deng, M. C. Downer, J. K. Lowell, and A. C. Diebold, "Randomly Oriented Angstrom-Scale Microroughness at the Si(100) SiO_2 Interface Probed by Optical 2nd-Harmonic Generation" Appl. Phys. Lett. **64**, 2139 (1994).

[59] G. Erley and W. Daum, "Silicon Interband Transitions Observed at Si(100)-SiO_2 Interfaces" Phys. Rev. B **58**, R1734 (1998).

[60] Y. R. Shen, "Surface Contribution versus Bulk Contribution in Surface Nonlinear Optical Spectroscopy" Appl. Phys. B **68**, 295 (1999).

[61] J. I. Dadap, Z. Xu, X. F. Hu, M. C. Downer, N. M. Russell, J. G. Ekerdt, and O. A. Aktsipetrov, "Second-Harmonic Spectroscopy of a Si(001) Surface during Calibrated Variations in Temperature and Hydrogen Coverage" Phys. Rev. B **56**, 13367 (1997).

[62] K. Kemnitz, K. Bhattacharyya, J. M. Hicks, G. R. Pinto, K. B. Eisenthal, and T. F. Heinz, "The Phase of 2nd-Harmonic Light Generated at an Interface and Its Relation to Absolute Molecular-Orientation" Chem Phys Lett **131**, 285 (1986).

[63] J. Chen, S. Machida, and Y. Yamamoto, "Simultaneous Measurement of Amplitude and Phase in Surface Second-Harmonic Generation" Opt. Lett. **23**, 676 (1998).

[64] W. Kern, in *Handbook of Semiconductor Wafer Cleaning Technology*, edited by W. Kern (Noyes Publications, New Jersey, 1993), p. 49.

[65] G. S. Higashi, Y. J. Chabal, G. W. Trucks, and K. Raghavachari, "Ideal Hydrogen Termination of the Si-(111) Surface" Appl. Phys. Lett. **56**, 656 (1990).

[66] J. Bloch, J. G. Mihaychuk, and H. M. van Driel, "Electron Photoinjection from Silicon to Ultrathin SiO_2 Films via Ambient Oxygen" Phys. Rev. Lett. **77**, 920 (1996).

[67] D. E. Aspnes, in *Properties of Crystalline Silicon*, edited by R. Hull (IEE, London, 1999), p. 677.

[68] A. Daunois and D. E. Aspnes, "Electroreflectance and Ellipsometry of Silicon from 3 to 6 eV" Phys. Rev. B **18**, 1824 (1978).

[69] J. I. Dadap, X. F. Hu, M. H. Anderson, M. C. Downer, J. K. Lowell, and O. A. Aktsipetrov, "Optical Second-Harmonic Electroreflectance Spectroscopy of a Si(001) Metal-Oxide-Semiconductor Structure" Phys. Rev. B **53**, R7607 (1996).

[70] P. Godefroy, W. deJong, C. W. van Hasselt, M. A. C. Devillers, and T. Rasing, "Electric Field Induced Second Harmonic Generation Spectroscopy on a Metal-Oxide-Silicon Structure" Appl. Phys. Lett. **68**, 1981 (1996).

[71] O. A. Aktsipetrov, A. A. Fedyanin, A. V. Melnikov, E. D. Mishina, A. N. Rubtsov, M. H. Anderson, P. T. Wilson, H. ter Beek, X. F. Hu, J. I. Dadap, and M. C. Downer, "DC-Electric-Field-Induced and Low-Frequency Electromodulation Second-Harmonic Generation Spectroscopy of Si(001)-SiO_2 Interfaces" Phys. Rev. B **60**, 8924 (1999).

[72] M. Cini, "Simple-Model of Electric-Dipole 2nd-Harmonic Generation from Interfaces" Phys. Rev. B **43**, 4792 (1991).

[73] C. Boulas, J. V. Davidovits, F. Rondelez, and D. Vuillaume, "Suppression of Charge Carrier Tunneling through Organic Self-Assembled Monolayers" Phys. Rev. Lett. **76**, 4797 (1996).

[74] K. Kassmi, J. L. Prom, and G. Sarrabayrouse, "Electrical-Conduction in MOS Capacitors with an Ultra-Thin Oxide Layer" Solid State Electron. **34**, 509 (1991).

[75] J. R. Power, J. D. Omahony, S. Chandola, and J. F. Mcgilp, "Resonant Optical 2nd-Harmonic Generation at the Steps of Vicinal Si(001)" Phys. Rev. Lett. **75**, 1138 (1995).

[76] J. G. Mihaychuk, N. Shamir, and H. M. van Driel, "Multiphoton Photoemission and Electric-Field-Induced Optical Second-Harmonic Generation as Probes of Charge Transfer across the Si/SiO_2 Interface" Phys. Rev. B **59**, 2164 (1999).

[77] C. H. Lee, R. K. Chang, and N. Bloembergen, "Nonlinear Electroreflectance in Silicon and Silver" Phys. Rev. Lett. **18**, 167 (1967).

[78] C. S. Chang and J. T. Lue, "Optical Second Harmonic Generation from Thin Silver Films" Surf. Sci. **393**, 231 (1997).

[79] J. Dabrowski and H.-J. Müssig, *Silicon Surfaces and Formation of Interfaces: Basic Science in the Industrial World* (World Scientific, Singapore, 2000).

[80] Y. D. Glinka, W. Wang, S. K. Singh, Z. Marka, S. N. Rashkeev, Y. Shirokaya, R. Albridge, S. T. Pantelides, N. H. Tolk, and G. Lucovsky, "Characterization of Charge-Carrier Dynamics in Thin Oxide Layers on Silicon by Second Harmonic Generation" Phys. Rev. B **65**, 193103 (2002).

[81] V. Fomenko, C. Hurth, T. Ye, and E. Borguet, "Second Harmonic Generation Investigations of Charge Transfer at Chemically-Modified Semiconductor Interfaces" J. Appl. Phys. **91**, 4394 (2002).

[82] V. Fomenko, J. F. Lami, and E. Borguet, "Nonquadratic Second-Harmonic Generation from Semiconductor-Oxide Interfaces" Phys. Rev. B **6312**, 121316 (2001).

[83] N. Shamir, J. G. Mihaychuk, and H. M. van Driel, "Trapping and Detrapping of Electrons Photoinjected from Silicon to Ultrathin SiO_2 Overlayers. I. In Vacuum and in the Presence of Ambient Oxygen" J. Appl. Phys. **88**, 896 (2000).

[84] H. W. K. Tom, "Studies of Surfaces Using Optical Second-Harmonic Generation" Ph.D. dissertation, UC-Berkeley, 1984

[85] H. W. K. Tom, C. M. Mate, X. D. Zhu, J. E. Crowell, T. F. Heinz, G. A. Somorjai, and Y. R. Shen, "Surface Studies by Optical 2nd-Harmonic Generation - the Adsorption of O_2, CO, and Sodium on the Rh(111) Surface" Phys. Rev. Lett. **52**, 348 (1984).

[86] S. V. Govorkov, N. I. Koroteev, G. I. Petrov, I. L. Shumay, and V. V. Yakovlev, "Laser Nonlinear-Optical Probing of Silicon/SiO_2 Interfaces - Surface Stress Formation and Relaxation" Appl. Phys. A **50**, 439 (1990).

[87] I. L. Lyubchanskii, N. N. Dadoenkova, M. I. Lyubchanskii, T. Rasing, J. W. Jeong, and S. C. Shin, "Second-Harmonic Generation from Realistic Film-Substrate Interfaces: The Effects of Strain" Appl. Phys. Lett. **76**, 1848 (2000).

[88] R. W. J. Hollering and M. Barmentlo, "Symmetry Analysis of Vicinal(111) Surfaces by Optical 2nd-Harmonic Generation" Opt. Commun. **88**, 141 (1992).

[89] G. G. Malliaras, H. A. Wierenga, and T. Rasing, "Study of the Step Structure of Vicinal Si(110) Surfaces Using Optical 2nd-Harmonic Generation" Surf. Sci. **287**, 703 (1993).

[90] C. W. Vanhasselt, M. A. C. Devillers, T. Rasing, and O. A. Aktsipetrov, "2nd-Harmonic Generation from Thick Thermal Oxides on Si(111) - the Influence of Multiple Reflections" J. Opt. Soc. Am. B **12**, 33 (1995).

[91] C. W. Vanhasselt, E. Mateman, M. A. C. Devillers, T. Rasing, A. A. Fedyanin, E. D. Mishina, O. A. Aktsipetrov, and J. C. Jans, "Oxide-Thickness Dependence of 2nd-Harmonic Generation Thick Thermal Oxides on Si(111)" Surf. Sci. **333**, 1367 (1995).

[92] O. A. Aktsipetrov, A. A. Fedyanin, E. D. Mishina, A. A. Nikulin, A. N. Rubtsov, C. W. vanHasselt, M. A. C. Devillers, and T. Rasing, "Macroscopic Size Effects in Second Harmonic Generation from Si(111) Coated by Thin

Oxide Films: The Role of Optical Casimir Nonlocality" Phys. Rev. Lett. **78**, 46 (1997).

[93] M. T. Tang, K. W. Evanslutterodt, G. S. Higashi, and T. Boone, "Roughness of the Silicon (001)/SiO_2 Interface" Appl. Phys. Lett. **62**, 3144 (1993).

[94] J. L. Dawson, K. Krisch, K. W. Evanslutterodt, M. T. Tang, L. Manchanda, M. L. Green, D. Brasen, G. S. Higashi, and T. Boone, "Kinetic Smoothening - Growth Thickness Dependence of the Interface Width of the Si(001)/SiO_2 Interface" J. Appl. Phys. **77**, 4746 (1995).

[95] U. Emmerichs, C. Meyer, H. J. Bakker, H. Kurz, C. H. Bjorkman, C. E. Shearon, Y. Mao, T. Yasuda, Z. Jing, G. Lucovsky, and J. L. Whitten, "2nd-Harmonic Response of Chemically-Modified Vicinal Si(111) Surfaces" Phys. Rev. B **50**, 5506 (1994).

[96] H. Hirayama, F. Ito, and K. Watanabe, "Effect of Hydrogen Annealing on 2nd-Harmonic Generation from SiO_2/Si(111) Interfaces" J. Vac. Sci. Technol. A-Vac. Surf. Films **13**, 750 (1995).

[97] H. Hirayama and K. Watanabe, "Annealing Effect on Native-Oxide/Si(111) Interfaces Studied by 2nd-Harmonic Generation" Phys. Rev. B **51**, 14717 (1995).

[98] K. Watanabe, H. Hirayama, and M. Kawata, "Oxide-Nitride-Oxide/Si(111) Interfaces Analyzed by Optical 2nd-Harmonic Generation" Appl. Phys. Lett. **66**, 2232 (1995).

[99] G. Lucovsky, D. R. Lee, S. V. Hattangady, H. Niimi, S. Gandhi, C. Parker, Z. Jing, J. L. Whitten, and J. R. Hauser, "Local Atomic Structure and Electrical Properties of Nitrided Si-SiO_2 Interfaces Produced by Low-Temperature Plasma Processing and Rapid Thermal Annealing, and Explained by ab-initio Quantum Chemistry Calculations" Appl. Surf. Sci. **104**, 335 (1996).

[100] G. Lucovsky, A. Banerjee, H. Niimi, K. Koh, B. Hinds, C. Meyer, G. Lüpke, and H. Kurz, "Elimination of Sub-oxide Transition Regions at Si-SiO_2 Interfaces by Rapid Thermal Annealing at 900 Degrees C" Appl. Surf. Sci. **117**, 202 (1997).

Appendix

SHG from vicinal Si(001) surfaces

Here we present the results of rotational-anisotropy SHG (RA-SHG) from vicinal Si(001) surfaces. The surface normal direction of the vicinal Si(001) sample is away from the principal [001] crystal axis for a small offset angle, α , which is named as vicinal angle, as shown in Fig. 2.2 in Chapter 2. Moreover, the offset direction is chosen to be in a mirror plane of symmetry of the Si crystal. The vicinal angle dependence of the (*p, p*) polarized RA-SHG signal is shown in Fig. A.1. The photon energy dependence of the RA-SHG signal from vicinal Si(001) surfaces for different polarization configurations are shown in Figs. A.2, A.3, A4, and A.5. These results will not only help improve the understanding of surface SHG, but will also help with the understanding of the step structures and energies on vicinal Si surfaces or interfaces.

The experimental conditions were the same as in Chapter 3, except that the spectroscopic studies here were also performed at higher photon energies, which were obtained by frequency doubling of the output of an OPO, as described in Chapter 1. All measurements were carried out at room temperature in a N_2 ambient.

Three sets of vicinal Si(001) samples were investigated. The first set were natively oxidized vicinal Si(001) samples with different vicinal angles of 0°, 1°, 2°, 3°, 4°, and 5°, designated as NO-Si V. The [001] crystal direction of the vicinal (off axis) Si(001) wafer was off from the surface normal toward the [110] direction for a small vicinal angle. Two more sets of samples, the thermally oxidized vicinal Si(001) samples, designated as TO-Si V, and the hydrogen terminated vicinal Si(001) samples,

designated as H-Si V, were prepared from the NO-Si V samples with the same preparation conditions as in Chapter 3.

The theoretical predictions of the symmetry properties of the RA-SHG signals from vicinal Si(001) surfaces are shown as Eqs. (2.40a) and (2.40b) in Chapter 2. The SH intensity in all of the figures is normalized in the same way as that in Chapter 3. It is important to note that the azimuthal angle is defined to be between the plane of incidence and the projection of the [110] axis in the surface plane. Moreover, when the azimuthal angle $\psi=0$, the incident beam is toward the downward miscut direction of the vicinal surface (or downward steps on the vicinal surface), as shown in Fig. 2.2 in Chapter 2.

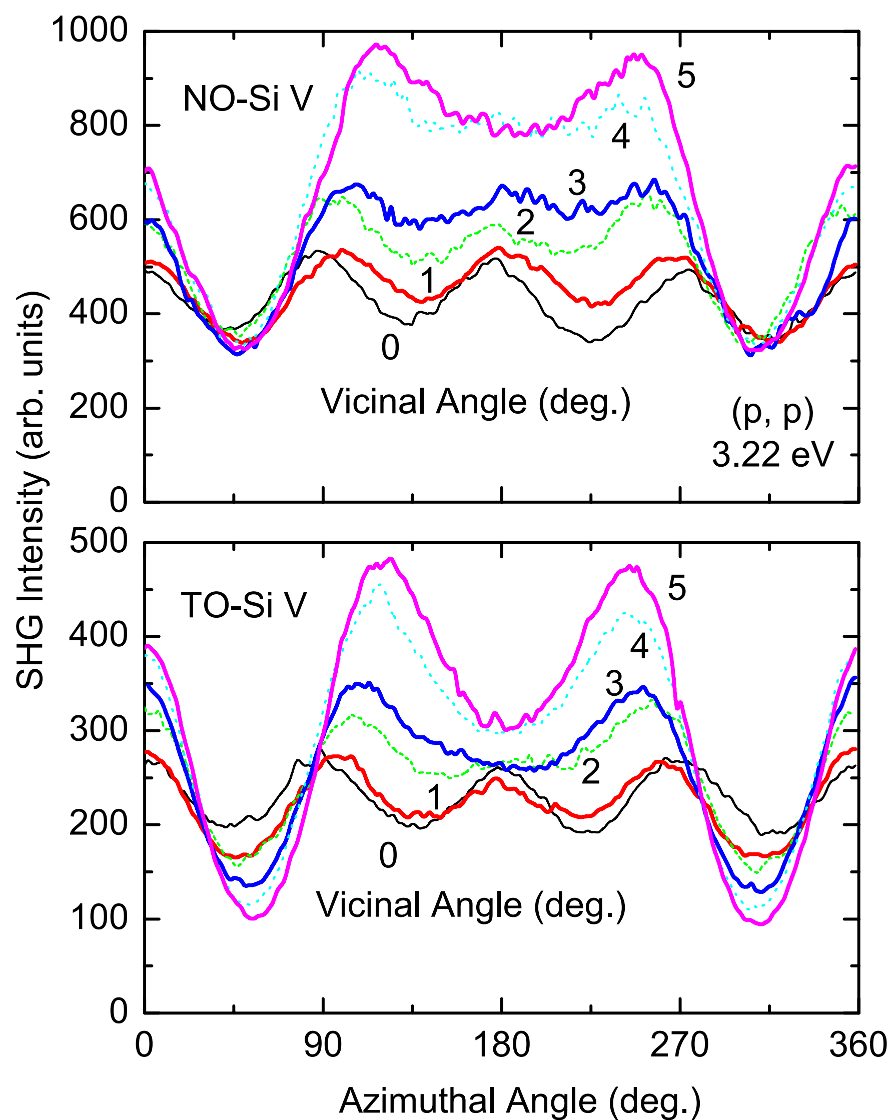

Fig. A.1. (*p, p*) polarized RA-SHG signals at a two-photon energy of 3.22 eV from natively oxidized vicinal Si(001) surfaces (NO-Si V) (upper panel) and thermally oxidized vicinal Si(001) surfaces (TO-Si V) (lower panel) with different vicinal angles of 0°, 1°, 2°, 3°, 4°, and 5°.

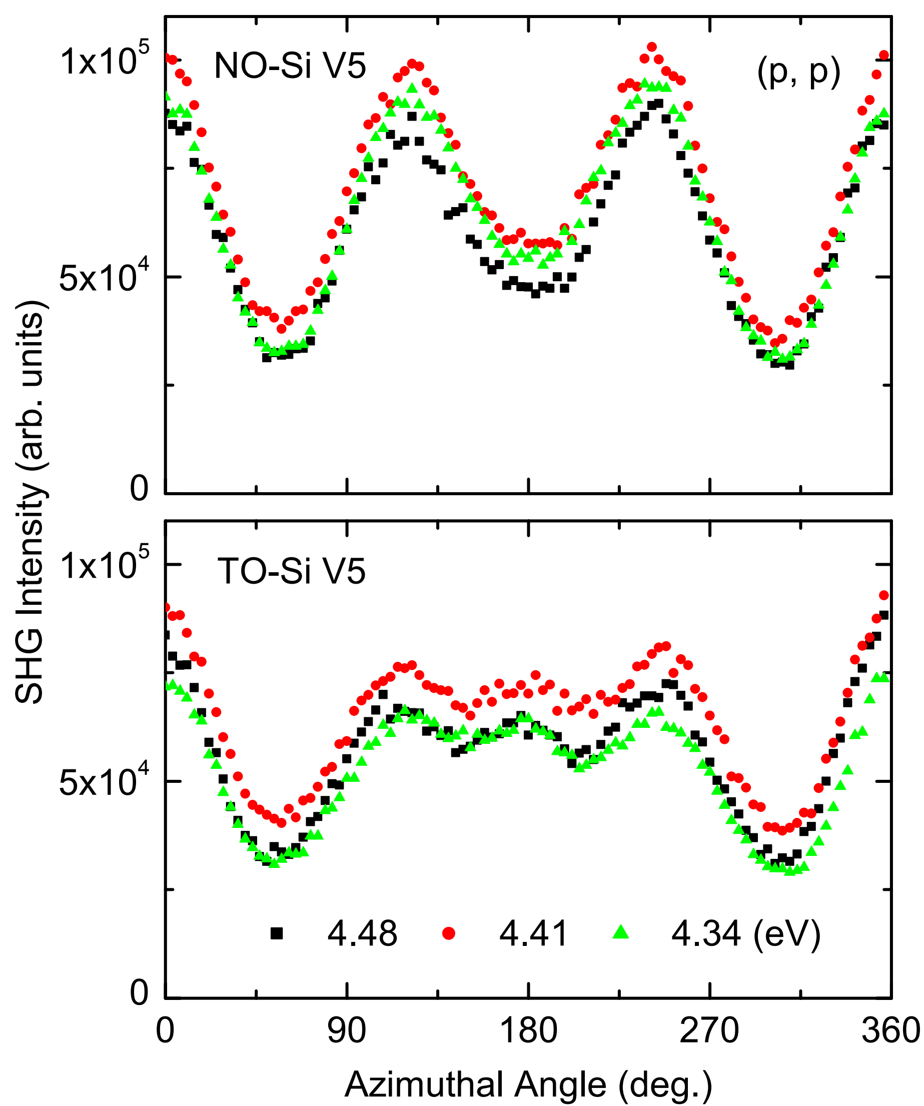

Fig. A.2. (*p, p*) polarized RA-SHG signals from a natively oxidized Si sample with vicinal angle of 5° (NO-Si V5) (upper panel) and a thermally oxidized Si sample with vicinal angle of 5° (TO-Si V5) (lower panel) at two-photon energies 4.34 eV, 4.41 eV, and 4.48 eV.

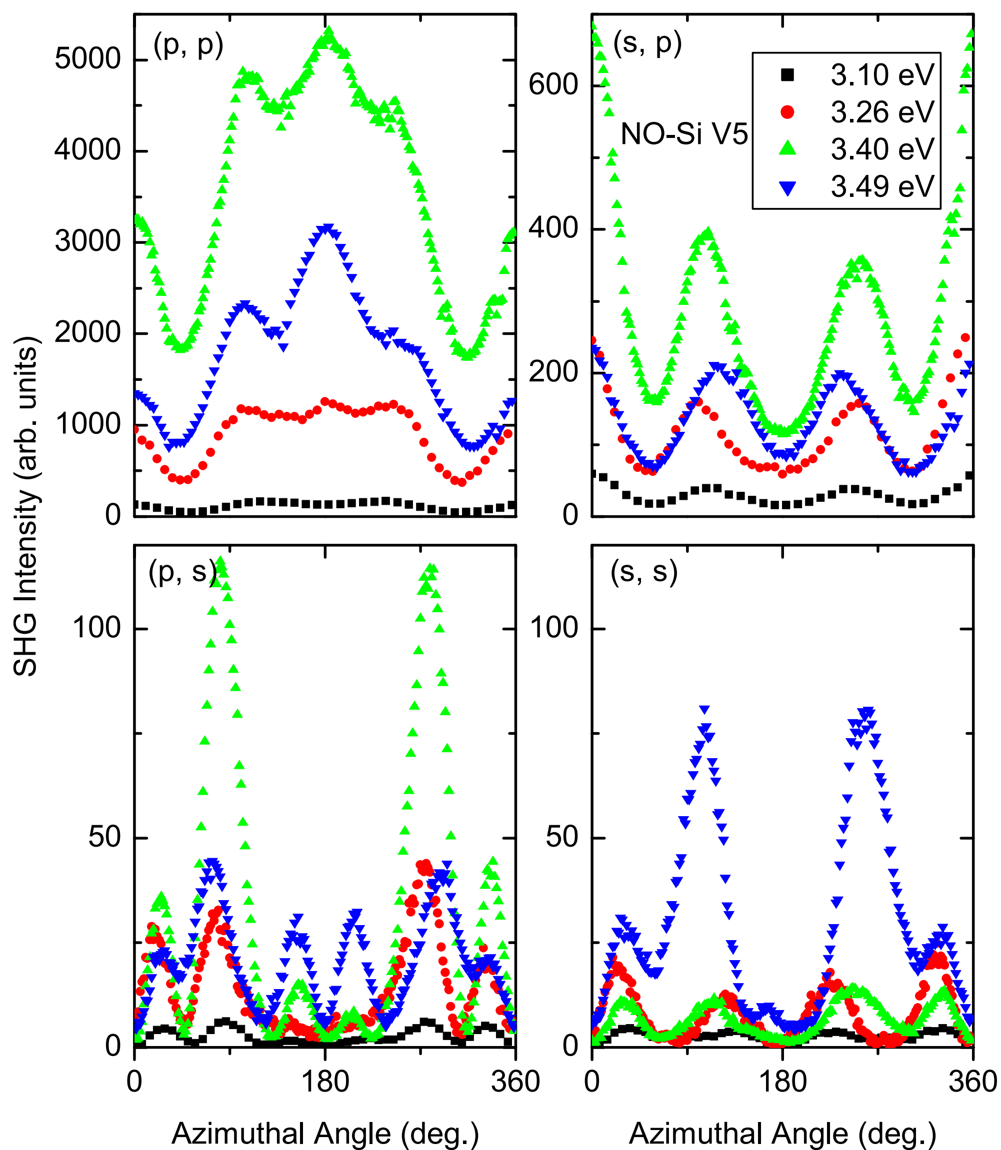

Fig. A.3. RA-SHG signals from a natively oxidized Si sample with vicinal angle of 5° (NO-Si V5) at several two-photon energies of 3.10 eV 3.26 eV, 3.40 eV, and 3. 49 eV for different polarizations: (*p, p*), (*s, p*), (*p, s*), and (*s, s*).

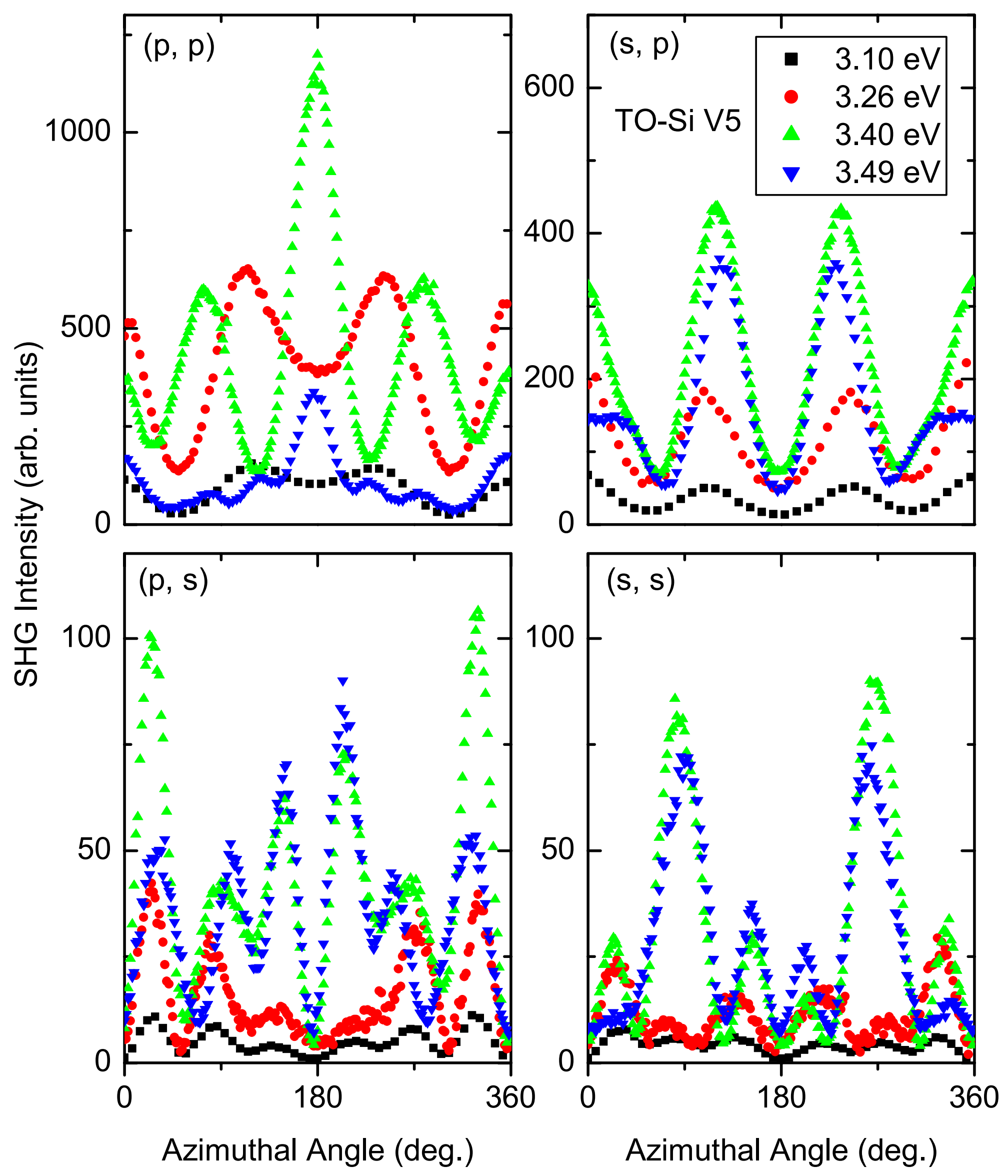

Fig. A.4. RA-SHG signal from a thermally oxidized Si sample with vicinal angle of 5° (TO-Si V5) at several two-photon energies of 3.10 eV 3.26 eV, 3.40 eV, and 3. 49 eV for different polarizations: (*p, p*), (*s, p*), (*p, s*), and (*s, s*).

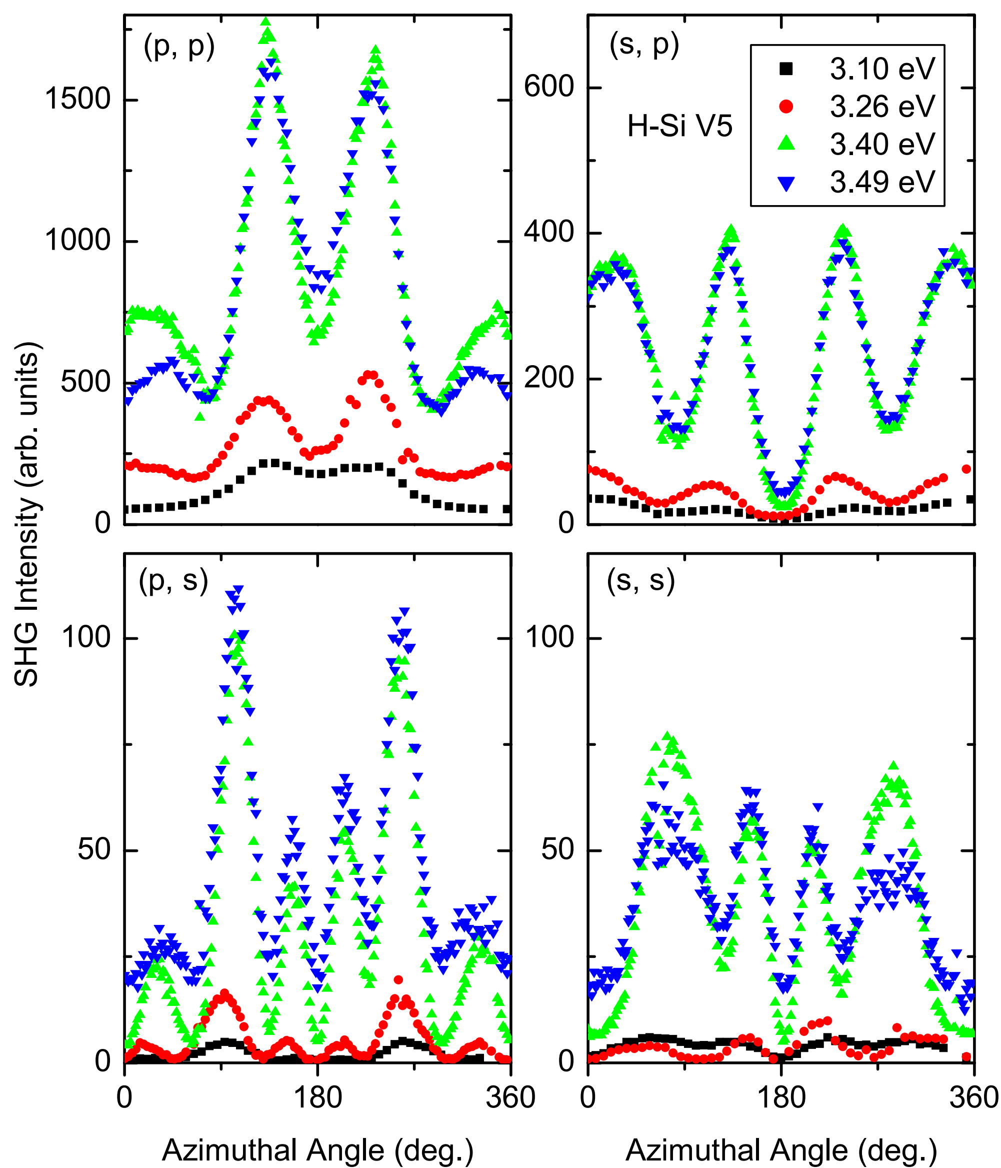

Fig. A.5. RA-SHG signal from a hydrogen terminated Si sample with vicinal angle of 5° (H-Si V5) at several two-photon energies of 3.10 eV 3.26 eV, 3.40 eV, and 3. 49 eV for different polarizations: (*p, p*), (*s, p*), (*p, s*), and (*s, s*).